Topological Toughening and Fracture of 2D Materials

by

Bo Ni

B.Sc., Engineering Mechanics, Xi'an Jiaotong University, 2011

M.Sc., Solid Mechanics, Xi'an Jiaotong University, 2013

A dissertation submitted in partial fulfillment of the

requirements for the Degree of Doctor of Philosophy

in the School of Engineering at Brown University

Providence, Rhode Island

May 2021

This dissertation by Bo Ni is accepted in its present form by the

School of Engineering as satisfying the

dissertation requirement for the degree of Doctor of Philosophy.

Date_____ _____

Prof. Huajian Gao, Advisor

Recommended to the Graduate Council

Date_____ _____

Prof. Kyung-Suk Kim, Reader

Date_____ _____

Prof. Jun Lou, Reader

Approved by the Graduate Council

Date_____ _____

Prof. Andrew G. Campbell

Dean of the Graduate School

Vita

Bo Ni was born in Huai'an, Jiangsu Province, China. He attended Xi'an Jiaotong University in 2007 and received the B.Sc. in Engineering Mechanics in 2011. Upon graduation, he was enrolled by Xi'an Jiaotong University with entrance examination waiver. He was rewarded the M.Sc. in Solid Mechanics in 2013. Subsequently, he entered the Solid Mechanics program at Brown University. His research mainly focused on theoretical modeling and numerical simulations of fracture behavior and toughening mechanisms in 2D materials and their integrated material systems.

Acknowledgments

First of all, I would like to express my sincere gratitude to my PhD advisor, Prof. Huajian Gao, for all his mentoring and guidance during the past years. His unparalleled insights and vision for science, persistent passion for research and high standard for work set an incredible example for me to learn from, both for the years past and the future to come. It is really a great honor for me to have been a member of Prof. Gao's group.

I would also like to thank my dissertation committee members, Prof. Kyung-Suk Kim from Brown University and Prof. Jun Lou from Rice University, who generously spend their time reading my thesis and offering valuable suggestions. I also want to thank the entire faculty of Mechanics of Solids at Brown University for providing the wonderful education and research environment. Thanks also to the administrative staffs at School of Engineering for providing support.

During my Ph.D. research, I had significant help and many suggestions from group members, collaborators and friends. I'm really grateful to Prof. Teng Zhang for his help and guidance at the beginning of my research. Some of my works were conducted in collaboration with some amazing experimentalists, and I'm sincerely grateful for Prof. Yingcao Yang, Prof. Sang Ho Oh for invaluable discussions and enjoyable collaborations. Special thanks to Prof. Xin Yi, Prof. Wenpeng Zhu, Prof. Haofei Zhou, Dr. Sheng Yin, Dr. Kai Guo, Dr. Guijin Zou, Dr. Yue Liu, Dr. Jiaoyan Li, Dr. S. Mohadeseh Taheri-Mousavi, Dr. Zhigong Song, Xing Liu, Zhi Li, Xuliang Qian, Dong Li and many other group members who shared their valuable experience and insightful discussions with me as well as my long-term friend Dr. Yue Shen and Mr. Tongzhou Zhang for their persistent support and company.

Finally, I want to thank my families with my whole heart, for all the love and support they offered me. Without their support and understanding, I would have never completed this thesis.

This work is dedicated to my beloved parents,

Jianjun Ni and Congfang Wang.

Contents

List of Tables

List of Figures

Chapter 1

Introduction

1.1 Brief review of fracture in 2D materials

The exceptional electronic (1-9), optical (9-11), thermal properties (12) and inherent flexibility (13-16) of newly emerging two-dimensional (2D) materials, including graphene (1-4, 10, 12), hexagonal boron nitride (*h*-BN) (5, 6, 9) and molybdenum disulfide (MoS_2) (7, 8, 11, 17), make them ideal candidates as building blocks for next generation technologies such as nanoelectronic devices (18-20) including field effect transistors (21-23) and nanomechanical resonators (24-26), corrosion-inhibiting coating (27), water desalination (28-30) and biological sensors (31). While each of these promising applications emphasizes a different aspect of 2D materials, the practical achievements of them all require the mechanical reliability of the structures. However, 2D materials are expected to have ultra-high strength with their nearly perfect atomic structures (32-36) but low fracture toughness due to their lack of efficient energy dissipation mechanisms. For example, an experimental study has shown the fracture toughness of graphene is only 16 J/m^2, close to that of an ideally brittle solid (37). Moreover, during large scale fabrication processes (e.g., chemical vapor deposition) (38-42) various forms of material defects (e.g. grain boundaries and their junctions) (43, 44) and geometrical flaws (holes, cracks, notches) will be introduced inevitably. When the corrosive species, like water vapor, are present in the working environment, the possible stress corrosion cracking process could further damage the fracture resistance of the materials (45, 46). Recently, strain engineering has

proven great potential in enhancing electron-phonon coupling (47) and tuning pseudomagnetic filed (48, 49) in 2D materials, thus becomes a promising reach direction demanding mechanical integrity under strain. The intrinsically brittle nature, inevitable flaws and possible corrosive or strained working conditions make fracture one of the most prominent concerns in large scale applications of graphene and other 2D materials (50-65).

As atomically thin layers, 2D materials have also demonstrated unique aspects in deformation behaviors and mechanical properties in different forms and dimensions. As a monolayer sheet, 2D materials are hard to stretch due to the strong in-plane covalent bonding (33) but remain flexible to bend given the extremely small thickness (66, 67). The large difference in the rigidity of in-plane (33) and out-of-plane (15, 16) deformations promotes 2D materials to go beyond the flat 2D configuration and explore low energy states in a three-dimensional (3D) space. For example, the presence of topological defects can trigger substantial out-of-plane deformation, especially in free standing cases, to minimize the strain energy (54, 68). The resulting 3D geometry will in turn alter mechanical and physical properties, including the elastic modulus, strength (51, 69), fracture toughness (70, 71), adhesion and friction (72), chemical reactivity (73), local density of states (74) and flexoelectricity (75, 76). This strong nonlinear coupling between topological defect, out-of-plane curvature and mechanical properties has been rarely observed in bulk materials. As layers stacking on top of one another, multilayered 2D materials represent a novel group of laminated materials with extremely high density of interfaces and strong anisotropy between intralayer and interlayer deformations (77, 78). For instance, the bending stiffness of van der Waals (vdW) heterostructures is determined by not only the intralayer properties but also interlayer shearing and slippage governed by atomic registry and dispersive vdW

interaction (79). The presence of massive interfaces and dispersive interlayer interaction is expected to affect fracture process and failure mode in multilayered 2D materials. As flexible building blocks or constituents, 2D materials can also hybrid with their zero-dimensional (0D) and one-dimensional (1D) counterparts to form new nanocomposites (80-83) or take 3D topology and geometry to form bulk assemblies. For example, graphene-fullerene hybrids (80, 81), graphene-carbon nanotube hybrids (83, 84) and 3D graphene assemblies (85-88) have been successfully fabricated in the laboratory. And the geometry and architecture of 2D material surfaces in these materials play crucial roles in generating overall properties and collective behaviors beyond their constituents. For instance, with different internal geometry, 3D assemblies made of graphene surfaces can be stiff and brittle microlattices (85, 86) or compliant and stretchable foams (87, 88). The freedom in constructing bulk materials using 2D material surfaces open doors to broad possibility for architected material design.

Combining these two observations, the following two questions become particularly interesting for fracture mechanics in 2D materials and relevant to engineering tough 2D materials and related systems. (1) How do these unique features, such as topological defects, out-of-plane curvature, 3D geometry and architecture as well as interlayer interactions, interact with the fracture process in 2D materials? (2) Can we take advantage of these novel interactions to toughen 2D materials and related systems? This thesis is motivated by these two questions. By integrating multiscale computational and theoretical models and collaborating closely with experimentalists, we aim at gaining some fundamental understanding about crack interactions with these novel features unique to 2D materials and based on that proposing effective toughening mechanisms as well as design guidance

for tough 2D material engineering.

1.2 Thesis organization

To address the questions raised above, in this thesis, we investigate some basic aspects of the crack interactions with topological defects, out-of-plane curvatures, 3D geometry and architecture as well as interlayer sliding in 2D materials and demonstrate toughening mechanisms and design guidance for various forms of 2D material systems, including monolayer sheets, hybrids with nanotubes, 3D nanolattices and multilayered 2D materials. This thesis consists of six chapters and is organized as follows.

Chapter 1 opens this thesis with a brief overview of the concern of fracture in 2D materials as well as the novel structures and interactions unique to 2D materials and set the theme of this thesis by raising two questions about the mechanics of fracture and toughening in 2D materials.

In Chapter 2, we investigate the interaction between topological defects, out-of-plane curvature and crack in monolayer graphene and propose a mechanism-guided topological design strategy to toughen graphene and similar 2D materials. Via concrete examples, we demonstrate various toughening mechanisms can be transplanted into brittle graphene by designing the distribution of topological defects and out-of-plane curvatures and toughen graphene collectively.

In Chapter 3, we collaborate with experimental experts to study the fracture process and toughening mechanisms in rebar graphene, a carbon nanotube-graphene hybrid. Combining experimental measurements with numerical simulations, we demonstrate how the carbon nanotubes integrated onto graphene interact with the propagating crack and

identify key toughening mechanisms and their dependence on the geometry and distribution of carbon nanotubes in rebar graphene.

In Chapter 4, we study the structure instability in graphene surfaces and propose a reversible energy dissipation mechanism via snap-through for 3D graphene nanolattices. By mimicking the shell geometry of flexible straw, we construct a graphene structure with snap-through instability and build 3D lattice with it. Through numerical simulations and theoretical analysis, we demonstrate this 3D graphene nanolattice can deform in a pseudoplastic way with stress-strain hysteresis and become tolerant to crack-like flaw via effective energy dissipation.

In Chapter 5, we focus on multilayered 2D materials and investigate the effect of neighboring layers and interlayer sliding on fracture process. By constructing a bilayer system with an initial crack in one layer, we demonstrate how interlayer interactions reduce the driving force at the crack tip and its dependence on system size, in-plane modulus and interlayer shearing stress through theoretical analysis and numerical simulations. Combining fracture-controlled crack propagation and strength-controlled crack penetration, we provide a phase diagram for the two competing failure modes to predict the crack evolution in multilayered 2D materials.

Chapter 6 concludes the entire thesis with major scientific findings, engineering implications as well as future perspectives.

Chapter 2

Topological Toughening of Graphene

Chapter Summary

With the ultra-high elastic modulus of 1 TPa and theoretical strength of 130 GPa, graphene has been claimed to be one of the strongest materials. However, from an engineering point of view, it is the fracture toughness that determines the actual strength of the material given that crack-like flaws such as cracks, holes, notches and corners are inevitable in the fabrication and operation of practical devices and systems. Recent experiments and simulations have demonstrated that graphene has very low fracture toughness, in fact close to that of ideally brittle solids. These findings have raised sharp questions and are calling for efforts to explore effective methods to toughen graphene.

Here, we present a topological toughening strategy to address this challenge. Built upon the out-of-plane effect of the topological defects in 2D materials, we decorate pristine graphene with networks of out-of-plane curvature by simulating the distribution of topological defects using phase field crystal (PFC) modelling. Through fracture tests with molecular dynamics (MD) simulations, it is demonstrated that the interaction between topological defects, out-of-plane curvature and crack can alter the brittle fracture process in graphene and various toughening mechanisms, including crack tip blunting, crack trapping, fracture mode transition, ligament bridging, crack deflection, void formation, interfacial failure, daughter crack initiation and coalescence, can be activated through

effective topological design. Based on this novel capability, vein-patterned graphene and nacre-like graphene are constructed by mimicking tough insect wings and nacres in nature and show enhanced fracture toughness and tolerance to crack-like flaws. The findings reported here present novel connections between simple topological patterns and effective toughening mechanisms in atomically thin materials and are expected to provide fundamental guidance for tough 2D material design and engineering.

2.1 Introduction

Because of the nature of strong covalent bonding and nearly perfect lattice, pristine graphene has been claimed as one of the strongest materials. Nanoindentation tests of free-stranding monolayer graphene have discovered an intrinsic strength as high as 130 GPa with a critical strain of 25% (33). These superior mechanical properties play important even critical roles in various applications of graphene, ranging from flexible electronics (20, 38), functional devices (24, 89, 90), DNA sequencing (91, 92), gas separation (93, 94) to water desalination (28, 30, 95). For instance, the outstanding stretchability of graphene makes strain engineering, i.e., tuning the properties of graphene via mechanical strain, highly promising and has led to a new research field of so-called "straintronics" (96, 97). However, from an engineering point of view, it is the fracture toughness, which describes the resistance of the material against crack propagation, that determines the actual strength of the material, given that defects and flaws are almost inevitable during the design, fabrication and operation of large scale samples and practical devices. Disappointingly, recent experiments as well as simulations (98-100) have demonstrated that graphene fractures brittlely with a fracture toughness as low as ~16 J/m^2 (98), close to that of ideally brittle solids. At the same time, during large scale fabrication processes (e.g., using

chemical vapor deposition) (101-103), various forms of material defects (e.g., vacancies, disclinations, dislocations, grain boundaries and junctions) and geometrical flaws (e.g., cracks, notches, corners and holes) will be introduced almost inevitably (43, 44, 104, 105), which can serve as initial flaws for brittle fracture. Moreover, when corrosive species, like water vapor, are present in the working environment, the possible stress corrosion process can further damage the fracture resistance of the material (106, 107). Thus, the combination of intrinsically brittle nature, inevitable flaws and possible harsh working environment makes fracture one of the most prominent concerns that limit the realization of the superior properties and functions of graphene in engineering applications and call for urgent efforts to explore effective methods to toughen graphene and other similar 2D materials (108, 109).

Built upon the unique effect of small scale defects, such as dislocations, grain boundaries (GBs) and twin boundaries, on deformation mechanisms and fracture behaviors, defect engineering has long be recognized as a versatile tool for enhancing mechanical properties for various types of materials in 3D, including metals(110-113), ceramics (113-115) and diamond (116). For example, nanoscale engineering of grain boundaries (GBs) and twin boundaries has been adopted to design superior metals with high strength, toughness and fatigue resistance (111, 117, 118). Fracture toughness of ceramics (e.g., Al_2O_3 and Si) shows a more than two-fold enhancement due to the creation of high density of tangled dislocations in the subsurface region (115, 119). Nano-twined cubic boron nitride (114) and diamond (116) exhibit higher hardness and toughness than their defect-free counterparts. These successes in bulk materials encourage the exploration of defect engineering in 2D materials and recent studies do have shown similar toughening effects of nanoscale defects in graphene (120-124). For example, via MD simulations and

continuous modelling, it has been demonstrated that the stress associated with individual defects, such as dislocations (a pentagon-heptagon pair) (120), Stone-Thrower-Wales defects (5-7-5-7 membered rings) (121-123) and 5-8-5 defects (124), can alter the crack tip field and shield the crack, similar to dislocation shielding effect studied in metal (125). In graphene samples containing regular or irregular GBs, through MD simulations, crack branching and atomic chain bridging are observed as the weak points within pentagon-heptagon defects break first near a crack tip during crack propagation (70), echoing the crack pattern due to a competition between intergranular and transgranular fracture in polycrystalline bulk materials. Combining these toughening mechanisms (e.g., stress shielding, crack branching and atomic chain bridging), a 50% enhancement in fracture toughness was reported for a polycrystalline graphene sample with well-stitched randomly distributed GBs in a comparison to pristine graphene (70). However, compared with the requirements of engineering applications, those enhancements are still far away from being satisfying and the demand of further toughening graphene remains strong.

Besides these similarities, recent studies have also identified important distinctions of defect engineering in 2D materials compared to that in bulk materials. Specifically, the atomic thin geometry and the sharp contrast in the rigidity of stretching and bending have made out-of-plane relaxation a prominent feature unique to 2D materials. Considered as a plate with thickness of 0.335 nm, graphene shows an ultrahigh in-plane Young's modulus of 1 TPa (33) while the experimentally measured bending rigidity is only about 1.2 eV (1.92×10^{-19} N m) (66). In other words, graphene as a 2D membrane is very stiff to stretch while highly flexible to bend. Consequently, it prefers to adopt a 3D configuration to release the strain energy induced by topological defects. For example, with continuum

modeling and MD simulations, Zhang et al (54) showed that global 3D configurations can be formed by introducing a single disclination into pristine graphene sheets, such as a cone shape for a pentagon and a saddle surface for a heptagon. Even an isolated dislocation can cause substantial out-of-plane deformation. This novel freedom of forming out-of-plane geometry via designing topological defect distribution is absent in bulk materials. And it has been widely recognized that the out-of-plane shape of graphene plays a crucial role in determining its mechanical and physical properties, including elastic modulus (126), strength (51, 126), fracture toughness (70, 71), adhesion and friction (72), chemical reactivity (73), local density of states (74) and flexoelectricity (75, 76). For instance, Zhang et al (71) investigated the properties of a sinusoidal graphene ruga which contains periodically distributed disclination quadrupoles and found from MD simulations that the mode I fracture toughness of the selected sinusoidal graphene is around 25.0 J/m^2, about twice that of the pristine graphene. These findings are suggesting that there exit unique and intriguing interactions between topological defects, out-of-plane geometry and material properties in 2D materials and encouraging further investigations on how to utilize the coupling between topological defects and membrane curvature to design a 2D material that conforms to an pre-designed 3D geometry for enhanced material properties, including fracture toughness, which has recently been coined as the concept of "topological design of graphene" (127).

At the same time, there are rapid developments in experimental capability of synthetizing and modifying detailed topological structures of 2D material systems. At large scales, for instance, GBs in polycrystalline graphene grown by chemical vapor deposition (CVD) could be controlled using pre-patterned growth seeds for graphene nucleation (128,

129). With appropriate growth conditions, graphene can grow on substrate of various geometry, including porous metal foams (130, 131), network of nanowires and microparticles (132), 3D printed scaffolds (133) and even zeolite crystal with nanoscale pores (85) and form topological defects to accommodate substrate curvatures naturally. At the molecular level, 2D carbon molecular sheets with heptagon and pentagon lattice have been chemically synthesized, whose equilibrium configurations are warped in 3D space (134-136). In controlled growth of hybrids of graphene and carbon nanotubes (CNTs) (84), topological defects are observed in the connection regions with varying curvature. At the atomic level, topological defects with designed types and location have been created with controlled irradiation or thermal excitation (137). Flat graphene could be rippled at nanoscale via dislocation addition (138). These experimental studies have paved a promising way to fabricate 2D material sheets with designed topological defect distribution and out-of-plane geometry and are calling for in-depth studies to fully explore the potential benefits of this topological design approach in graphene.

In this study, we employ the novel concept of topological design of 2D materials to toughen graphene. By taking advantage of the coupling between topological defects and out-of-plane geometry, we present tough graphene samples with bio-inspired topological designs and demonstrate that a variety of toughening mechanisms that are alien to pristine graphene can be activated and alter the brittle fracture in graphene collectively. The novel connections between simple topological patterns and effective toughening mechanisms discovered here are expected to provide inspiring guidance for next-generation tough 2D material design and engineering.

2.2 Results

2.2.1 Bio-inspired design of vein-patterned graphene

Instead of randomly exploring arbitrary topological defect distribution and out-of-plane geometry, we borrow inspirations from some tough 2D structures in nature, such as the tough wings of the desert locust *Schistocerca gregaria*. As part of its exoskeleton, the wings of the locust do not have any self-repairing mechanism yet are able to sustain millions of cycles of mechanical load and deformation during the insect's long-distance flying lifespan (Figure 2. 1A). Morphology studies(139, 140) have shown that the wing consists of numerous membrane cells divided by a network of longitudinal veins (LVs) and cross-sectional veins (CVs) with an annulated structure (Figure 2. 1B and C). Fracture tests (139) on the wing have identified that veins can play the role of barriers to crack propagation and enhance the wing's toughness by 50%. Specifically, the CV can blunt the crack tip and secondary crack nucleates ahead of and coalesces with the main crack (Figure 2. 1D) while the LV can deflect the crack path (Figure 2. 1E), thus transferring the catastrophic crack propagation in the membrane into a series of discrete events of crack stopping, nucleation and coalescing as indicated by the steps in the stress-strain and crack length-strain curves in Figure 2. 1F.

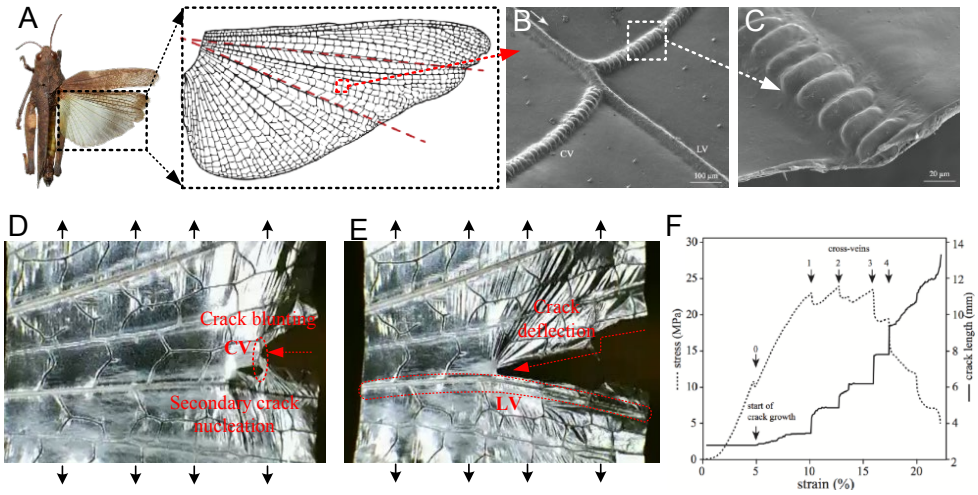

Figure 2. 1 Morphology of S. gregaria hind wings and fracture test of fresh wings (139, 140). (A) a membrane-vein structure of the insect wing. (B) Longitudinal veins (LV) and cross veins (CV) embedded in the membrane of the wing. (C) Compartment-like annulated structure of a cross-vein. (D and E) Propagating an initial edge crack in the fresh wing by mechanical load. As the crack hits the CVs, the crack tip becomes blunted (D) and secondary crack nucleates ahead of and then coalesces with the main crack (E). (F) Stress-strain curve and corresponding crack length recorded during a fracture test of the wing.

Inspired by the toughening role played by the vein networks in the insect wings, we constructed the graphene counterpart of the insect wing by mimicking the morphonology of the membrane and veins through topological design. As shown in Figure 2. 2A, a representative element (indicated by the red dash rectangle) of the insect wing includes the flat membrane as well as the annulated vein. To simplify the geometry, we replaced the membrane with a flat surface in *xOy* plane, the vein with a sinusoidal surface oscillating in the out-of-plane direction as,

$$z = A\sin\left(\frac{2\pi}{\lambda}y + \pi\right), \tag{2.1}$$

where A is the amplitude and λ is the wavelength. By connecting the flat phase and the wavy phase with a smooth transition, a 3D surface version of the representative element of

the insect wing can be constructed (Figure 2. 2B). To generate a graphene unit cell which adopts such a 3D shape, we simulated the crystal growth process on this designed 3D surface using a phase field crystal (PFC) model (Figure 2. 2C) (141) and translated the stationary distribution of the phase density, ϕ, into the atomic coordinates of carbon atoms in graphene (Figure 2. 2D) (142). For nanoscale graphene, we only introduced small out-of-plane oscillation by taking $A = 1.4\,nm$ and $\lambda = 4.6\,nm$. The thermal stability of the obtained graphene unit cell was validated by relaxing it under an NPT ensemble with Nose-Hoover thermostat (143) at 0 *Pa* and 300 *K* for 50 *ps* using MD. The geometry and potential energy distribution of the relaxed sample are shown in Figure 2. 2E. It should be noted that even through the relaxed graphene unit cell does not fully conform to the designed geometry, the wavy-flat pattern is stably maintained. Careful inspection shows that the topological defects, such as disclinations and dislocations, only concentrate at the connection between flat and wavy surfaces to accommodate the curvature transition, while flat and wavy surfaces are defect-free.

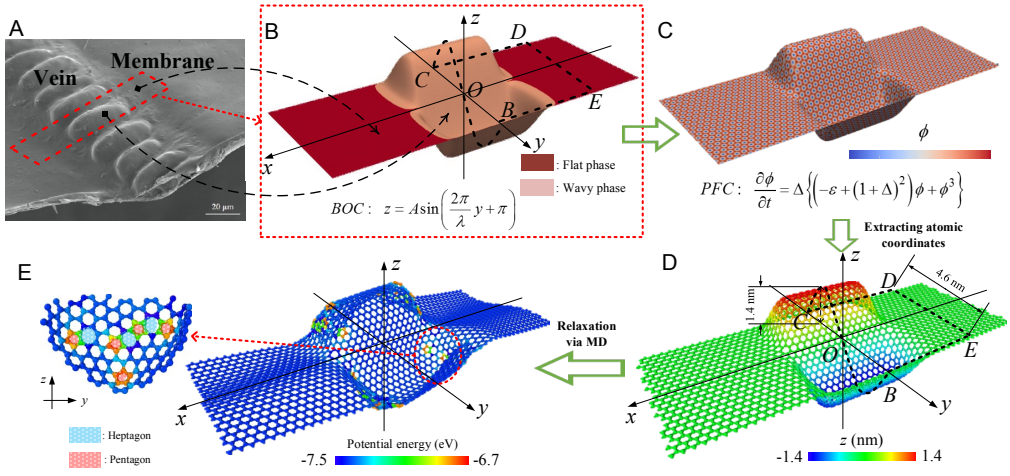

Figure 2. 2 Topological design of a representative element of the insect wing with graphene. (A) A representative element of flat membrane and annulated vein in the insect wing. (B) A simplified 3D

surface based on the morphology of the representative element of the insect wing. (C) Simulating the crystal growth process of graphene on the designed curve surface using a phase field crystal (PFC) model. (D) The atomic structure of the graphene sample adopting the designed geometry. (E) The geometry of the topologically designed graphene sample after MD relaxation and the topological defects distributed at the transition between flat and wavy regions.

2.2.2 Toughening effects of wavy phases in vein-patterned graphene

To explore the potential barrier effect of the vein-like wavy geometry on cracks in graphene, we first adopted an 1D parallel strip pattern to embed the wavy phase into a graphene sheet and conducted fracture tests with MD simulations. As shown in Figure 2. 3A, by replicating the constructed graphene unit cells, a vein-patterned graphene containing strips of flat and wavy phases alternating over a periodic width, a, is constructed, mimicking an insect wing with a set of parallel veins embedded. By the changing the width of the flat strip, the ratio of the flat phase, κ, varies within the interval, (0,1], where $\kappa = 1$ corresponds to the pristine graphene. MD simulations of uniaxial tension tests were performed to propagate an initial edge crack in a large sample of the vein-patterned graphene by applying a constant strain rate of 10^9/s to the simulation box along the y direction (Figure 2. 3B). During the test, a periodic boundary condition was applied along the loading direction and an NVT ensemble with Nose-Hoover thermostat (143) was adopted to maintain a constant temperature of 10 K.

The fracture tests of pristine graphene and vein-patterned graphene demonstrate that the wavy phase in the vein-patterned graphene can act as barriers to crack propagation and toughen graphene effectively. For a pristine graphene sample without any wavy phase (i.e., $\kappa = 1$), as the loading strain increases, high stress concentrates in the crack tip and the crack

starts to propagate in at a relatively low strain level (Figure 2. 3C1); As the crack propagates, the region ahead of the crack tip has already stored a high level of strain energy, which supplies abundant driving force to the crack tip (Figure 2. 3C2) and leads to a catastrophic failure with a dive in the stress-strain curve (see the blue dash curve in Figure 2. 3D). A fracture energy $G_0 = 13.8 J/m^2$ is obtained using the driving force analysis in fracture mechanics (144), which is in close agreement with the values reported in the previous studies (98).

The presence of the wavy phase in the vein-patterned graphene tends to alter this brittle fracture behavior. Taking the sample with 50% of flat phase (i.e., $\kappa = 0.5$) as an example, initially the edge crack tip sits in the flat phase. As the loading strain increases, high stress level is built up at the crack tip and crack starts to propagate at an early stage (Figure 2. 3E1), similar to the pristine graphene case. However, as the crack tip hits the wavy phase, it is surrounded by the relaxed wavy surfaces and the local supply of the driving force is lost, thus stopping the crack from propagating. As the applied strain further increases, the local stress in the flat phase (Figure 2. 3E2) and the overall stress (E1 to E2 in the red curve in Figure 2. 3D) keeps growing because the crack tip remains trapped and becomes blunted (Figure 2. 3E2). A careful inspection reveals that for the crack tip trapped in the wavy phase, the mode I fracture load from the remote is actually transformed into an out-of-plane tearing mode near the crack tip due to the geometry of the wavy phase (Figure 2. 3F). This transition of fracture mode also helps crack blunting and trapping. The critical moment occurs as the neighboring flat phase ahead of the crack reaches its strength and a daughter crack suddenly initiates from the weak spot of the topological defects (heptagon), leaving the remaining ligament of the wavy phase between the two cracks bridging the

crack surfaces (Figure 2. 3E3). As new daughter cracks initiate in each flat phase and coalesce with the main crack (Figure 2. 3E4), the overall stress level drops (see the red curve in Figure 2. 3D). Due to the bridging effect of the wavy phases, the dropping slop is also mitigated comparing to that of the pristine graphene case (see the triangles in Figure 2. 3D). In short, the wavy phase in the vein-patterned graphene can trap and blunt the crack, transform the local fracture mode, lead to daughter crack nucleation, ligament bridging and crack coalescence, thus changes the catastrophic fracture in pristine graphene. The measured fracture energy for the sample with $a = 12nm$, $\kappa = 0.5$ reaches 61.4 J/m^2, which much larger than that of the pristine graphene.

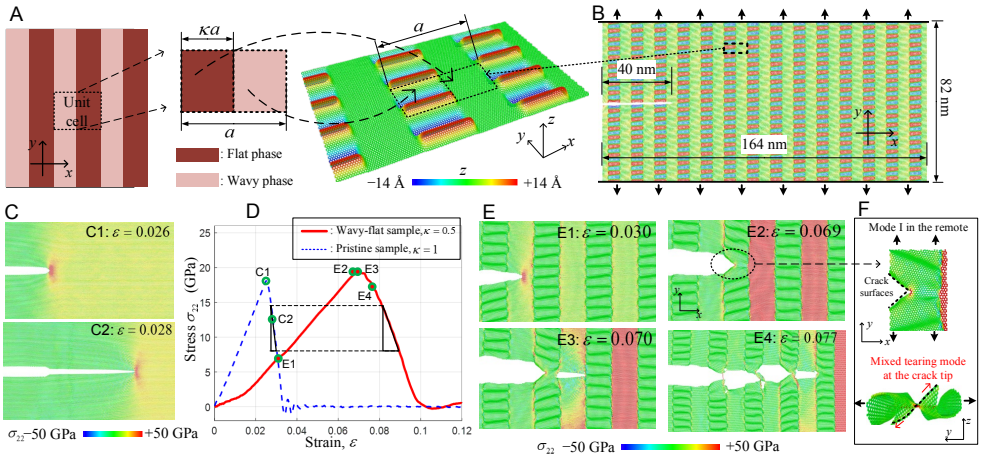

Figure 2. 3 Fracture tests of 1D vein-patterned graphene. (A) 1D parallel strip pattern of wavy phases embedded in graphene built with the topologically designed graphene unit cells. (B) Propagating an initial edge crack in a vein-patterned graphene sample by applying uniaxial tension. (C) Brittle fracture process in pristine graphene. The critical moment (C1) and the catastrophic propagation (C2). (D) Overall stress-strain curves of the fracture tests on pristine and vein-patterned graphene. (E) Fracture process in the 1D vein-patterned graphene sample with a flat phase ratio of 0.5. (F) Mode I fracture load from the remote is transformed into a mixed tearing mode at the crack tip as the crack is trapped in the out-of-plane wavy phase.

To investigate the effect of the flat phase ratio on the toughening mechanisms and fracture energy, we conducted similar fracture tests on samples with a fixed wavy-flat

periodic width, $a = 12\,nm$, and a flat phase ratio, κ, varying between 0 and 1 and summarized the results in Figure 2. 4. As shown in Figure 2. 4A, at the critical moment, crack trapping due to the wary phase was observed for all cases (except the pristine one). Correspondingly, as κ decreases, in Figure 2. 4A the critical strains (marked as the peaks in the stress-train curves) decreases and the unloading slopes tend to be flattened, indicating the less the flat phase is, the stronger the effects of crack trapping and ligament bridging are. At the same time, the loading slopes of stress-strain curves in Figure 2. 4B suggests the in-plane modulus decreases as κ decreases. These two effects make a tradeoff with toughness enhancement. As shown in Figure 2. 4C, a maximum value of fracture energy, $G = 83.2\ J/m^2$, is found at $\kappa = 0.8$, corresponding to a six-fold enhancement in the fracture energy.

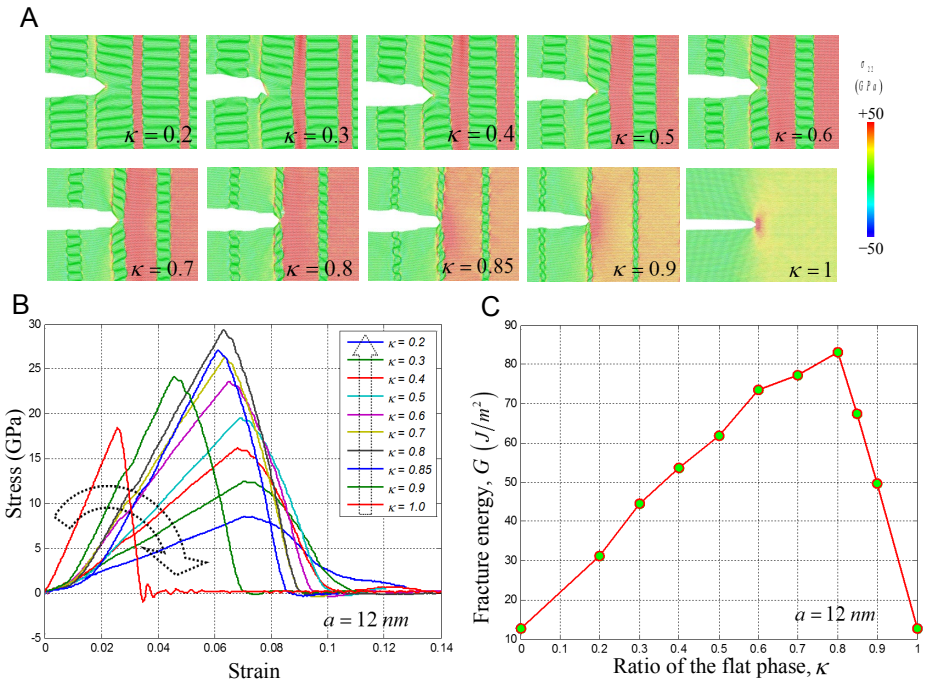

Figure 2. 4 The effect of the flat phase ratio on the toughening mechanisms and fracture energy in 1D vein-patterned graphene. (A) Crack trapping at the critical moment for samples with different flat phase ratio. (B) Stress-strain curves of fracture tests on samples with different flat phase ratio. (C) Measured

fracture energy for samples with different flat phase ratio.

The results of the 1D vein-patterned graphene have demonstrated that the interaction between crack and the vein-like wavy phases can alter the fracture behavior in graphene and toughening mechanisms such as crack trapping, crack blunting, fracture mode transition, daughter crack initiation, ligament bridging and crack coalescence, can be activated and optimized. However, the 1D parallel strip pattern show low symmetry within the 2D plane and cracks that are parallel to the wavy strip may not be contained effectively. To overcome this limitation, in the next section, we generalize this vein-patterned graphene by adopting 2D networks of wavy phases and demonstrate the effect of the 2D distribution on toughening graphene.

2.2.3 Effects of the 2D networks of wavy phases in vein-patterned graphene

Just like the veins in the insect wing forming a network to fulfill their biological and mechanical functions, in this section we take the distribution of the vein-like wavy phases as a new degree of freedom to design and construct vein-patterned graphene samples with various types of 2D networks of out-of-plane curvatures and demonstrate the toughening mechanisms associated with them.

To demonstrate the effect of a 2D network of wavy phases, we have constructed vein-patterned graphene samples with a hexagonal network of out-of-plane curvatures and conducted fracture tests on them using the topological design framework introduced in the previous section. As shown in Figure 2. 5A, sinusoidal wavy phases with an out-of-plane amplitude of 0.84 nm are embedded in flat graphene following a hexagonal network. The unit cell containing the wavy and flat phases has a dimension of $a = 9.54\ nm$ (measured

from the center to one corner) and the area ratio of the flat region is κ. After relaxation, the hexagonal distribution of wavy phases remains and the topological defects (which show relatively high potential energy) are found only at the interfaces between the flat and wavy phases (Figure 2. 5B). Fracture tests (similar to that in Figure 2. 3B) are conducted for samples with different κ and various toughening mechanisms are identified. Taking the sample of $\kappa = 0.49$ as an example, as the initial sharp edge crack propagates in the flat phase and hits the neighboring wavy phase, it is then trapped by the relaxed wavy surface and the crack tip becomes blunted as the overall load keeps increasing (Figure 2. 5C left). Different from the previous case of 1D distribution of wavy phases, with the hexagonal network, there exist wavy phases lying along the direction perpendicular to the overall loading. And across these wavy phases, the out-of-plane geometry leads to spots with high stress concentration as load is transferred nonuniformly (dash ellipses in Figure 2. 5C right). As the overall load reaches a critical level, multiple voids nucleate from the topological defects within these stress concentrated spots (Figure 2. 5D), which corresponds to the slight drop in the over-all stress-strain curve (Point D in Figure 2. 5H). The formation of nanovoids in the region ahead of the main crack is expected to help to dissipate stored deformation energy (145). As the load further increases, at the main crack tip, the wavy phase is further flattened and the stress in the neighboring flat region grows. Consequently, the voids on the interface between these wavy and flat phases coalesce and the interface fails, resulting in a daughter crack right ahead of the main crack and the vertical wavy phase bridging the two (Figure 2. 5E). As the load further increases, multiple daughter cracks form at interfaces between wavy and flat phases ahead of the main crack while the remaining materials bridges the crack surfaces (Figure 2. 5F). An effective bridging of the ligaments

between cracks can postpone the coalescence of the daughter cracks into the main crack and promote more interface failure. In return, the formation of such a diffusive damage zone ahead of the main crack helps to dissipate the stored deformation energy and drain the driving force from the main crack. Finally, the sample fails with a large damage zone rather than a clear and single crack path (Figure 2. 5G).

Comparing with the fracture process in the sample with 1D distribution of wavy phase, 2D networks of wavy phases not only inherit the similar toughening mechanisms but also introduce new features. Specifically, wavy phases in both 1D and 2D networks can trap, blunt the crack tip and transform the local fracture mode, then cause daughter crack nucleation, ligament bridging and crack coalescence. Different from 1D distribution, the interfaces between wavy and flat phases in the 2D networks can act as novel sources for diffusive damage, such as multiple void formation and interfacial failure, in a large region ahead of the initial crack and lead to a intertwined geometry of ligament bridging. This effect extends the region of energy dissipation phenomena from individual locations along the initial crack direction (in the 1D distribution case) to a spread-out processing area surrounding the crack path. The new toughening mechanisms, including void formation and interfacial failure, and the expanded damage processing area may lead to further enhancement of toughness and resistance to crack-like flaw. For example, a fracture energy of $G = 91.2 J/m^2$ is measured for the hexagonal sample of $\kappa = 0.49$, larger than those of the previous samples with 1D distribution of wavy phases.

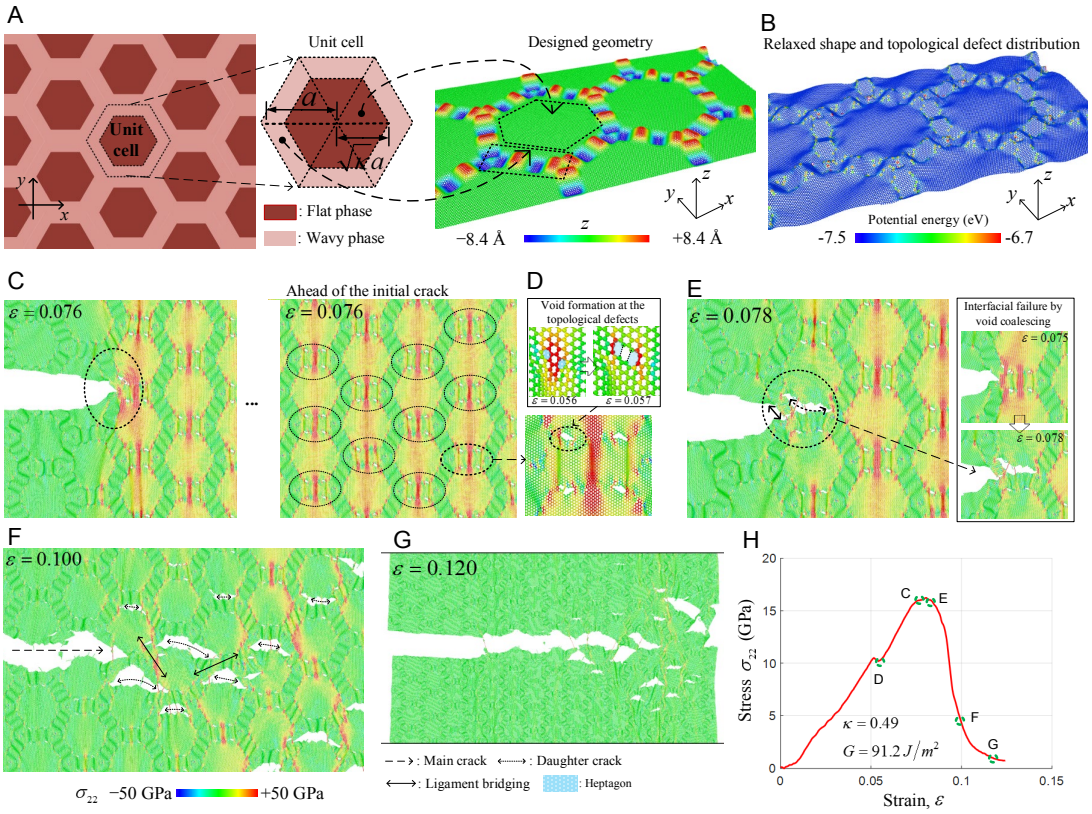

Figure 2. 5 Topological design of vein-pattern graphene with a hexagonal network of wavy phases and the activated toughening mechanisms. (A) Topological design of a hexagonal network of wavy phases in graphene. (B) The geometry of the relaxed sample and the distribution of topological defects indicated by the atomic potential energy. (C) Crack trapping by the wavy phase. (D) Void formation at the topological defects within the interfaces between wavy and flat phases that lie perpendicular to the loading direction. (E) First daughter crack nucleation due to void coalescence. (F) Multiple daughter crack nucleation and ligament bridging due to interfacial failures between wavy and flat phases in a large region ahead of the main crack. (G) The final crack path with diffusive damages within the sample. (H) The overall stress-strain curve of the fracture test.

The geometry of the 2D network of wavy phases also affects crack path via crack deflection. As observed in the hexagonal network cases, it is the interfaces with stress concentration as well as topological defects between wavy and flat phases where new cracks prefer to nucleate. When the bridging effect of the remaining ligaments is limited by either the geometry of the wavy phases or the loading condition, daughter cracks near

the main crack tend to coalesce with it. Thus, the initial crack can be deflected and attracted to a path consisting of these interfaces. For example, as shown in Figure 2. 6A and B, cracks along the armchair and zigzag directions of the hexagonal network are deflected to follow the wavy phases in the sample with a large flat ratio ($\kappa = 0.9$) given that the bridging effect is limited by the width of the wavy phases. The increased crack length also contributes to the enhancement of the effective toughness.

Similar toughening mechanisms are also observed in vein-patterned graphene samples with different distribution of wavy phases. For example, using topological design, we constructed a family of vein-patterned graphene samples with different 2D networks, such as triangular pattern, square pattern and diamond-celled pattern (Figure 2. 6C, E and G). Fractur tests reveals that similar toughening mechanisms, including crack trapping and blunting, fracture mode transition, daughter crack nucleation, ligament bridging, crack coalescence, void formation and interfacial failure and crack deflection, remain active in these different samples while the quantitative contributions may vary. For instance, cracks can be defected towards distinguishing paths following the specific distribution of the wavy phases (Figure 2. 6D, F and H) in different samples. The results on samples of various distributions suggest the toughening effects of the 2D network of wavy phases remain robust while the distribution of the 2D network is also an important degree of freedom in designing tough graphene samples.

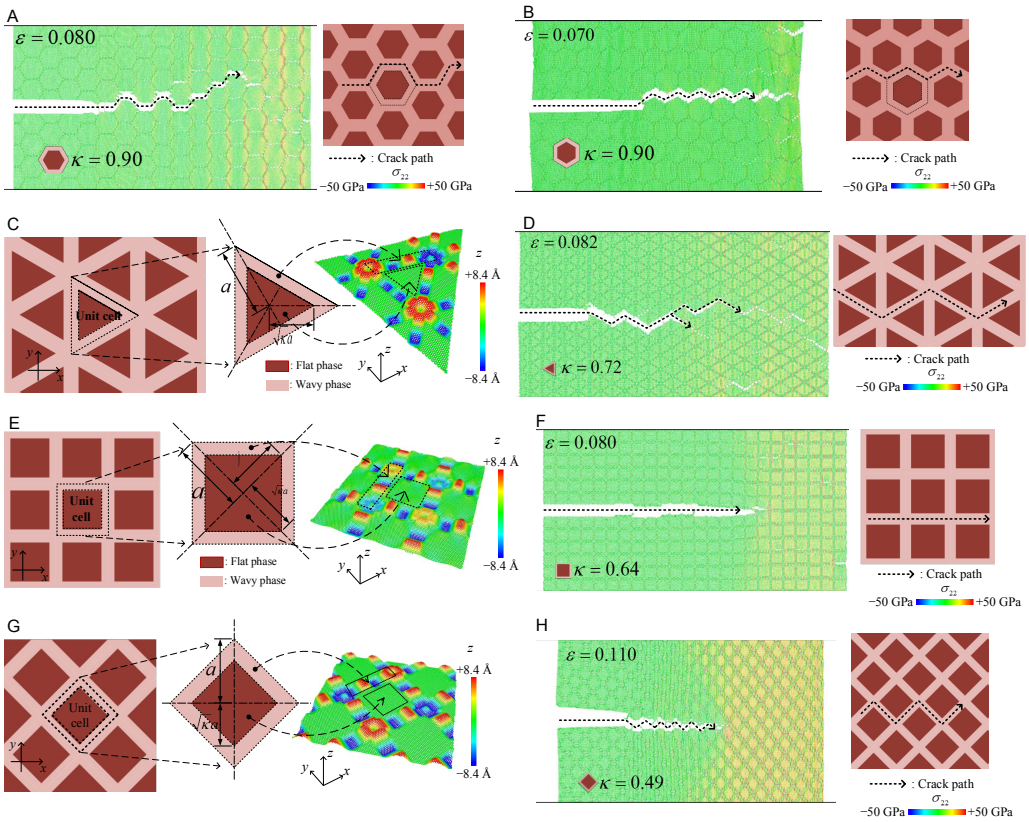

Figure 2. 6 Crack deflection in vein-patterned graphene samples with different of 2D networks. (A and B). Crack along armchair and zigzag direction of the hexagonal network are deflected to paths following the wavy phases in a sample of a large flat phase ratio. (C, E and G) Topological designed unit cells of vein-patterned graphene samples with a triangular (C), square (E) or diamond-celled (G) network of wavy phases. (D, F and H). Cracks in vein-patterned graphene samples can be deflected to different paths following their own distribution of wavy phases.

By comparing the fracture processes in pristine graphene and various vein-patterned graphene samples above, it becomes clear that the out-of-plane geometry of the individual wavy phases as well as the distribution of the wavy network play key roles in altering the fracture behavior and activate series of toughening mechanisms. By forming the out-of-plane curvature, the 3D shape of the wavy phases changes the local stress distribution and deformation response, forming sharp contrasts to those in a pristine/flat region. Thus, the wavy phases can behave as crack barrier when confronting an approaching crack and

energy dissipation sources when subjected to intensive loading. While the individual wavy phases alter the deformation and damage process locally, the distribution of the wavy phases organized these processes collectively by controlling potential sites for crack trapping and damage nucleation. Correspondingly, the distribution of daughter cracks and bridging ligaments varies with the network of wavy phases, resulting in different final crack patterns. A rational design of these two factors are essential to implement various toughening mechanisms and control the fracture behavior in graphene via topology design. As a demonstration, in the next section, we apply a mechanism-guided design strategy to construct a nacre-like graphene sample by controlling the out-of-plane geometry and 2D distribution of the wavy phases and mimic the tough fracture behaviors observed in nacre and nacre-mimicking materials.

2.2.4 Mechanism-guided topological design of nacre-like graphene.

Build upon the results of the vein-patterned graphene above, it is the recognized that the out-of-plane geometry and the distribution of the wavy phases influence toughening mechanisms strongly in topologically design graphene. This relationship in reverse provides a mechanism-guided strategy for topological design, i.e., constructing the effective out-of-plane curvatures and their distribution to achieve some targeted/given toughening mechanisms in graphene. In this section, we demonstrate this strategy via a rational design of nacre-like graphene.

As another tough material made of brittle components in nature, nacre (the pearly inner layer of many mollusk shells) (Figure 2. 7A) has been be studied intensively for its effective toughening mechanisms and provide biological inspirations to numerous tough

composite designs (146-148). The elementary structure of nacre consists of plate-like mineral crystals and soft protein matrix in a multilayered 'brick-and-mortar' architecture (Figure 2. 7B). Under uniaxial tension, the primary load is transferred through a tension-shear chain with the stiff mineral platelets as bricks under tension and the soft protein matrix as mortar in shear (Figure 2. 7C) (149). When a crack is introduced, there exist a number of toughening mechanisms around the crack tip identified by experimental and theoretical studies (Figure 2. 7C and E), including crack blunting induced by the soft organic matrix, nucleation and evolution of microvoids and microcracks around the crack tip to shield the remote load, platelet bridging between crack surfaces, organic ligament bridging during the shearing and relative sliding between neighboring platelets as well as crack deflection following the weak organic layers (147).

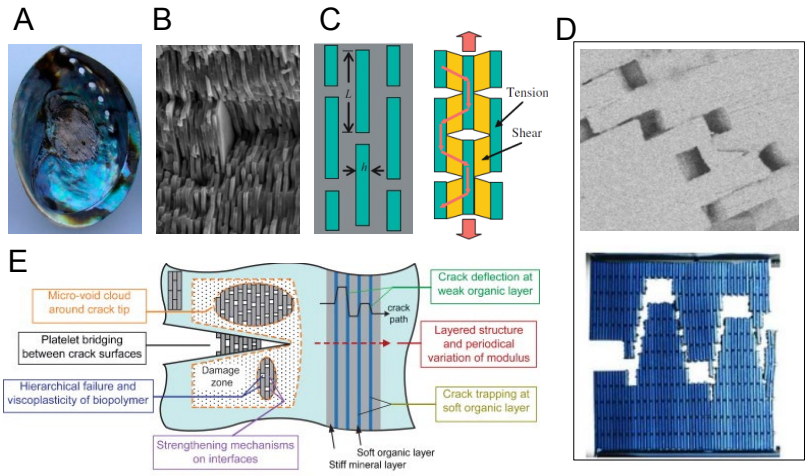

Figure 2. 7 Representative structure and toughening mechanisms in nacre and nacre-mimicking materials. (A) Nacre inside an abalone shell. (B) Microstructure of nacre. (C) The staggered pattern of hard plates in a soft matrix and a tension-shear chain model of the load transferring path (149). (D) Fracture paths in nacre and nacre mimicking materials (148, 150). (E) A schematic of typical toughening mechanisms in nacre (147).

Now, we set these toughening mechanisms as the goal to guide a specific topological design of nacre-like graphene. Based on the results on vein-patterned graphene, here we

use the wavy phases with out-of-plane curvature as the soft matrix while taking the flat phases of pristine graphene as the stiff platelets. The flat phases are organized in a staggered pattern connected by a 2D network of wavy phases (Figure 2. 8A). Different from the cases of vein-patterned graphene, two kinds of wavy phases are adopted to promote the tension-shear chain under a vertical loading. Specifically, as shown in Figure 2. 8B, a narrow single-sine surface is designed for the horizontal wavy phases lying perpendicular to the load while a double-sine profile with a half-period phase shift is taken for the vertical wavy phases parallel to the load. The atomic structure obtained through topological design shows that more topological defects are introduced in the double-sine wavy phases comparing with those in the single-sine ones (Figure 2. 8C), which are expected to promote the failure of the vertical wavy phases through shearing. Fracture test of propagating an initial edge crack is conducted in this graphene sample and a typical example is shown in Figure 2. 8D-G. As the initial crack hits the first vertical double-sine wavy phase, high stress is concentrated along the middle line of this wavy phase and one void forms at the saddle point with topological defect. Even through this void merges with the main crack quickly and the first sinusoidal surface fails, the main crack tip is still be trapped and blunted by the second sinusoidal surface in this wavy phase (Figure 2. 8D). As the crack tip is trapped, more voids nucleate from the stress concentrated topological defects in the horizontal wavy phases forming a damage zone ahead of the main crack while most of the vertical wavy phase remain intact (Figure 2. 8E). As the load increase, the horizontal wavy phases near the main crack fail along its interfaces connecting to the flat phases by void coalescence (Figure 2. 8G). The failure of the horizontal wavy phases transforms the load path into a tension-shear chain. As shown in Figure 2. 8H, the vertical wavy phase is sheared by the

flat phases it connects and the tension-shear chain formed by the flat phase and the vertical wavy phases bridges the crack surfaces. It should be noted that even through the multiple voids form inside, the vertical wavy phases can still tolerate the damage well without failure due to the trapping effect of the out-of-plane geometry. The out-of-plane geometry and the contained voids in turn help the vertical wavy phases to accommodate large relative sliding displacement (Figure 2. 8I left). Finally, a crack path deflected by the distribution of the wavy phases forms in the sample with diffusive damages around it (Figure 2. 8I right), similar to those observed in nacre and nacre-mimicking materials (Figure 2. 7C).

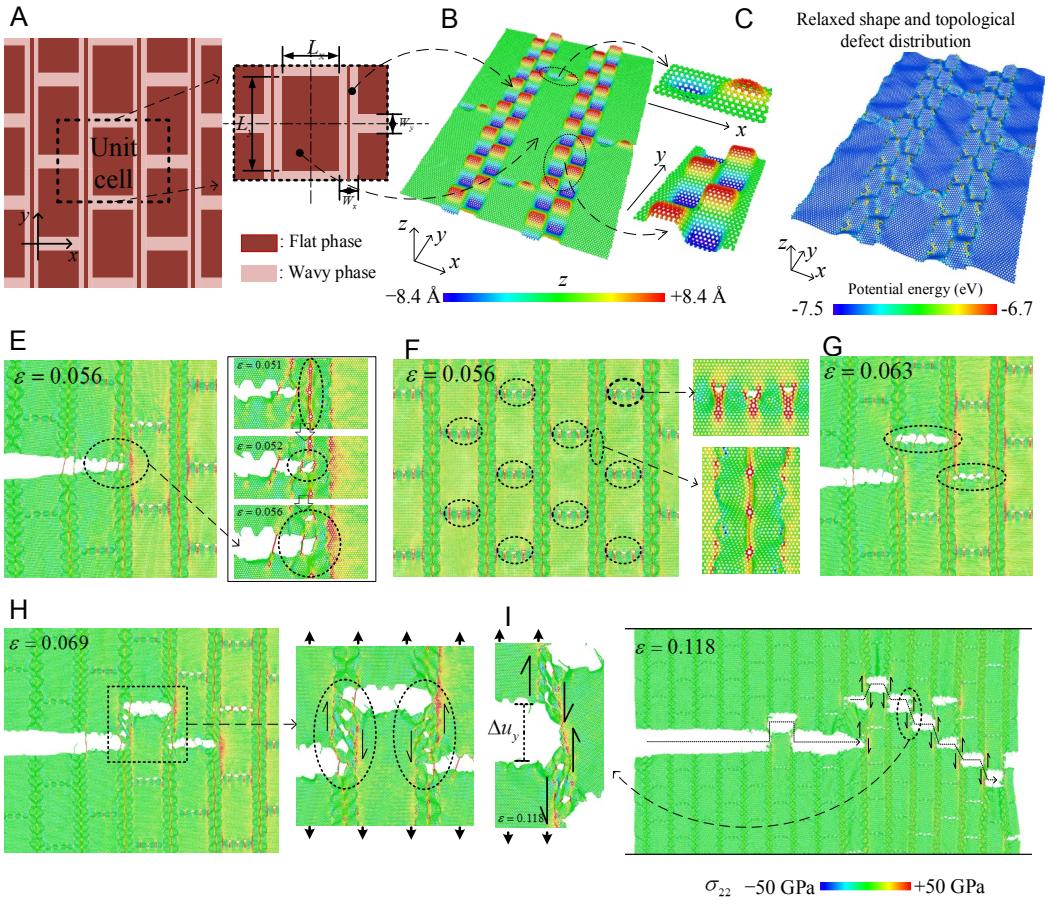

Figure 2. 8 Topological design of nacre-like graphene and fracture tests. (A) A staggered distribution of the wavy and flat phases following the typical pattern in nacre. (B) Atomic structure of nacre-like graphene with two different wavy phases designed to fail under tension and sustain large shear respectively. (C) Relaxed geometry and topological defect distribution in the designed nacre-like

graphene. (E-I) Fracture process and toughening mechanisms in nacre-like graphene. (E) Crack trapping and blunting at the vertical wavy phase. (F) Ahead of the crack, multiple voids form at the horizonal wavy phases from the spot with topological defects and stress concentration while the vertical wavy phases remain intact under tension. (G) The horizontal wavy phases fail as the voids merge. (H) After the failure of horizontal wavy phase, tension-shear chains are developed as the vertical wavy phases are under shear and the flat phase is under tension. Consequently, the vertical wavy phase and the flat phase together bridge the crack surfaces. (I) The vertical wavy phase sustains large relative displacement between the two ends. The final crack path is deflected by the distribution of the wavy phases.

Through the design and fracture tests of the nacre-like graphene, it is demonstrated that the deformation and toughen mechanisms provide valuable guidance for effective topological design. For example, the tension-shear chain model abstracted from nacre has inspired the design of the geometry and distribution of the out-of-plane wavy phases. Specifically, to facilitating the formation of the shear-tension chains in the staggered pattern, it is expected the horizonal wavy phase should fails at tension easily while the vertical wavy phases need to be tolerant to shearing and large sliding displacement. To fulfill these different functions, in nacre-like graphene, a single-sine surface is used for horizontal wavy phases to create stress concentration and weak spot of topological defects which trigger the failure under tension. When shearing is considered, a double-sine surfaces is adopted for more tolerance of relative sliding displacement as multiple voids formation at the saddle points and strong ligament bridging in between promote a stable flattening of the curved surface to accommodate a large elongation between the two pulling ends. Built upon this tension-shear chain, the major toughening mechanisms known to nacre, including crack blunting by the matrix/network, nucleation and evolution of microvoids and microcracks, platelet bridging between crack surfaces, ligament bridging during the shearing between neighboring platelets and crack deflection following the matrix/network, are reproduced in graphene effectively. The success of nacre-like graphene design suggests

that mechanism-guided topological design strategy provides an efficient way to harness the strong coupling between out-of-plane curvatures and deformation/fracture behaviors in the atomically thin sheet to implement toughening mechanisms that are alien to graphene.

2.3 Discussions and conclusions

The results of vein-patterned graphene and nacre-like graphene in the previous sections have demonstrated that a family of toughening mechanism can be imported into brittle graphene via a mechanism-guided topological design. Some of the fracture behaviors and toughening design enabled in topologically designed graphene indicate interesting similarities to those observed in other material systems while the uniqueness of the topological toughening of graphene still stands out. As a comparison, some unique aspects of this mechanism-guided topological toughening of graphene are discussed in the following.

1. The out-of-plane curvature plays the key role in activating novel effective deformation modes in the wavy phase of graphene. At the first glance, the introduce of wavy phases into flat graphene via topological design resembles a convergent tough design from nature and engineering, in which soft and hard components/phases are arranged alternatively to postpone crack propagation (149), such as the nacre made of soft organic matrix and hard mineral platelets (146) and tough hydrogels with stiff elastic dissipators embedded (151). However, the topologically designed graphene distinguishes itself by achieving the desired heterogeneous elastic properties through out-of-plane curvature. With nontrivial out-of-plane curvature, the deformation in the wavy phases under remote load is a mixture of bending and stretching and the effective in-plane elastic properties can

be tuned by designing the initial curvature. Moreover, the extra length released during the flattening process of the way phases makes it be much more tolerant to large deformation thus sustain a long-lasting bridging. Also, when a trapped crack tip tries to propagate in the wavy phase, the out-of-plane geometry surrounding the crack transfers the remote mode I fracture to a mixed mode subjected to tearing locally (Figure 2. 3F), which is a fundamentally different picture from that in bulk composites (152). At last, it is mainly a geometrical effect and no second material is introduced. The maintenance of the chemical purity in topologically designed graphene may be particularly beneficial to applications relying on the unique physical properties of graphene.

2. Topological defects are the fundamental building blocks for topological toughening of graphene. In continuum scale, it has also been demonstrated that the curvature can affect the fracture behavior in elastic brittle thin shell structures. For example, by draping elastic sheets to a curved substrate, experiments have discovered that the crack path can be deflected and guided by the curvature of the substrate (153). Using a phase field fracture model, numerical simulations has demonstrated crack in a thin shell can be attracted to and trapped by an out-of-plane dimple. Similar crack deflection and crack trapping are also observed in the topologically designed graphene. However, topological defects add new features to these curvature-induced toughening effects. Specifically, as a crystalline material in 2D, the nontrivial gaussian curvature in free-standing graphene can only be sustained by the distribution of the topological defects (54). At the same time, the topological defects also introduce residual stress and weak spots in graphene, which can facilitate more toughening mechanisms. For example, the voids in the interfaces between wavy and flat phases surrounding the main crack nucleate precisely from the topological

defects associated with residual stress and help to dissipate the strain energy. These coupled effects of topological defects make topological toughening of graphene more than the pure curvature effect on fracture in an elastic brittle thin shell.

In summary, in this chapter, we have demonstrated a mechanism-guided topological design strategy for graphene toughening. Based on the strong coupling between out-of-plane geometry and deformation behaviors in graphene, we bring networks of out-of-plane curvatures into graphene via controlling the distribution of topological defects and demonstrate various toughening mechanisms known to other tough material systems, such as insect wings and nacre, can be transplanted into graphene consequently. The forward relation from topological design to toughening mechanisms is studies and categorized by comparing vein-patterned graphene with various types of networks of wavy phases. And the possibility of inverse design of wavy phases to reproduce targeted deformation and fracture behaviors is demonstrated via a nacre-like graphene example. These findings advance the fundamental understanding about the connections between simple topological patterns and effective toughening mechanisms in atomically thin materials and are expected to provide rational guidance for tough 2D material design and engineering.

Chapter 3

CNT-Graphene hybrids: Toughening Graphene by Integrating Carbon Nanotubes

Chapter Summary

The low resistance to fracture has been a grave issue that limits the accessibility of the superior properties of graphene in practical applications. Besides toughening graphene via topological design, in this chapter we study an extrinsic toughening strategy for graphene by integrating carbon nanotubes (CNTs). The introduction of CNTs into bulk materials has proven to be a widely accepted method for toughening and strengthening materials. However, such toughening effect of CNTs on 2D materials remains largely unknown. Here, we focus on a unique material, rebar graphene, which consists of CNTs embedded in graphene and characterize its fracture behavior and toughening mechanisms through experiments and atomic simulations. By implementing a "dry" transfer technique, the freely suspended rebar graphene was systematically tested under uniaxial tension mode inside a scanning electron microscope (SEM). Combining experiments and molecular dynamics (MD) simulations, it is confirmed that the embedded CNTs divert and bridge the propagating crack and provide a toughening mechanism for the material. Our work identifies a promising extrinsic toughening strategy for 2D materials and provides mechanistic insights into the fracture process of similar graphene-CNT hybrid materials.

3.1 Introduction

Following the discovery of graphene by Geim and co-workers, a lot of effort has been dedicated to better understanding of the properties of graphene and its analogues (12, 52, 58, 98, 154-159). Graphene has attracted huge attention due to its extraordinary properties, such as high electrical conductivity (89, 158), high intrinsic strength and Young's modulus (33, 160), and high thermal conductivity (12, 161). In perfect graphene, extremely high modulus and strength can be achieved under uniform stretching and breaking of the strong C-C bond (52, 56, 156, 157, 160, 162-164). However, like many other materials, defects are inevitable which weaken graphene considerably. Based on the Griffith theory, the strength of materials depends on the size of crack/flaw in materials, rather than the intrinsic strength. Fracture toughness, which characterizes a material's ability to resist fracture, is quite limited for graphene, as confirmed recently by both experiments and theoretical calculations. The previous study demonstrates that the fracture toughness of graphene is only 4.0 $MPa \cdot m^{1/2}$ (98), which suggests that graphene is a typical brittle material. The magnitude of fracture toughness can not only determine the mechanical performance of materials, but also strongly affect the reliability and stability of flexible devices built with those materials. Considering that graphene has a great potential in building flexible devices, in case of mechanical failure, graphene-like materials with higher fracture toughness is in need. It is thus very important to develop toughening strategies for this exciting material.

Two general toughening strategies have been extensively explored in the past for bulk materials, namely, intrinsic toughening which exploits the microstructural features such as grain or phase structures to increase material toughness (58, 165); or extrinsic toughening where additional material components are added to help retard the crack advancement and improve fracture resistance(166, 167). A representative example of extrinsic toughening is

graphene reinforced nanocomposites. Due to its exceptional mechanical properties, high aspect ratio and low density, graphene is an ideal candidate for developing the next generation of polymer-matrix, metal-matrix, and ceramic-matrix composites. To date, there has been a significant amount of research work with focus on graphene reinforced composites. The related composites include: randomly dispersed graphene into matrix to reinforce composites (168, 169); functionalized graphene to reinforce composites (170, 171); laminated graphene or graphene oxide to reinforce composites (172); three-dimensional (3D) graphene foams to reinforce composites (130); hybrid graphene and other nanostructures to reinforce composites (173). Since it is still quite challenging to precisely control the microstructural features such as grain structures in graphene and there exists only limited evidence of sufficiently strong interactions between grain boundaries and crack tips in graphene, extrinsic toughening strategy seems to be a more plausible choice to toughen graphene(70, 163).

Because of the weak van der Waals interaction between 2D layers giving rise to rather inert surfaces that are free of dangling bonds, ideas have long been sought to engineer graphene properties through integration with other 2D materials. One such example is the so-called “van der Waals solid” (77) where graphene has been layered with various 2D materials to create vertical heterostructures exhibiting unique properties for electronic and optoelectronic applications (77, 159, 174). However, the inertness of the 2D material surface makes it more difficult for effective load transfer between layers that is oftentimes necessary for desired enhancement of mechanical properties as sought after in this study. Alternative strategies are clearly needed to fulfill the goal of toughening graphene. Yan et. al. has pioneered the synthesis of a new graphene hybrid material that combines a one-

dimensional (1D) material, carbon nanotubes, and a 2D material, graphene, into an integrated material (155, 175). This concept of the so called "rebar graphene" nicely relates the macroscopic idea of using embedded reinforcing steel bars to toughen and strengthen concrete to a 2D material in nanoscale. Many studies have been performed on the integration of CNTs into bulk materials, such as metals, polymers, and ceramics, to make nanocomposites with enhanced mechanical properties (84, 176). However, research on the mechanical interaction of CNTs with layered 2D materials is sparse (177).

In this chapter, we systematically investigated fracture behaviors of the freely suspended rebar graphene under uniaxial tension mode and identify the toughening mechanisms induced by CNTs. Combining SEM and atomic simulations, it is confirmed that the embedded CNTs can divert and bridge the propagating crack and provide a toughening mechanism for 2D materials.

3.2 Results

3.2.1 Experimental results

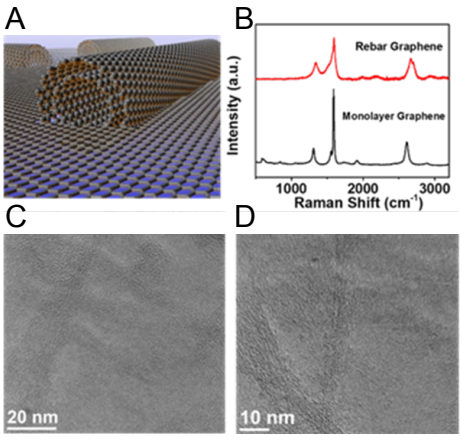

Figure 3. 1 Rebar graphene characterizations. (A) Schematic illustration of rebar graphene. (B) Raman spectra and (C-D) High resolution TEM images of rebar graphene.

Our collaborators, Prof. Jun Lou and his group at Rice University conducted the experimental study of rebar graphene and the results are summarized in the following. Figure 3. 1A provides a schematic illustration of rebar graphene and illustrates how CNTs are embedded into monolayer polycrystalline graphene. Rebar graphene is characterized using Raman spectroscopy as shown in Figure 3. 1B. A 514 nm excitation was used on rebar graphene and graphene, both on Cu foils in 10 different areas of a 1 cm^2 sample size. The Raman spectra of graphene exhibits two key features: a G peak at ~1580 cm^{-1} and a G' or 2D peak at ~2700 cm^{-1}. The D peak at ~ 1350 cm^{-1} correlates with the presence of some sp^3 carbon atoms, or defects. The rebar graphene spectrum has a shoulder on the 2D peak at ~2698 cm^{-1}, similar to monolayer graphene on copper. This shoulder location suggests a dominance of monolayer graphene in the rebar graphene sheets. Further characterization is seen in transmission electron microscopy (TEM) where the CNTs are shown in Figure 3. 1C and Figure 3. 1D. The images illustrate the interconnected CNT networks on graphene sheets. TEM images also reveal that some regions of the rebar graphene sample might have two-layer graphene islands, however the Raman spectra suggest a strong dominance of monolayer graphene. And based on the growth method and previous study, it is believed that CNTs are packed on the top of graphene layer, instead of forming a sandwiched 3D network on both sides of graphene (155).

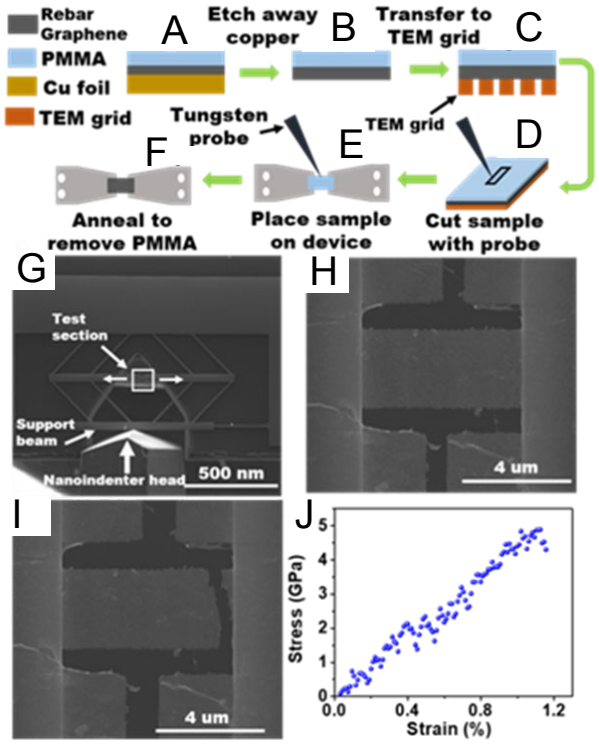

Figure 3. 2 Sample preparation and testing results. (A-D) After spin coating PMMA on rebar graphene sample, the copper substrate is etched away and a tungsten probe is used to cut out the sample area under optical microscope. (E) The sample area is placed in test section of the micromechanical device (F) The devices are annealed in a CVD furnace with N2/H2 mixture to remove PMMA. (G) SEM image of the testing device geometry. (H) SEM image of film in test area of device before fracture. (I) SEM image of film in test area after fracture to show the zig-zag fracture surface. (J) Stress-strain curve of the sample depicted in previous two images.

One of the biggest challenges in quantitatively characterizing mechanical properties of 2D materials is proper sample preparations. Transferring 2D materials requires spin coating a polymer, such as PMMA, to provide support during handling. Typically, these polymers can be removed using acetone; however, the suspended working layer of the mechanical device used for the tensile test of nanomaterials requires a dry transfer technique that avoids the use of any liquid, as shown in Figure 3. 2A-D (154). The process starts with spin coating a PMMA layer about 200-300 nm thick on the as-grown rebar graphene on copper substrate. The substrate is etched away and a floating layer of rebar

graphene and PMMA is left and fished out with a silicon substrate. After extensive washing, the film is transferred onto a TEM grid. The TEM grid is used to mitigate contact between the film and the substrate and add ease to the process of removing the film from the substrate. Under an optical microscope, a fine tungsten probe is used to cut away the area of the material that will be tested. The same probe is used to gently place the rebar graphene/PMMA on the test section of the micromechanical testing device. Once contact between the film and device is made, heat treatment is used to ensure proper adhesion. The entire device with the attached film is placed in a tube furnace and annealed under flow of hydrogen and nitrogen to remove the PMMA coating and leave the rebar graphene in the test section. The suspended rebar graphene is cut into a rectangular geometry using a focused ion beam (FIB). Careful attention is paid to use a beam current of less than 40 pA to protect the integrity of the suspended material. Figure 2h provides a depiction of the rectangular geometry for ease of calculation in data processing. The device, pictured in Figure 3. 2G, exercises a spring-like "push-pull" mechanism and is actuated in situ by an Agilent nanoindenter to quantify the mechanical properties of 2D materials, including rebar graphene. The indenter provides measurements of load and displacement and the tests are video recorded to understand crack propagation. In 1D material tensile tests, platinum deposition is required to adhere the sample to the test shuttles (178, 179). Fortunately, to prevent sliding during tests of 2D materials, no additional deposition of platinum or epoxy is needed because 2D materials adhere to the test shuttle surface by van der Waals forces (98, 154). The stress-strain relationship for the sample depicted in Figure 3. 2H and Figure 3. 2I is shown in Figure 3. 2J. The stress-strain relationship exhibits a linear slope, corresponding to an elastic regime, and an abrupt ending, corresponding to the fracture of

the sample. The rebar graphene samples fracture leading to a zig-zag type fracture surface.

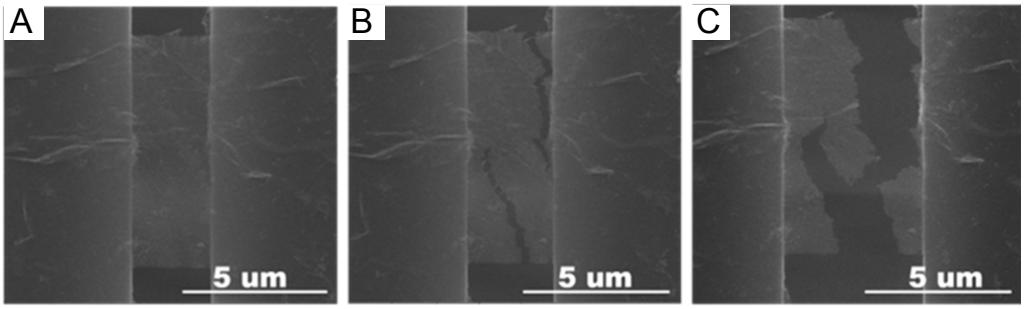

Figure 3. 3 Crack propagation in rebar graphene. (A) Rebar graphene suspended over microdevice before loading. (B) Rebar graphene during tensile loading with zig-zag crack propagation path and multiple crack formation. (C) Fractured rebar graphene showing rough fracture surfaces.

Evidence of a zig-zag crack propagation of rebar graphene is presented in Figure 3. 3. This fracture surface is due to the carbon nanotubes redirecting the motion of the crack and guiding the propagation in a zigzag formation. Pristine graphene fractures in a very linear crack down the center of the sample, as shown in the study by Zhang et al (98). Graphene alone is brittle and exhibits a direct fracture, but rebar graphene shows a fracture pattern that has been stopped and redirected by CNTs. The longer length of the rebar graphene fracture surface compared to that of graphene indicates a higher fracture energy consumption in the rebar graphene samples.

To gain a better understanding of the toughening effects of embedded carbon nanotubes on graphene, a series of fracture tests were performed to measure the critical stress intensity factor (SIF) of this unique material. A center notch, ~10% of the total sample width, was cut into the sample. The equation (3.1) below was used to calculate the critical SIF K_c,

$$K_c = \sigma_c \sqrt{\pi a_0} \tag{3.1}$$

where a_0 is the half notch length and σ_c is the fracture strength.

The modulus and fracture strength are presented in Table 3. 1. It should be noted that most CVD grown graphene constrains certain number of defects, which would weaken graphene. The fracture strength of graphene obtained through tensile tests is less than 10 GPa. Such number is much lower than that of theoretical calculation. The fracture strength of rebar graphene obtained in this study is 6.02±1.53 GPa, which suggests that the existence of CNTs deteriorates the strength of graphene. However, unlike the case of graphene in which the thickness of 0.34 nm was used to calculate the fracture stress and fracture toughness, the thickness of rebar graphene is assumed to be 0.7 nm which is about the diameter of CNTs embedded in graphene. With the thickness discrepancy between graphene and rebar graphene taken in consideration, the fracture strength should be similar. Previous work also demonstrated that single wall carbon nanotubes (SWCNTs) partially unzip during "welding" to graphene. Therefore, the CNTs would not obviously lower the strength of graphene. However, if the boundaries between CNTs and graphene are not well controlled, the strength of rebar graphene could be deteriorated which is reflected in several samples with lower fracture strength and fracture toughness in this study.

The average modulus of the tested un-notched rebar graphene samples is 466.8 ± 29.95 GPa (Table 3. 1) and the average fracture strength of the notched samples is 5.89 ± 1.43 GPa (Table 3. 2). The ranges of fracture strength and elastic modulus of rebar graphene are slightly broad, which could result from small SWCNT bundles, holes, and residual stress in rebar graphene. We examine TEM images of rebar graphene and believe that there are two sources resulting in large spread of mechanical performance of rebar graphene. (1) The SWCNTs were treated by alkaline and supposed to exhibit high solubility in chloroform, THF, and DMF. However, once we spread them on Cu substrate,

small SWCNT bundles may form. (2) In our study, dry transfer technique was developed and used to transfer rebar graphene onto micromechanical device. However, samples could be damaged after removing PMMA annealed at 400 °C with protection gas of H2/N2. Once there is residual stress in rebar graphene, defects could be created after annealing. Another concern is that the thermal expansion of device shuttles could result in large stress which would lead to damage as well. Note that the thickness of 0.7 nm was used to calculate the elastic modulus, fracture strength, and SIF of rebar graphene due to the nonuniformity of rebar graphene. More detailed discussions on the strength and stiffness of rebar graphene could be found in the supporting information. The SIF values determined by these experimental tests are presented in Table 3. 2. In comparison to similar studies performed on pristine graphene, the average SIF of rebar graphene is clearly much higher. This can be explained by the ability of the CNTs to constrict and divert the propagation of the crack.

Sample Number	Total Strain (%)	Young's Modulus (GPa)	Fracture Strength (GPa)
B1	1.16	431.69	4.89
B2	3.84	461.6	15.1404
B3	0.65	490.97	2.8572
B4	0.41	324.84	1.354
B5	2.30	415.95	6.9182
B6	2.43	527.65	8.0768
B7	2.36	614.9	2.933
	Average	466.8 ± 29.95	6.02 ± 1.53

Table 3. 1 Mechanical properties of suspended rebar graphene (A measured average thickness of 0.7 nm is used here)

Sample Number	Flaw Ratio (%)	Total Strain (%)	Fracture Strength (GPa)	Stress Intensity Factor (MPa$\sqrt{m}$)
A1	8.53	1.33	5.08	7.23
A2	12.34	0.93	3.73	6.99
A3	15.92	2.13	2.41	4.43
A4	14.43	2.17	5.57	10.61
A5	38.09	4.65	2.65	8.30
A6	18.24	3.54	12.81	21.18
A7	13.58	2.01	9.00	14.75
		Average	5.89 ± 1.43	10.50 ± 2.16

Table 3. 2 Geometry of initial crack length with respect to total sample width compared to stress intensity factor as calculated by the Griffith theory. (A measured average thickness of 0.7 nm is used here)

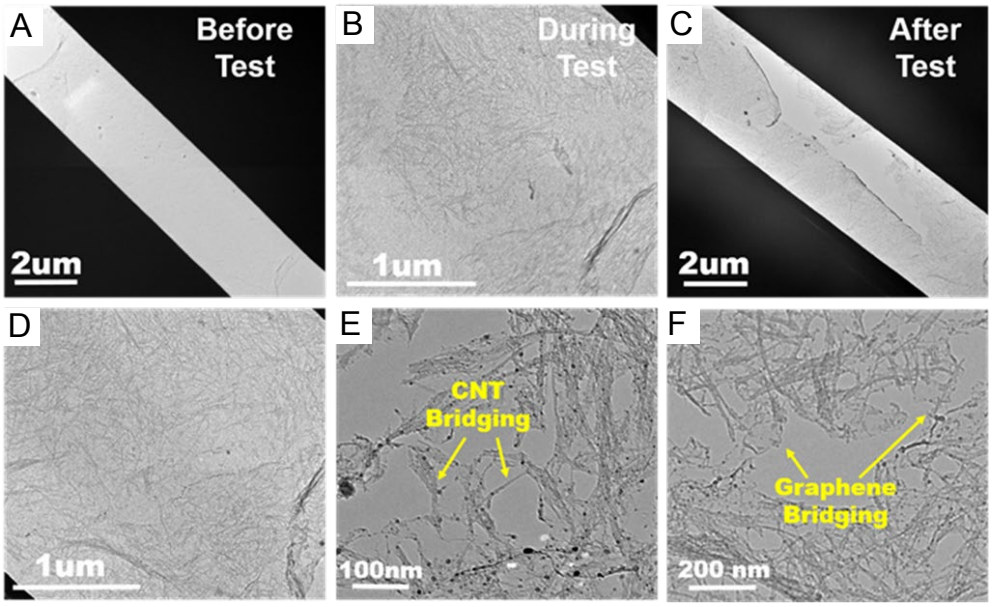

Figure 3. 4 In situ tensile test of rebar graphene in TEM. (A) Rebar graphene suspended over microdevice before tensile test. (B) Rebar graphene at the onset of fracture. (C) Overview of fractured rebar graphene. (D-F) Fractured rebar graphene with pulled-out CNTs, CNT bridging, and graphene bridging.

The *in situ* SEM tensile tests enable us to quantify the elastic modulus, fracture strength, and fracture toughness of rebar graphene. The critical SIF is over twice as much as that of graphene. To unveil the mystery behind the improved mechanical properties and

to understand the interaction between CNTs and graphene as well as between the initial crack and CNTs, we performed *in situ* tensile tests of rebar graphene in TEM shown in Figure 3. 4. A piece of rebar graphene was first transferred onto the TEM microdevice using the same transfer technique mentioned above. Figure 3. 4A shows that the TEM image of rebar graphene firmly adhered to the TEM microdevice. There are several holes in the rebar graphene, which might have resulted from the dry transfer. However, the pre-existing holes can be considered an initial notch to observe crack propagation during the tensile test. The uniaxial tensile test was actuated by joule heating. Figure 3. 4B captures the moment of fracture of rebar graphene at which the crack went through the observed hole and was also greatly deflected. The crack deflection is desired for material toughening since more energy could be dissipated during the fracture process, leading to the enhancement of mechanical performance of rebar graphene. Figure 3. 4C shows an overview of the fractured rebar graphene. Unlike fractured CVD grown graphene with a single straight crack line, there are several cracks in the fractured rebar graphene. This observation suggests multiple locations for crack initiation that inhibit the momentum of the primary crack driving force. Such phenomenon is also reflected by the different maximum strains between CVD grown graphene and rebar graphene. The maximum strain for CVD grown graphene is only 0.3% (98), while the average maximum strain of rebar graphene is up to 1.5%. More fracture details in Figure 3. 4D-F were investigated to understand the reinforcing mechanism. Some fractured shrinking tips of CNTs can be found in Figure 3. 4E and F. The shrinking tips demonstrate that the CNTs bridged the crack growth before the catastrophic failure. The CNT bridging dominates the rebar graphene fracture surface, which successfully retard the crack growth in mechanical failure

of rebar graphene shown in Figure 3. 4E and F. The graphene bridging is also found in Figure 3. 4E and F complementing the enhancement of toughness of rebar graphene. In addition to the above reinforcing phenomena, the pulled-out CNTs can be observed around the fracture surface in Figure 3. 4E and F, which is another reinforcing mechanism to improve the fracture toughness of materials. With the above observed reinforcing mechanisms, more energy could be consumed before final failure, which promotes the toughness of rebar graphene.

3.2.2 Results of MD simulations

To validate the hypothesized toughening mechanisms and unveil more details of the fracture process in rebar graphene, we have constructed full-atom models of rebar graphene with typical distributions of CNTs. MD simulations of crack propagation and uniaxial tension tests of rebar graphene nanostrips were carefully performed. The rebar graphene samples are built by connecting CNTs with a diameter of 1 nm and length of 11 nm to a graphene layer through sp^2 covalent bonds (Figure 3. 5A). As the representative examples, only the CNTs lying along the vertical loading direction are presented here and several typical CNT distribution patterns, including the regular staggered pattern, inclined staggered pattern and random staggered pattern, are discussed respectively (Figure 3. 5B). More discussions about the effect of the varying geometry and distribution of CNTs on the toughness enhancement could be found in the next section.

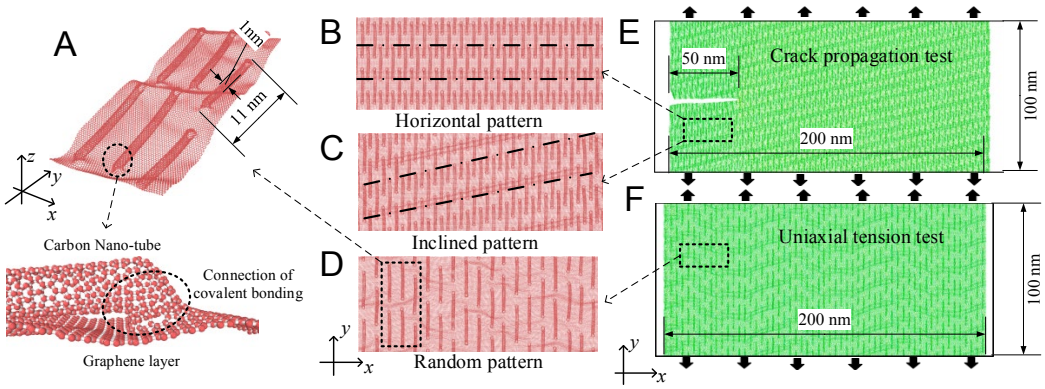

Figure 3. 5 Molecular Dynamics simulations of uniaxial tensile fracture tests of rebar graphene samples. (A) The atomic structure of rebar graphene samples. CNTs with a diameter of 1 nm and a length of 11 nm are connected to a graphene layer through sp2 covalent bonds to represent rebar graphene samples. (B-D) Different distributions of reinforcing CNTs lying along the y direction. A regular staggered pattern (B), an inclined staggered pattern (C) and a random staggered pattern (D) are constructed. (E-F) MD simulations of crack propagation and uniaxial tension of rebar graphene nanostrips.

After the full atomic arrangement of the rebar graphene structures are obtained, we performed MD simulations of relaxation and uniaxial tension in rebar graphene strips 200 *nm* in length and 100 *nm* in width, with/without a 50 *nm* long edge crack initially (Figure 5c). An initial relaxation under an NPT ensemble with Nose-Hoover thermostat (143) at 0 *Pa* and 300 *K* for 50 *ps* was performed first to make sure the rebar graphene models are thermodynamically stable. Then to perform the mechanical test, a tensile loading with a constant strain rate of 10^9 s^{-1} was applied by deforming the simulation box in the *y* direction. During the test, periodic boundary condition was applied in the *y* direction and an NVT ensemble with Nose-Hoover thermostat was adopted to maintain a constant temperature of 10 *K*. Note that the length of the CNTs and the size of rebar graphene strips in these MD models are smaller than those of the experimental samples mainly due to the limitation of current simulation power. Nevertheless, it appears that the interaction between CNTs and graphene and the distribution of CNT network are reasonably captured by the MD

simulations, which prove to play the key roles in achieving the observed toughening mechanisms in rebar graphene.

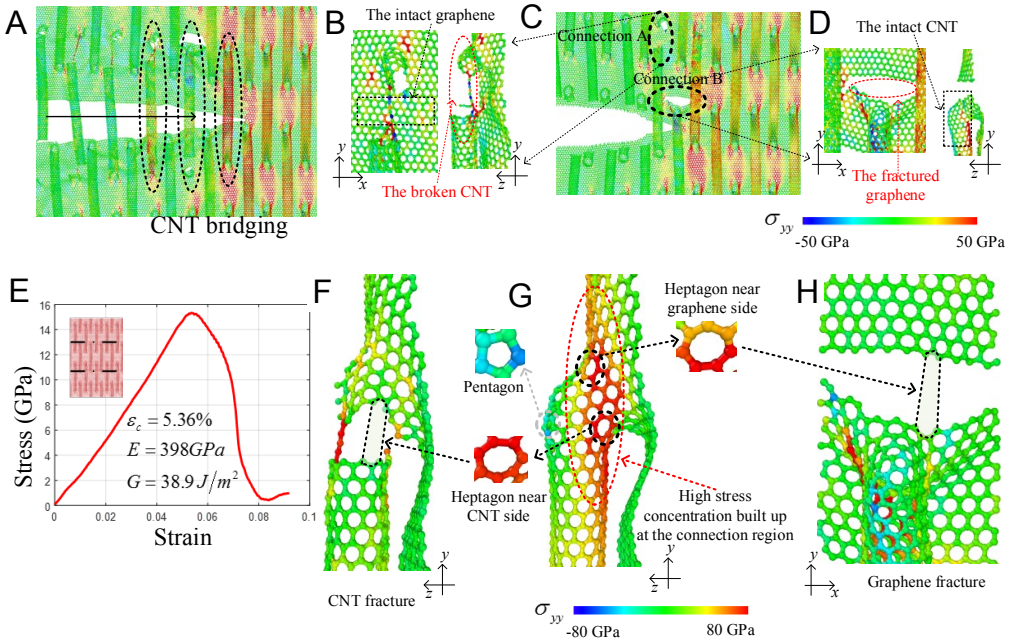

Figure 3. 6 Molecular Dynamics simulations of CNT bridging in rebar graphene samples. (A) MD simulation of crack propagation in a rebar graphene with CNTs in a regular staggered distribution pattern. The CNTs bridge the crack surfaces and fail as the crack propagates and the measured fracture toughness is enhanced. (B-D) Two failure modes of the bridging CNTs. The CNT could break leaving the graphene layer intact (top view and side view shown in b), or the graphene layer fractures with the CNT unbroken (top view and side view shown in d). (E) The stress-strain curve of the crack propagation test in a rebar graphene with CNTs in a regular staggered distribution pattern. The measured fracture energy, G is 38.9 J/m2, larger than that of graphene, 11.9 J/m2, obtained via MD simulations. (F-H) Local stress distribution and atomistic configurations at the connection region between CNT and graphene in rebar graphene model. Heptagons with high stress concentration (g) initiates local fracture process resulting in either CNT breaking (F) or graphene fracture (H).

MD simulations of crack propagation were performed in rebar graphene samples (Figure 3. 5E) to investigate the interaction between CNTs and crack. The results demonstrate that the crack could be bridged and/or deflected by CNTs in rebar graphene. Figure 3. 6A shows that as the loading increases, along the crack path stress is transferred

by the CNTs which bridge the two crack surfaces, postponing the main crack propagation. The crack propagates only when the bridging CNTs are broken or pulled out, leading to a strong bridging effect (Figure 3. 6E) of the CNTs perpendicular to the initial crack path. The ending of individual CNT bridging (Figure 3. 6C) results from either the breaking of the CNT (Figure 3. 6B) or the daughter crack initiation in the connected graphene layer (Figure 3. 6D). These two localized, atomistic fracture events can be related to the local stress distribution and local atomistic configurations (i.e. the topological defect structures). As shown in Figure 3. 6G, when the CNT bridges the crack surfaces, high stress concentration builds up at the connection region between the CNT and the graphene layer. Locally, to accommodate the curvature change from the cylindrical CNT to flat graphene, there are positive and negative disclinations (pentagon and heptagon rings) at the connection spots. Previous studies have shown that the heptagon rings are weak spots for bond breaking in graphene and our simulations demonstrate that both failure modes, CNT breaking (Figure 3. 6F) or graphene fracture (Figure 3. 6H), initiate at these heptagon rings (51, 71). However, regarding the competing of the two local failure modes, no dominant trend is observed in the simulations. This is consistent with the experimental observation of both CNT pull-out and graphene bridging. It should be pointed out that the detailed atomistic configurations around the connection of CNTs and graphene layer remain unknown in experiments and the simulation model adopted here may still be different from the reality. Further advanced experimental observation and systematic simulations about the connection spots in rebar graphene may unveil more details about these failure modes to tune the bridging mechanism and are left for future study.

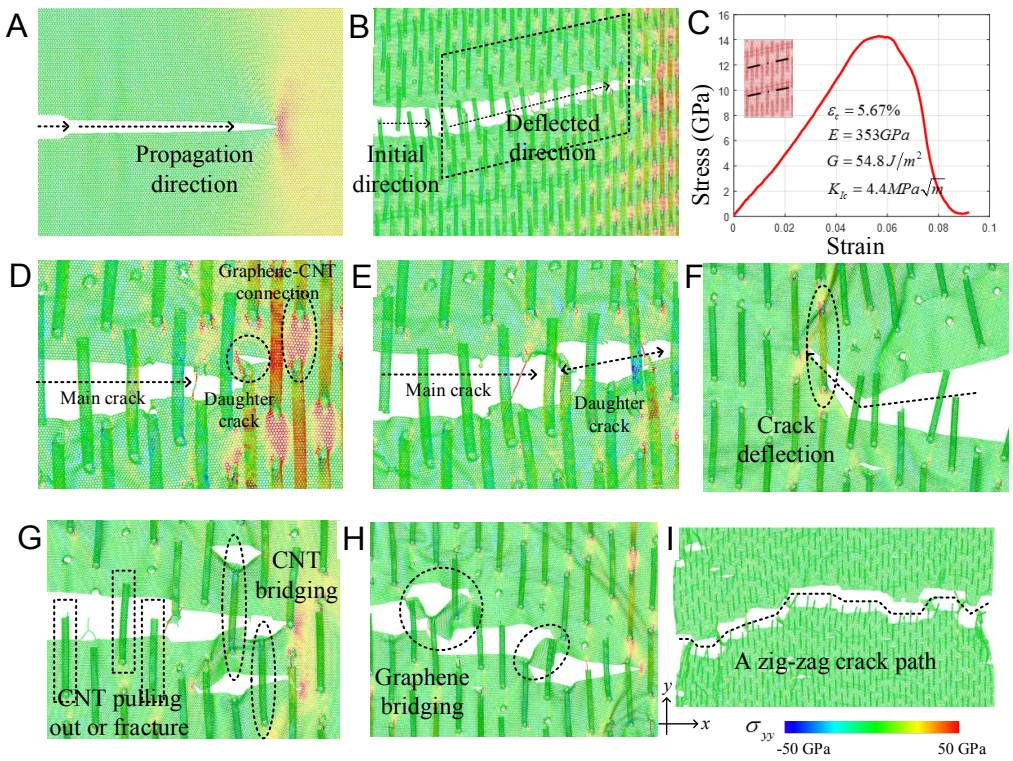

Figure 3. 7 Molecular Dynamics simulations of toughening mechanisms in rebar graphene samples. (A) MD simulation of crack propagation in pristine graphene. A straight crack path with smooth crack surfaces are observed. (B-C) MD simulation of crack propagation in a rebar graphene with an inclined staggered distribution of CNTs. The initial horizontal crack is deflected due to the bridging and breaking of a series of CNTs along the inclined direction. A more than four-fold enhancement of fracture energy is achieved compared with graphene in MD. (D-E) One step in crack deflection through daughter crack initiation (D) and crack coarsening (E). (F) Crack deflection through strong bridging in a rebar graphene with random staggered CNT pattern. (F-H) MD simulation of uniaxial tension test of a rebar graphene sample with a random staggered CNT pattern. CNT bridging, pulled out or fractured CNTs, crack defection and graphene bridging are observed during the fracture process and finally a zig-zag crack path cuts through the whole strip.

MD simulations also show that the CNTs in rebar graphene could deflect the crack path through daughter crack initiation and coarsening and crack bridging. For purposes of comparison, we simulated crack propagation in pristine graphene along zigzag direction using MD as well. As shown in Figure 3. 7A, the crack propagates along a straight line in pristine graphene leaving smooth crack surfaces behind, which is consistent with previous

studies (98). However, in rebar graphene, for example, when the CNTs are oriented inclined with an angle to the initial crack path, as shown in Figure 3. 7B for the sample with inclined CNT pattern, a series of effective bridging events happen along the CNT distribution direction, resulting in the deflection of the crack path during the propagation, which further enhances the fracture energy of rebar graphene (Figure 3. 7C). The detailed crack defection mechanisms demonstrated in this example are daughter crack initiation and crack coarsening. As shown in Figure 3. 7D, the connections between CNTs and graphene often suffer high stress concentration and daughter cracks can initiate at these spots. Later, these secondary cracks coarsen and merge into the main crack, achieving a small "jump over" of the crack path (Figure 3. 7E). A sequence of such interaction could deflect the crack path away from the original direction (Figure 3. 7B). Another crack deflection mechanism in rebar graphene is crack bridging. As shown in Figure 3. 7F, strong CNT bridging in a rebar graphene sample with a random staggered pattern of CNTs can also deflect the crack path.

To unveil more details of fracture process in rebar graphene, uniaxial tension tests are performed in rebar graphene strips with a random CNT pattern (Figure 3. 5F). Without an initial edge crack, multiple cracks initiate at different locations, propagate and interact with each other, resulting in a rich variety of crack initiation and propagation processes. Figure 3. 7F-I show that CNT bridging, CNT pulling out/fracture, crack deflection, graphene briging are all captured by the simulation and finally a zig-zag crack path forms in the sample, which are consistent with the experimental observation in Figure 4 and further validate the hypothesized toughening mechanisms of rebar graphene in a qualitative way.

Due to these novel toughening mechanisms activated in rebar graphene, the fracture

toughness measured in MD simulation also show obvious enhancement. As a comparison, for pristine graphene, we obtained a fracture energy of 11.9 J/m^2 and a critical SIF of 3.5 $MPa \cdot m^{1/2}$ using MD simulation, which is in good agreement with previous study (98). The rebar graphene model with an inclined staggered pattern of CNTs discussed above shows a fracture energy of 54.8 J/m^2 and a critical SIF of 4.4 $MPa \cdot m^{1/2}$ which achieves a more than four-fold enhancement in fracture energy.

We also note that the experimental measured value of the critical SIF of rebar graphene reaches an average of 10.5 $MPa \cdot m^{1/2}$, which is still relatively larger than the simulation results. Qualitatively this discrepancy could be related to the following factors. Due to the limitation of current computational power, the rebar graphene models adopted in MD simulations are considerably smaller than those in real experiments. Correspondingly, the length of CNTs and the complexity of the CNT networks are all reduced and simplified to adjust to the available simulation size. Quantitatively, this scaling down could limit the effect of toughening mechanisms, reduce the size of the processing zone surrounding the crack tip and lead to an underestimated fracture resistance. What's more, under current experimental condition, the detailed observation of the distribution of the CNT network and the atomistic configurations of the connections between CNTs and graphene layer in rebar graphene remain unknown. There could be different distribution patterns and connection configurations in the experimental samples. As demonstrated in current MD simulations, the CNT network distributions and the defect structure at the connections could affect the toughening mechanisms directly and alter the fracture toughness quantitively. For future study, it is important to combining the advanced experimental observation with MD simulations to construct a quantitative relation between

the toughness enhancement and rebar graphene structures.

3.2.3 Effect of the geometry and distribution of CNTs on toughening

The rebar graphene sample we studied in the experiments show certain randomness in the geometry and distribution of CNTs. Under current experimental techniques, there is still a lack of effective ways to fabricate rebar graphene with well controlled/designed CNT network in the laboratory. So, it remains a challenge to characterize the effect of CNT geometry and distribution on the enhancement of toughness directly. Alternatively, we performed MD simulations on rebar graphene models with controlled geometry and distribution in hope to shed some light on the possible effect of CNT's geometry and distribution on the toughening effect in rebar graphene.

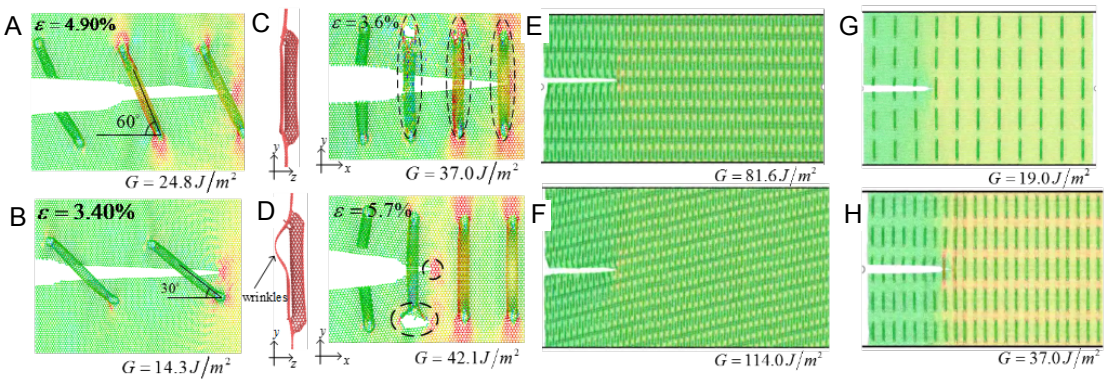

Figure 3. 8 The effect of the geometry and distributions of CNTs on toughening effect in rebar graphene via MD simulations (*G* denotes the measured fracture energy in MD simulations and equivalent to fracture toughness. For the purpose of comparison, a uniform thickness of 0.34 nm is adopted for all examples here). (A-B) The effect of the relative orientation of CNTs with respective to the crack path. CNTs lying closer to the vertical directions show better bridging effect. (C-D) The influence of the length mismatch between CNTs and graphene layer. Wrinkles in graphene layer help to improve the bridging effect of CNTs. e-f. The effect of CNT distribution patterns. The inclined pattern (F) shows better fracture energy than the regular one (E). (G-F) The influence of CNT density. Higher density of CNT network yields better fracture resistance.

Via MD simulations, we find that the toughness enhancement in rebar graphene could be influenced by the orientation of CNTs, the length mismatch between CNTs and the graphene layer, the density and distribution patterns of CNT networks. For example, when bridging the crack surfaces, the CNTs whose orientations are closer to the perpendicular direction of the crack path show better toughening effect (Figure 3. 8A and B) because the CNTs tend to first rotate to the orientation perpendicular to the crack path before bridging the crack surfaces effectively. Due to the possible wrinkles in the graphene layer, there could be some length mismatch between CNTs and the graphene layer lying beneath (Figure 3. 8D). MD simulations show that such length mismatch could also affect the toughening effect. For instance, the extra length in graphene layer/insufficient length of the CNTs could make CNTs bear more load at the early stage of deformation and enhance toughening effects (Figure 3. 8C and D). What's more, the density and distribution pattern of CNTs can also alter the measured fracture energy of the samples. As discussed in the previous section, the rebar graphene with an inclined staggered distribution of CNTs demonstrated a better fracture energy than that with a regular staggered CNT distribution because of the toughening mechanism of crack deflection triggered by the CNT distribution pattern (Figure 3. 8E and F). Under the same distribution pattern, a higher density of CNTs usually yields a better fracture energy (Figure 3. 8G and F). These preliminary results strongly imply that there could be direct connections between the toughness enhancement and the geometrical parameters of CNT network. And the toughness of rebar graphene may be tuned and even optimized through designing the CNT network. A systematic study of the quantitative relation between fracture toughness enhancement and the geometry of CNT network is calling for more research efforts in the future.

3.3 Conclusions

The previous study (98) demonstrates that the fracture toughness of graphene is only 4.0 $MPa \cdot m^{1/2}$, which suggests that graphene is a typical brittle material. Considering that graphene has a great potential in building flexible devices, in case of resisting mechanical failure, graphene-like materials with higher fracture toughness is in need. Rebar graphene is the graphene toughened by CNTs. The measured fracture toughness is over twice higher than that of pristine graphene. Such promising fracture toughness would make rebar graphene find more practical applications. For example, rebar graphene could be a very good candidate material for flexible transparent conductive electrodes (180). In flexible electronics, once the electrode is under tension, compression, and twisting, the mechanical behaviors of electrode materials will dominate the reliability and stability of the device. Also, the rebar graphene can be used to fabricate 3D rebar graphene foams, which have demonstrated stable performance as a highly porous electrode in lithium ion capacitors (180). Another significance of our work is that through the measurement and study of fracture toughness enhancement in rebar graphene, materials with exceptional mechanical performance might be discovered and designed in the future. For example, the unveiled toughening mechanisms in rebar graphene may be applied to design and engineer other tough 2D material systems as hybrids of 2D planar sheets and 1D nanotubes, like rebar hexagonal-boron nitride (h-BN) and even rebar transition metal dichalcogenides (TMDs).

In conclusion, we have performed quantitative *in situ* mechanical tests and numerical simulations on rebar graphene in comparison with similar tests done on pristine graphene and determined toughening mechanisms of the embedded carbon nanotubes. Such tests and

study are imperative to understanding and enhancing mechanical properties of 2D materials before their integration into robust electronic devices. The CNTs toughen the graphene as seen by the increased average SIF values obtained. This is further seen in a comparison of the nature of the crack propagations in graphene and rebar graphene. Graphene fractures in a linear, brittle manner where graphene rebar displays a zigzag fracture surfaces, guided and redirected by the embedded CNTs. The creation of this hybrid graphene material opens the door to many other 2D composites that can be mechanically tailored to the needs of their flexible device applications.

Chapter 4

Engineer energy dissipation in 3D graphene nanolattice via reversible snap-through instability

Chapter Summary

Carbon micro/nanolattice materials, defined as three dimensional (3D) architected metamaterials made of micro/nanoscale carbon constituents, have demonstrated exceptional mechanical properties, including ultrahigh specific strength, stiffness and extensive deformability through experiments and simulations. The ductility of these carbon micro/nanolattices is also important for robust performance. In this work, we present a novel design of using a reversible snap-through instability to engineer energy dissipation in 3D graphene nanolattices. Inspired by the shell structure of flexible straws, we construct a type of graphene counterpart via topological design and demonstrate its associated snap-through instability through molecular dynamics (MD) simulations. One-dimensional (1D) straw-like carbon nanotube (SCNT) and 3D graphene nanolattices are constructed from a unit cell. These graphene nanolattices possess multiple stable states and are elastically reconfigurable. A theoretical model of 1D bi-stable element chain is adopted to understand the collective deformation behavior of the nanolattice. Reversible pseudo plastic behavior with a finite hysteresis loop is predicted and further validated via MD. Enhanced by these novel energy dissipation mechanisms, the 3D graphene nanolattice shows good tolerance of crack-like flaw and is predicted to approach a specific energy dissipation of 233 kJ/kg

in a loading cycle with no permanent damage (one order higher than the energy absorbed by carbon steel at failure, 16 kJ/kg). This study provides a novel mechanism for 3D carbon nanolattice to dissipate energy with no accumulative damage and improve resistance to fracture, broadening the promising application of 3D carbon in energy absorption and programmable materials.

4.1 Introduction

Carbon micro/nano lattices are a unique family of architected metamaterials constructed from micro/nano-scale carbon constituents (181). During the past few years, they have demonstrated exciting potentials in reaching theoretical limits of mechanical performances as well as integrating properties which are often mutually exclusive through experimental studies and numerical simulations (86, 182-187). For example, the glassy carbon nano-honeycomb lattice fabricated through pyrolysis of polymeric microlattice has reached a compressive strength of 1.2 GPa at a density of 0.6 g/cm^3, approaching the lower bound of the theoretical limit set by the bulk glassy carbon (86). Pyrolytic carbon nanolattices with topologies of octet- or iso-truss have been demonstrated to possess a combination of high specific strength, low density, extensive deformability and flaw tolerance, which are properties, in general, mutually exclusive in conventional materials (182). The record-breaking performances of these carbon nanolattices are boosted by at least two factors: the size-dependent properties of the constituents and the well-designed lattice architecture (181). By reducing the length scale of the components, such as beams or cell walls, to nanoscale, the constituents unlock the properties which are close to their theoretical values. For example, combining theoretical, computational and experimental studies (188-190), researchers have predicted that the critical size for pyrolytic carbon

being flaw tolerant is about ~490 nm (182). Experimental studies confirm that for carbon nanolattice with a characteristic length (diameters of the struts) below this size, local failure of the constituents becomes flaw insensitive, reaching the theoretical strength of bulk carbon materials (86, 182). The benefit of being small is further coupled with the well-designed lattice architectures, resulting in richer and more balanced combinations of desired properties. For instance, via a systematic computational study of 3D graphene in the topologies of triply periodic minimal surfaces (TPMSs), it has been demonstrated that topology can strongly affect the elastic properties and failure mechanisms of graphene nanolattices (183, 184). In short, the combination of small-scale carbon constituents and unlimited architecture designs of lattice opens a broad exploration space for better material properties in carbon nanolattices.

Besides pursuing high specific strength, ductility is also particularly important to carbon nanolattices for robust performances (186). At the material level, the carbon constituents are intrinsically brittle. Including bulk glassy carbon (86, 185), the basic material building block of most carbon nanolattices is graphene, a two-dimensional (2D) atomically thin layer of carbon atoms connected by sp2 hybrid covalent bonding (191). As one of the strongest known materials, graphene has a theoretical strength of 130 GPa (33) (two orders larger than that of bulk glassy carbon, 2~3 GPa (86)). However, experimental studies have unveiled that the fracture toughness of graphene is only 16 J/m^2 (192), which is close to that of an ideally brittle solid (193). As the characteristic length of carbon nanolattices falls smaller to make use of the ultrahigh strength of graphene, it is also important to enhance the toughness and ductility of the nanolattices. At the structure level, buckling is an important mechanism to dissipate energy in nanolattice materials under

compression (194-196). However, permanent and continuous damage often accompanies buckling events. For example, it is observed that for hollow metallic and ceramic microlattices, the hysteresis loops of stress-strain curves shrink as the number of loading cycles increases, especially over the first few cycles (196, 197). Also, while being accessible under compression (198, 199), buckling can have much limited effect on energy dissipation under tensile loading. For instance, MD simulations have demonstrated that under tension, graphene nanolattices, such as graphene gyroids, dissipate energy mainly through crack nucleation and propagation, which accumulates permanent damage and degrade the material systems (183, 184). Given the great potentials of carbon nanomaterials, it is important to enrich the design library of carbon nanolattices with examples of novel energy dissipation mechanisms in order to overcome this challenge.

Like buckling, snap-through instability has been a long-time research topic (200-207). Recent studies unveil some unique advantages of this instability. On one hand, at macro-scale, by carefully designing and arranging the snap-through units in metamaterials, sequential snap-through instabilities can be triggered under not only compressive but also tensile loading conditions (203, 206). Cyclic loading tests demonstrate that these built-in instabilities suffer little irreversible damage (206). Metamaterials with snap-through instability often exhibit multiple mechanically stable states, which open doors to the design of shape-reconfigurable materials (SRMs) (203). On the other hand, at small scales, basic conceptual units with mechanically bi-stable states and snap-through instability (208-211) have been adopted to explain deformation behaviors of phase transforming materials, including structure proteins with compactly folded or unfolded domains (212, 213) and shape memory alloys undergoing martensitic phase transformation (214). Such universal

structure-to-property relationship indicates great potential in engineering complex overall deformation behavior via bi-stable units and snap-through instabilities.

The present study is aimed to address the challenge of toughening carbon nanolattice with the potential of snap-through instability in engineering overall material behavior. Through mechanism-inspired structure design, MD simulations and theoretical analysis, we present a novel design of 3D graphene nanolattice with snap-through instability and demonstrate that it can effectively dissipate deformation energy without accumulating irreversible damages via pseudo plastic deformation.

3.2 Results

3.2.1 Unit cell design

We choose 2D graphene as a basis for our nanolattice design due to its outstanding mechanical properties. To adapt to the 2D geometry of graphene, we focus on shell-based designs

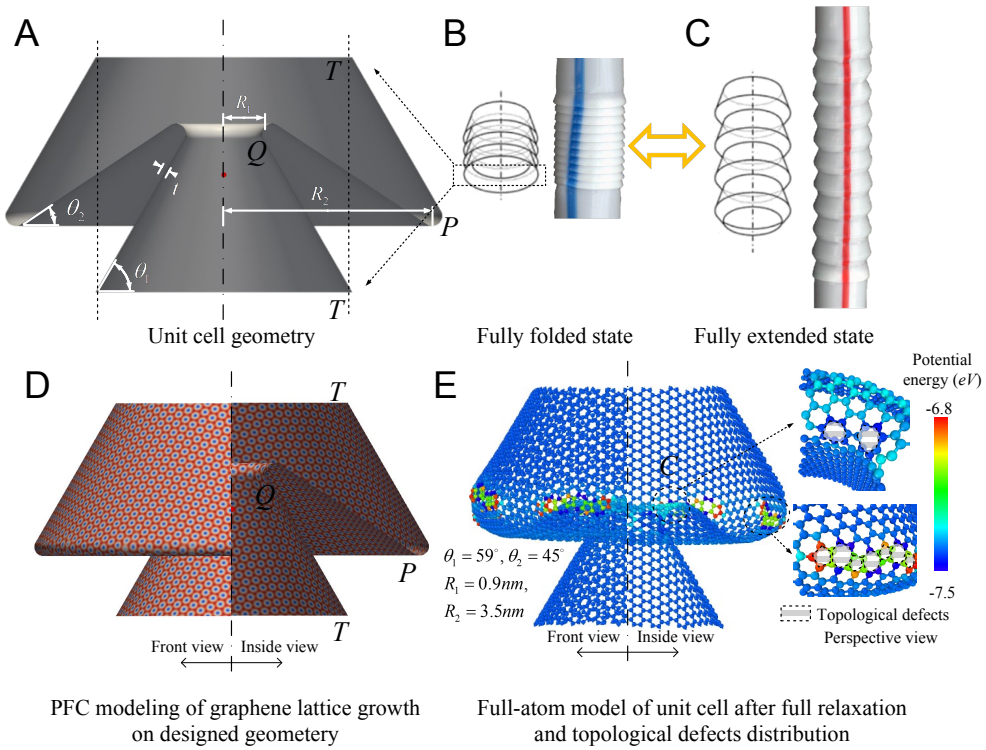

Figure 4. 1 Unit cell of shell structure in flexible straws and its nanoscale graphene counterpart engineered via topological design. (A) Geometry of the unit cell structure in straws. (B-C) The fully folded and fully extended states of flexible straws. (D) Phase field crystal simulation of a 2D crystal sample growing on the designed shell surface. (E) The atomic structure of the graphene unit cell with straw-like geometry after MD relaxation and the topological defects distributed at the inner and outer folds.

At macroscale, numerous applications and studies have presented various examples of shell structures with snap-through instabilities (215-220). Here, we borrowed inspiration from one of the simplest cases, the flexible straw (221, 222), which can change length by transforming between the folded state and the extended state (Figure 4. 1B and C). As shown in Figure 4. 1A, the unit cell structure of such a flexible straw is a pair of intersecting conical frustra (the outer frustum, Q-T-P and the inner one, Q-P, intersecting at the folds P and Q). By designing the geometrical parameters of the unit cell, a recent study (223) has demonstrated that both the axially folded state and the extended state can be mechanically

stable (Figure 4. 1B and C) for elastic shells. Here, we constructed a full-atom model of graphene counterpart to such a unit cell by taking advantage of the methodology of topological design (54, 71, 224). As shown in Figure 4. 1D, phase field crystal modeling (141, 142, 225) was adopted to simulate the growth of 2D crystal on the designed geometry of the conical frustra. The thermal stability of the obtained crystal structure was validated by relaxing it under an NPT ensemble with Nose-Hoover thermostat (226) at 0 Pa and 300 K for 50 ps using MD. The dimensions of the relaxed sample are listed in Fig. 1 e. It should be noted that even through the relaxed model does not fully conform to the designed geometry (Figure 4. 1D), the straw-like topology is stably maintained (Figure 4. 1E). Further inspection showed that topological defects (68, 224), such as disclinations and dislocations, only concentrate at the connections of the two frustra, accommodating and stabilizing the curvature transition (Figure 4. 1E). The inevitable presence of topological defects, their residual stress (54) as well as the Van der Waals (VdW) interactions (227) between graphene frustra make the atomic sample different from its counterpart at large scale.

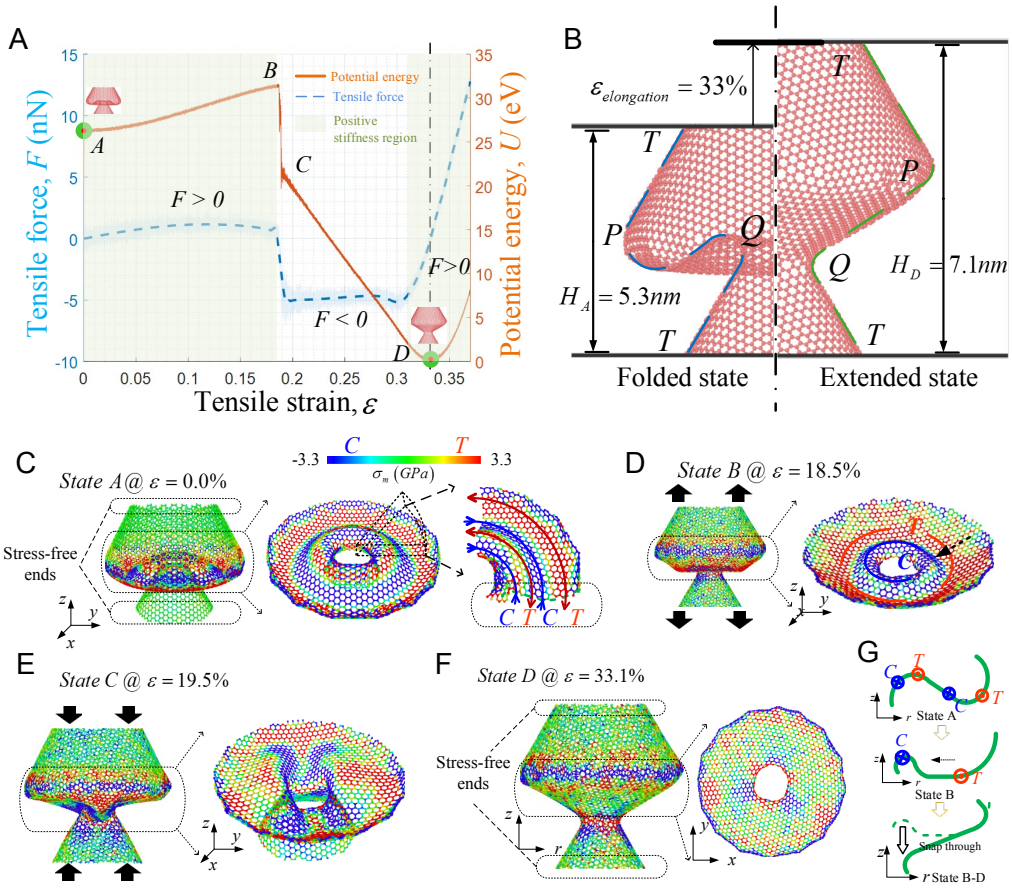

Figure 4. 2 The two stress-free stable configurations of the unit cell and the process of a snap-through event. (A) The force-strain and potential energy-strain curves of the unit cell transforming from the folded state to the extended state. (B) Geometry of the two loading-free equilibrium configurations of the unit cell. The two halves of the unit cell are in the folded and extended states, respectively. (C-F) Snapshots of a snap-through event during a tension test in MD simulation. (G) 2D sketch of the deformation process of the inner frustrum during the snap-through process.

To explore the snap-through instability and possible mechanically stable states of such straw-like unit cells, uniaxial tension tests were performed by applying a constant strain rate of 10^8/s to the simulation box along the axial direction. During the test, a periodic boundary condition was applied along the axial direction and an NVT ensemble with Nose-Hoover thermostat (226) was adopted to maintain a constant temperature of 10 K. The force-strain and potential energy-strain curves are shown in Figure 4. 2A. The potential

energy curve shows two parabolic-like parts centered around the folded state (State A) and the extended state (State D), indicating both states have positive stiffness. Relaxation and loading tests via MD demonstrated they are mechanically stable. In the transition region, the force curve suffers a non-positive derivative, resulting from the snap-through instability and the corresponding negative incremental stiffness. Through the snap-through instability, the unit cell achieves a 33% elongation without any irreversible damage to the crystal structure (Figure 4. 2B). Careful inspection showed that the snap-through event mainly takes place at the inner frustum (P-Q in Figure 4. 2B) with the outer frustum (Q-T-P in Figure 4. 2B) serving as a constraint to its deformation. At the folded state, the inner frustum is already self-stressed under no external loading (Figure 4. 2C). As the external tension increases, the highly compressive stress state is pushed toward the inner fold, Q (Figure 4. 2D). At the critical moment, the axial-symmetry of the deformation is broken (Figure 4. 2E) and the inner frustrum flips out (Figure 4. 2F), resulting in a snap-through event (Figure 4. 2G). Compared to the folded state (Figure 4. 2C), the residual stress in the inner frustrum is reduced in the extended state (Figure 4. 2F). Correspondingly, the potential energy in the extended state is lower than that of the folded state (Figure 4. 2A) even through the two share the same atomistic topology. In short, the straw-like unit cell possesses two mechanically stable states and can snap-through between them under tension, suffering no permanent damage. It is also interesting to note that similar bi-stable states and snap-through events have been studied in shell systems at macroscale. For example, via experiments and finite element simulations, mirror buckling and snap-through events in spherical cap shells have been studied, where it is demonstrated that the initial asymmetrical buckling can make the snap-through more robust (219). Recently, an energy

landscape analysis is conducted for cylindrical shells. Such detailed energy landscape proved to be an insightful guidance for designing controllable buckling paths between different states (220). Inspired by these advances in shell buckling study, we wish to point out that it is very likely the straw-like unit cell presented here can be further tuned for more optimized mechanical behavior. For instance, by adjusting its geometrical dimensions, defect/imperfection distributions and residual stress fields, the unit cell may demonstrate a higher stress level for snap-through transition and a larger elongation between the folded and the extended states. We leave this optimization to a future study and focus on the coupling between the unit cell behavior and the lattice level design in the current study.

In the following section, we combine the unit cell with different lattice designs to construct 1D and 3D graphene nanolattices and study their collective deformation behaviors, aiming at engineering effective energy dissipation by leveraging the effect of the snap-through instability.

4.2.2 Lattice design: 1D and 3D

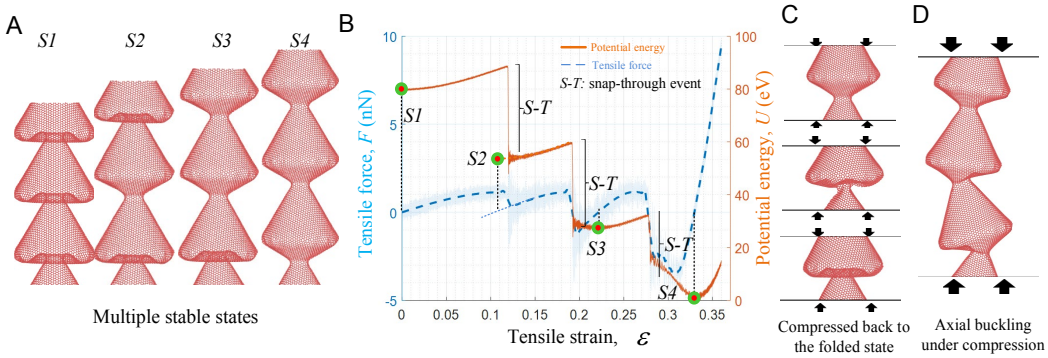

Figure 4. 3 1D lattice design: a straw-like CNT. (A) The four stress-free equilibrium configurations with different lengths. (B) Force-strain and potential energy-strain curves during transition from the fully folded stated to the fully extended state under tension via MD. (C) One unit cell compressed back to its folded state without suffering axial buckling. (D) Axial buckling of the SCNT with three unit cells

under compression.

Straightforwardly, by repeating the unit cell along the axial direction, we obtain the 1D lattice of a straw-like CNT (SCNT). Because each unit cell within the SCNT can choose either the folded state or the extended state, the SCNT sample can have multiple mechanically stable states. Under tensile loading along the axial direction, the SCNT can transform through these states and achieve different axial lengths, making it a reconfigurable 1D nanolattice. We validated this capability via MD simulations. One example SCNT with three unit cells is transformed from the fully folded configuration to the fully extended state under tensile loading in MD. As shown in Figure 4. 3, four different equilibrium lengths are identified from MD (Figure 4. 3A). During the tensile loading process, they are separated by discrete snap-through events of individual unit cells (Figure 4. 3B). At each instability event, the stored strain energy (orange solid line in Figure 4. 3B) is partially released and dissipated into the environment via thermal vibrations. Correspondingly, the loading force drops, leaving a saw-teeth like force-strain curve (blue dash line in Figure 4. 3B).

One limitation for this 1D nanolattice of SCNT is that it can be hard to transform the extended configuration back to the folded one due to global axial buckling of SCNT under compression. As shown in Figure 4. 3C and D, under compression, even though the straw-like unit cell can snap back to the folded state, the SCNT with three unit cells buckles along the axial direction before the backward snap-through can happen. This asymmetry in tension and compression limits the reconfigurability of 1D SCNT in cyclic loading. Next, we construct a 3D lattice to overcome this limitation.

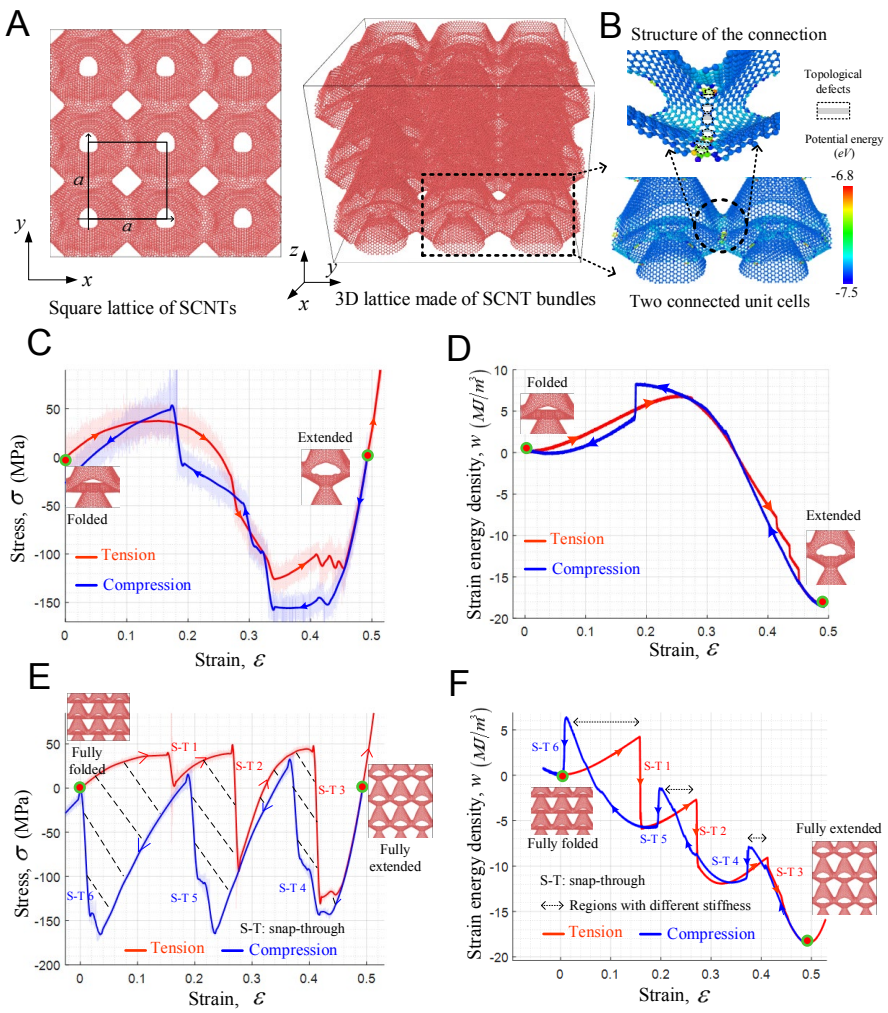

Figure 4. 4 3D design: 3D graphene nanolattice made of straw-like graphene unit cells. (A) The square lattice structure of SCNT bundles. (B) The covalently bonded connection between neighboring unit cells and topological defect distribution nearby. (C-D) The stress-strain and strain energy density-strain curves of a single unit cell under a tension-compression loop between the folded and extended states. (E-F) The stress-strain and strain energy density-strain curves of a 3D graphene nanolattice with 3-by-3-by-3 unit cells under a tension-compression loop between the folded and extended states.

As shown in Figure 4. 4A, parallel 1D SCNTs are assembled into a bundle-like architecture according to a square lattice with lattice parameter, a, forming a new 3D graphene nanolattice. We chose a to be smaller than the outer diameter the SCNTs, $2R_2$ (Figure 4. 1A), so that the neighboring SCNTs are interconnected through covalent bonding. We designed the atomic structure using topological design (224). As shown in Figure 4.

4B, topological defects appear and help to accommodate the curvature transition at the connections. To investigate the deformation behavior of such 3D graphene nanolattices, we performed tension-compression cyclic loading along the vertical directions (which is the axial direction of the SCNTs) using MD. It is demonstrated that these 3D graphene nanolattices can snap forward and backward between the fully folded and extended states under cyclic loading without suffering global buckling or irreversible damage, which makes them elastically reconfigurable.

It should be noted that the number of unit cells along the axial direction can affect the deformation behavior of the 3D graphene nanolattices. In a reference case of one single unit cell under cyclic loading along the axial direction (Figure 4. 4C-D), it is observed that the mechanical responses along tension and compression paths show very limited differences. For example, in Figure 4. 4C and D, the stress-strain and strain energy density-strain curves of tension and compression tests are close to each other. Correspondingly, very limited energy can be dissipated during such a displacement-controlled loading loop. However, the energy dissipation is amplified when there is more than one unit cell along the axial direction. For instance, in Figure 4. 4E-F, a sample with 3-by-3-by-3 unit cells are tested under the same loading condition. The stress-strain history takes different paths under tension and compression. Correspondingly, a hysteresis loop appears, and the energy associated with it is dissipated after the cycle (Figure 4. 4E). Intuitively, this hysteresis behavior can be related to the snap-through instability. As shown in Figure 4. 4E-F, the snap-through events correspond to the sudden jumps in the stress-strain and strain energy-density curves. Two observations can be made here. First, the pairs of neighboring snap-through events from tension and compression paths (such as $S\text{-}T_i$ and $S\text{-}T_{(7-i)}$, where i =1,

2, 3 in Figure 4. 4E-F) happen at different strain values. Second, in the region with strain values between one pair of such snap-through events, the strain energy density curves along tension and compression paths deviate from each other (Figure 4. 4F, regions with dash line arrows), indicating that the system can be in/near configurations with different equilibrium lengths and stiffnesses. To systematically explain the relationship between the hysteresis behavior, snap-through instability and multi-stable configurations, a theoretical model is developed in the next section.

4.2.3 Theoretical model

In this section, we construct a theoretical model to explain our observation of 3D graphene nanolattice with snap-through stability and predict the collective behavior of samples with large members of unit cells.

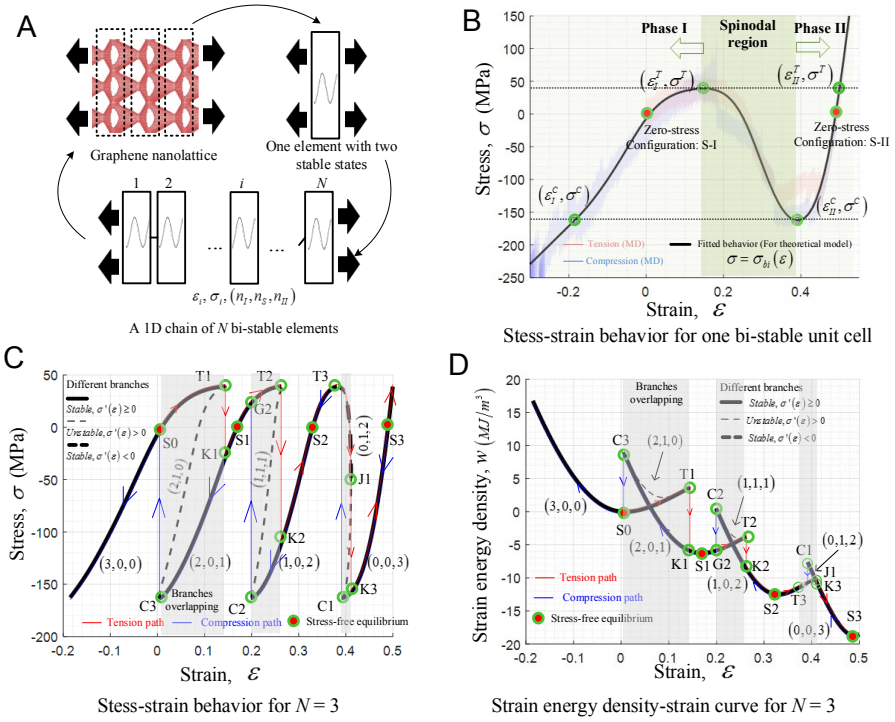

Figure 4. 5 A theorical model of 1D chain of bi-stable elements. (A) Abstracting the graphene

nanolattice with straw-like unit cell into a 1D bi-stable element chain. (B) The constitutive law of a single bi-stable element based on the MD data. (C-D) Theoretical predictions of the stable deformation branches and the paths taken under tension and compression loading on the stress-strain and strain energy density-strain curves.

Phenomenologically, our 3D graphene nanolattice can be modeled as a series of identical unit cells connected one after another along the axial direction. For each unit cell, there exits two equilibrium configurations with different lengths and stiffnesses. Correspondingly, we adopted a theoretical model of 1D chain of bi-stable elements to study the nanolattices (Figure 4. 5A). Similar models have been successfully applied to understand the rate independent hysteresis of phase transforming materials (208, 209, 228), protein deformation (229, 230) and deformation behavior of polymeric foams and carbon nanotube foams (231).

First, the deformation behavior of the unit cell of our 3D graphene nanolattice is represented by a bi-stable elastic element. Based on our MD results (Figure 4. 5C-D), the deformation of the unit cell under both tension and compression can be represented by a single stress-strain curve with no hysteresis loop (Figure 4. 5B), $\sigma = \sigma_{bi}(\varepsilon)$. Accordingly, the tangential stiffness E_t, defined as $E_t = \sigma_{bi}^{'}(\varepsilon) = \partial\sigma/\partial\varepsilon$, varies, where σ and ε are the stress and strain along the axial direction of the unit cell. Based on the sign of tangential stiffness, there exist two stable phases with $E_t > 0$, namely Phase I for $\varepsilon < \varepsilon_I^T$ and Phase II for $\varepsilon > \varepsilon_{II}^C$, separated by a spinodal region with $E_t < 0$, where ε_I^T and ε_{II}^C are strain values reaching zero tangential stiffness, i.e., $\sigma_{bi}^{'}\left(\varepsilon_I^T\right) = \sigma_{bi}^{'}\left(\varepsilon_{II}^C\right) = 0$. The presence of this spinodal region breaks down the one-to-one mapping between stress and strain for $\sigma \in \left(\sigma^C, \sigma^T\right)$ and $\varepsilon \in \left(\varepsilon_I^C, \varepsilon_{II}^T\right)$, where σ^C and σ^T are the lower and upper bounds of stress

in the spinodal region, $\sigma^C = \sigma_{bi}\left(\varepsilon_{II}^C\right)$, $\sigma^T = \sigma_{bi}\left(\varepsilon_I^T\right)$, ε_I^C and ε_{II}^T satisfy $\sigma_{bi}\left(\varepsilon_I^C\right) = \sigma^C$ in Phase I and $\sigma_{bi}\left(\varepsilon_{II}^T\right) = \sigma^T$ in Phase II (Figure 4. 5B). For our specific unit cell with $\sigma^C < 0 < \sigma^T$, there are three stress-free equilibrium configurations ($\sigma = 0$). The one in the spinodal region is not mechanically stable while those two in Phase I and II are, which makes our unit cell a bi-stable elastic element defined by a single stress-strain curve shown in Figure 4. 5B.

Second, consider the static/quasi-static deformation of 1D chain of $N \geq 2$ such bi-stable elements connected in series. In equilibrium, the strain of the chain, $\bar{\varepsilon}$, is the average over all elements and the stress of chain, $\bar{\sigma}$, is continuous through all members,

$$\begin{aligned} &\bar{\varepsilon} = \frac{1}{N}\sum_{i=1}^{N}\varepsilon_i \\ &\bar{\sigma} = \sigma_i, i = 1,2,...N \end{aligned}, \tag{4.1}$$

where ε_i and σ_i are strain and stress of the *i*-th element in the chain. Combining Eq. (4.1) with the constitutive relation of individual element,

$$\sigma_i = \sigma_{bi}\left(\varepsilon_i\right), i = 1,2,...N, \tag{4.2}$$

as depicted numerically on Figure 4. 5B, all possible equilibrium configurations can be found for given $\bar{\sigma}$ or $\bar{\varepsilon}$. However, it should be noted that the available equilibrium configurations are not necessarily stable. Here, we are only interested in those which are mechanically stable to be physically meaningful (and relevant to MD simulations at finite temperature). The multiple equilibrium configurations can be distinguished by the state of the system, i.e., the numbers of elements in the three phases, $\left(n_I, n_S, n_{II}\right)$, where n_I, n_{II} and n_S are numbers of elements in Phase I, II and spinodal region, respectively,

$n_I + n_{II} + n_S = N$. Previous studies on similar bi-stable element chains (208, 232) have shown that the equilibrium configuration is mechanically stable only if

$$n_S = 0 \ \ or \ \begin{cases} n_S = 1 \\ \dfrac{\partial \bar{\sigma}}{\partial \bar{\varepsilon}} < 0 \end{cases}, \tag{4.3}$$

i.e., the equilibrium configurations with no element in the spinodal region, $n_S = 0$, are stable; for system with only one element in the spinodal region, $n_S = 1$, it is stable only if the overall tangential stiffness is negative. Combining this criterion with the constitute law of individual bi-stable elements, Eq. (4.2) and the constraint of 1D chain, Eq. (4.1), we can obtain the stable branches of deformation behavior of the 1D chain under all possible system states, $\left(n_I, n_S, n_{II}\right)$. One example of these branches in stress-strain and strain energy density-strain curves is shown in Figure 4. 5C-D (black solid lines and thick dash lines) for a chain of $N = 3$. There exist $N+1$ branches for system states with $n_S = 0$, i.e., $\left(N-i, 0, i\right), i = 0,1,...N$ (black solid lines in Figure 4. 5C-D). They all have a convex shape in strain energy density curves (Figure 4. 5D) with one local minimal ($Si, i = 0,1,..,N$), indicating positive stiffnesses and stress-free equilibrium configurations. They are terminated at the points ($Ti, Ci, i = 1,2,..N$) where the stress reaches the critical values (σ^T or σ^C) to push one of their elements into the spinodal region. Interestingly, these termination points make the $N+1$ branches overlap with each other over finite strain intervals. These $N+1$ stable branches are connected by another N branches for system state with $n_S = 1$ (black dash lines in Figure 4. 5C-D), forming a connected path. However, for our graphene nanolattice case, except for a small portion, T3-J1 (thick dash line), most

parts of the N branches with $n_S = 1$ have a positive tangential stiffness and are therefore not stable. Consequently, the available stable branches (S0-T1, C3-S1-T2, C2-S2-T3-J1, C1-S3 in Figure 4. 5C-D) between the fully folded and extended states (S0-S3) are disconnected fragments with strain overlapping in stress-strain and strain energy density-strain curves.

It is the discontinuity and overlapping of the stable deformation branches that distinguish the collective behavior of elements in 1D chain from that of one element in monotonical and cyclic loading. First, consider a monotonically increasing tensile loading applied to the chain of three elements in a displacement-controlled way (red solid line in Figure 4. 5C-D). Starting from the fully folded state, S0, in the branch of $(N,0,0)$, the system raises the stress and accumulates energy until reaching the end of this branch, T1 with a stress of σ^T. The continuity of overall strain required by displacement-controlled loading condition can be used to find the next stable deformation branch. Accordingly, in a discrete manner, the system has to switch to the next available branch, $(N-1,0,1)$, at the point of the same strain via a snap-through event. Assuming the system is overdamped, this sudden change of system state results in a drop in the stress response and partially releases the energy of the system, which is not observed in the case of one bi-stable element. Similar changes of system state reappear at the right end of the each stable branches until the fully extended state, SN, on the last branch $(0,0,N)$ is reached, leaving behind a saw-teeth like stress-strain curve. During this loading path, the dissipated energy includes not only the work done by the external loading but also the energy difference between the stress-free configurations, SN and $S0$. Second, consider a full loop of tension-compression loading.

Like in the tension path, the saw-teeth stress-strain curve and sudden drops in system energy also appear at the left end of each stable branch ($Ci, i = 1,2,3,..$ in Fig. 5 c-d) along the compression path from SN to $S0$. Moreover, due to the overlapping of different stable deformation branches in strain intervals, the system can choose among different stable branches under tension and compression over the same strain interval. Correspondingly, over these intervals the system has different states, showing different stiffness, stress and strain energy responses (shaded regions in Figure 4. 5C-D). The separation of loading paths in tension and compression results in hysteresis loops under cyclic loading, which is also absent in the single element case. After a full loop, the system can fully recover with no energy change. The nontrivial work done by the external loading is fully dissipated through the hysteresis loops between tension and compression path in the stress-strain curve. In summary, the theoretical model predicts that the collective behavior of bi-stable elements in a 1D chain gives birth to the discontinuity and overlapping of stable deformation branches. The switching between different branches results in saw-teeth stress-strain curves under monotonical loading. The different choice of the overlapped branches yields the hysteresis loops in cyclic loading. These predictions explain the behaviors observed in MD simulations (Figure 4. 5E-F).

4.2.4 Pseudo plastic behavior in graphene nanolattices with large numbers of unit cells

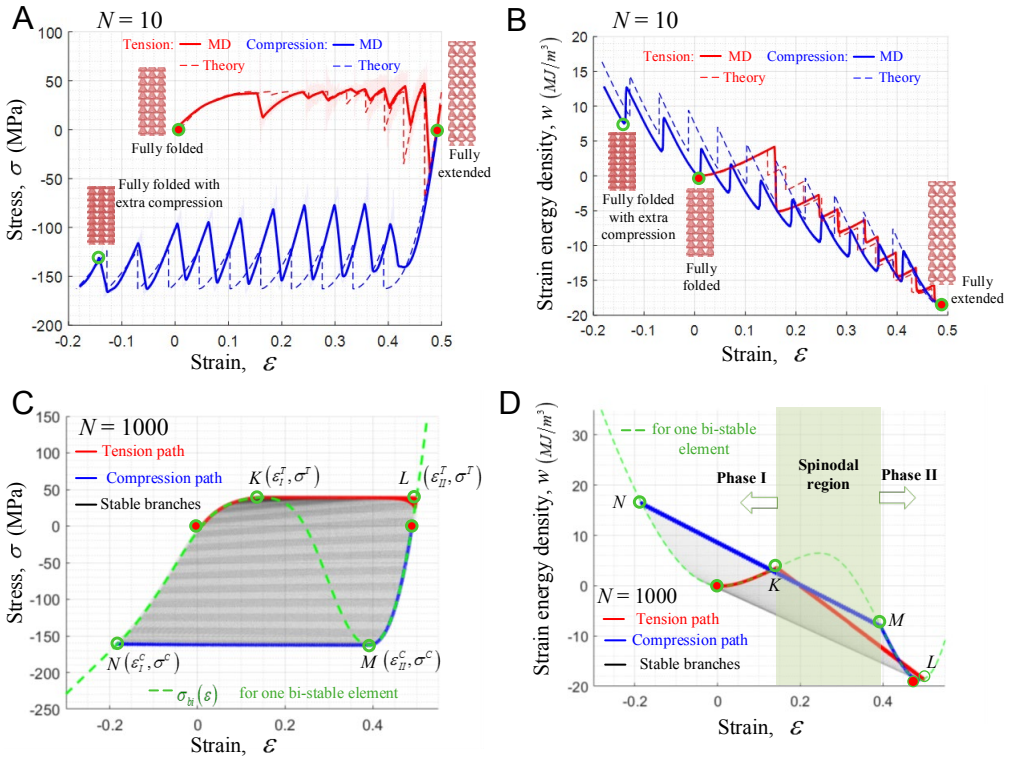

Figure 4. 6 Validating the theoretical model and predicting the collective behavior of nanolattice with a large number of unit cells. (A-B) MD results and theoretical predictions of stress-strain and strain energy density-strain curves of the nanolattice with 10 elements along the axial direction during a tension-compression loop. (C-D) Theorical prediction of the deformation of a nanolattice with 1000 elements along the axial direction and its comparison to that of a single bi-stable element.

To quantitatively validate the theoretical model, we compare its prediction to the results of MD simulations. A tension-compression test was applied to a 3D graphene nanolattice with 3-by-3-by-10 unit cells using MD. Its results are compared with the prediction of the theorical model for the case of $N = 10$. It should be noted that, there exist some important differences between the assumptions of the theoretical model and the MD simulation conditions. In the theoretical model, it is assumed that the system is over-damped, and the deformation is quasi-static (i.e., no kinetic effect has been included) and the strain rate is infinitely low. In contrast, the MD simulations are performed with a

constant temperature of 10 K and a relatively high strain rate of $10^8/s$. Under such a simulation condition with kinetic effects, the snap-through events can be triggered earlier; Several unit cells may snap at the same time; After snap-through events, the suddenly released deformation energy may excite extra fluctuations and it takes time for the associated thermal energy to be absorbed by the environment. In spite of these differences, as shown in Fig. 6 a-b, the history of stress and strain energy density during the full loading cycle still shows a reasonably good agreement between MD results and theoretical predictions. This consistency indicates that the deformation behavior of the graphene nanolattice in this study is not sensitive to strain rate and can be well captured by both MD and the theoretical model.

Comparing the MD results of cases for $N = 3$ (Figure 4. 4E-F) and $N = 10$ (Figure 4. 6A-B), it is also noted that as the number of unit cell along the axial direction increases, the amplitude of stress oscillations along tension/compression paths decreases and the area of hysteresis loop increases. Based on this observation, it becomes interesting to predict the asymptotic behavior of nanolattice samples with large numbers of unit cells and ask what is the upper bound of energy dissipation for this nanolattice design. While the full atom MD simulations may be limited by the available computational power, the efficient theoretical model developed above is suitable for this task.

By keeping increasing N (from 10 to 1000) in the theoretical model, we observed the deformation behavior converges to a pseudo plastic behavior with a finite hysteresis loop. For stress level between σ^C and σ^T, as N increases, the available stable deformation branches (grey lines in Figure 4. 6C-D for $N = 1000$) increases and become densely packed between the fully folded and extended configurations. The distance between neighboring

branches become smaller and the overlapping regions become larger. Correspondingly, the amplitude of stress drops due to switching between two neighboring branches decreases and averaged stress levels approach ending points of the stable branches, which are σ^C or σ^T. The plasticity-like behavior with flow stress σ^C and σ^T in tension and compression, respectively, is observed (K-L and M-N in Figure 4. 6C). However, there is no irreversible damage accumulated in this reconfigurable nanolattice during the process. So, we term this as a pseudo plastic behavior. The hysteresis loop formed by these two stress plateaus is finite because the branch overlapping only exists over the strain interval, $\left(\varepsilon_I^C, \varepsilon_{II}^T\right)$. The left and right boundaries of this hysteresis loop are confined by the stress-strain curves of the constituent bi-stable element between σ^C and σ^T in Phase I and II respectively (K-N and M-L in Figure 4. 6C). For stress level beyond the interval $\left(\sigma^C, \sigma^T\right)$ or strain level beyond $\left(\varepsilon_I^C, \varepsilon_{II}^T\right)$, the only stable states are $(N,0,0)$ or $(0,0,N)$ and the nanolattice behaves in the same way as one unit cell does.

It is interesting to note that the overall behavior of such a nanolattice with large number of unit cells is different from but strongly connected to that of its constituent element. It is the lattice arrangement that enables the novel deformation behavior in the assembly level, such as pseudo plasticity and hysteresis. At the same time, the deformation behavior of single bi-stable element determines the bounds of the pseudo plasticity and hysteresis loops at the lattice level. The strong connection between the behavior of the overall lattice and its constituent provides a promising way to preserve superior properties of nano-scale constituent up to the lattice scale. For example, the reversible snap-through capability of the specific straw-like unit cell studied in the present work benefits from the

ultrahigh strength, in-plane stiffness (33) and outstanding bending flexibility (16) of graphene. With a density of $453 kg/m^3$ (in the fully folded state), the graphene nanolattice made of such unit cells is predicted to have flow stresses of $39 MPa$ in tension and $-163 MPa$ in compression over a strain ranging between -0.18 and 0.49. The energy dissipation per unit mass for a full loop between the fully folded and extended states can approach $233 kJ/kg$, and this process is purely elastic with no permanent damage. Optimization of the geometry and topological defect distribution of the unit cell may further improve this specific energy dissipation density of the nanolattice. Meanwhile, for carbon steel SAE 1020 annealed, with a density of $7872 kg/m^3$ and a toughness of $128755 kJ/m^3$, the energy absorption per unit mass at failure is $16.4 kJ/kg$, which is one order of magnitude smaller than the predicted value of the graphene nanolattice studied here.

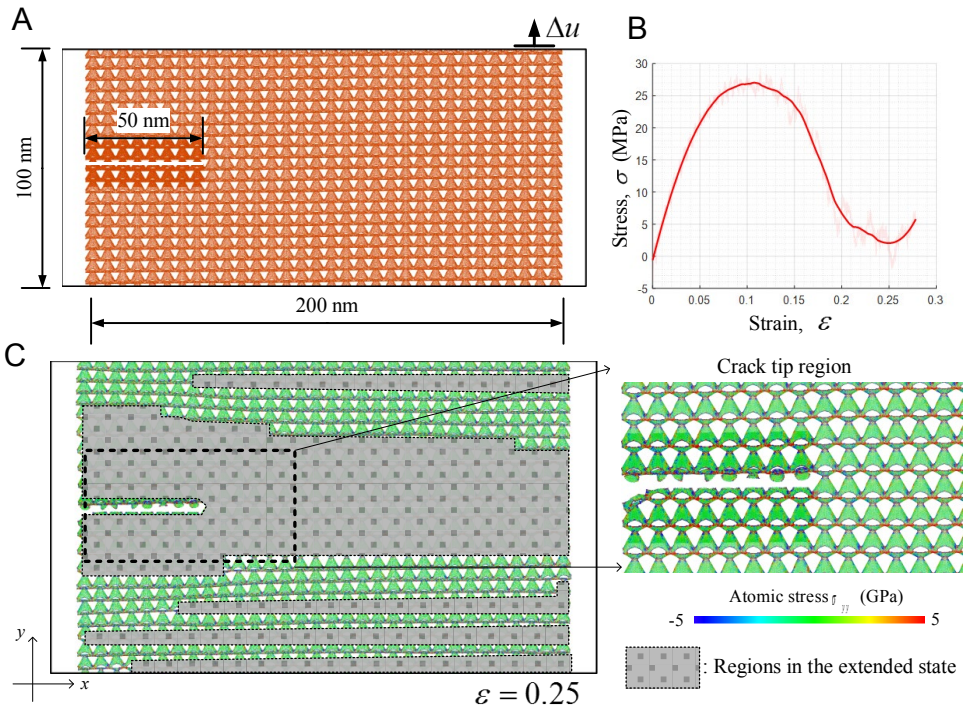

Figure 4. 7 MD simulation of a tension test of a graphene nanolattice slab with an edge crack. (A) Geometry of the graphene nanolattice. (B) The overall stress-strain curve. (C) Crack trapping due to the band-like region around the crack tip transformed into the extended state via snap-through events.

At last, we demonstrated the effect of the energy dissipation mechanisms enabled in this novel 3D graphene nanolattice on resisting crack propagation. As shown in Figure 4. 7, MD simulation of a uniaxial tension test in a slab of the graphene nanolattice 200 nm in length and 100 nm in height with a 50 nm edge crack was performed. Unlike the uniform loading in previous uniaxial tension tests, high stress concentration is expected around the crack tip region and promotes crack propagation (193). However, in the graphene nanolattice, it is observed that unit cells near the crack tip transform from the folded state into the extended one first. Correspondingly, the stress near the crack tip region is mostly released and the crack tip is trapped (Figure 4. 7C). As the transformation region expands through the lattice, the overall stress level also decreases (Figure 4. 7B) due to the reconfiguration of the nanolattice. This example demonstrates that the graphene nanolattice

with snap-through instability can tolerate crack-like flaw and behave in a ductile manner within the pseudo plastic deformation region.

4.3 Conclusions

Carbon nanolattices have demonstrated great potential in achieving outstanding mechanical performances, including a combination of high strength, low density, good flaw tolerance and extensive deformability, which are rarely seen in conventional materials. In the present study, we have investigated a type of 3D graphene nanolattice for better ductility through an efficient energy dissipation mechanism design. Specifically, snap-through instability is implemented in the unit cell level via a straw-like graphene cell. With simple lattice architectures, 1D and 3D graphene nanolattices made of such unit cells demonstrate multiple stress-free equilibrium configurations and are elastically reconfigurable. Through tension and compression tests in MD, stress plateaus with saw teeth-like oscillations and finite hysteresis loops emerge as the number of unit cells in the lattice increases. This lattice-level deformation behavior is explained by a theoretical model of a 1D bi-stable element chain. The theoretical model identifies multiple stable deformation paths available to the lattice. It is the discontinuity and overlapping of these deformation paths that give birth to a pseudo plastic deformation. Interestingly, the theoretical model predicts that the pseudo plastic behavior of the nanolattice is bounded by the deformation behavior of the unit cell. Benefiting from the outstanding property of the nanoscale unit cell, nanolattices with large numbers of such unit cells is predicted to achieve a specific energy dissipation of 233 kJ/kg during a full loading cycle without any irreversible damage, which is one order of magnitude larger than the energy absorbed by

carbon steel at failure (16.6 kJ/kg). With such efficient energy dissipation mechanisms enabled by snap-through instability, the graphene nanolattice is demonstrated to be able to trap and postpone crack propagation in MD, showing good tolerance of crack-like flaw and enhanced ductility. This novel capability may broaden the potential application of 3D graphene nanolattices in energy absorption (204) and programmable materials (233).

Chapter 5

Crack evolution in multilayered 2D materials in the presence of interlayer sliding

Chapter Summary

Multilayered 2D materials have found broad applications in fields ranging from flexible electronic devices to reinforced composites. As a stack of homogeneous or heterogeneous 2D material layers, the performance of multilayered 2D materials is influenced by not only the intralayer properties but also the interlayer interactions. Recent progresses in characterizing both the intralayer and interlayer properties in 2D materials have reviled sharp contrasts between these two, which distinguishes multilayered 2D materials from the conventional multilayered composites in macroscale. Thus, it becomes particularly interesting to ask how interlayer interactions affect the fracture process in multilayered 2D materials, given that 2D materials as individual layers often suffer from low fracture resistance. In this chapter, we study the toughening effect of the interlayer sliding on crack propagation and the competition between intralayer crack propagation and interlayer crack penetration. Using theoretical analysis and numerical simulations, we derive the energetic driving force for a propagating crack in contact with a neighboring intact layer and demonstrate an enhanced critical fracture strain due to interlayer interaction. The enhancement in the critical strain depends on the sample size, in-plane modulus of the neighboring layer as well as the interlayer shearing stress. Based on that, we further include the strength-controlled failure and provide a phase diagram to predict whether the initial

crack will propagate within the layer or penetrate the neighboring layer. Our finding presents a clear fracture mechanics model demonstrating how interlayer sliding can affect intralayer fracture and provide guidance for toughening multilayered 2D materials by choosing suitable sample size and combination of individual layers.

5.1 Introduction

Multilayered 2D materials have demonstrated novel collective properties beyond the constituent layers and are gaining broad applications in a variety of fields, ranging from functional electronic devices (77, 234-236), bio-functional coating (237) to reinforced composites (238-240). As an recent example, by stacking different 2D materials, such as graphene, hexagonal boron-nitride (hBN) and transition metal-dichalcogenides (TMDs, e.g., MoS2 and WSe2) on top of one another, van der Waals (vdW) heterostructures have emerged as a novel material system with unprecedented functions and tunability (77, 236, 241). For example, unconventional superconductivity is realized in bilayer graphene by adopting a magic twisting angle about 1.1 degree (242, 243); New designs of electronic devices based on vdW heterostructures have emerged, including tunneling transistors (244, 245), barristors (246), optoelectronic devices (10, 11, 247) and flexible electronics (248, 249). For novel structural material engineering, multilayered graphene and graphene oxide (GO) have been adopted as reinforcements in metals (e.g., Al, Cu and Ni) (172, 238, 250, 251), ceramics (e.g., alumina, silicon nitride and hydroxyapatite) (239, 252-254) and polymers (240) due to their unique 2D structure and outstanding mechanical properties. As discussed in the previous chapters, 2D materials as individual layers often suffers from a limit fracture toughness (98-100, 154). Therefore, understanding and predicting fracture behavior of these multilayered 2D materials is of great engineering significance for

realizing and optimizing the full potential of these promising applications.

At the same time, multilayered 2D materials distinguishes themselves by the unique interfaces, which makes the fracture problem in them particularly interesting for fundamental mechanics. As multilayered systems made of atomically thin layers, multilayered 2D materials possess unprecedented volume ratio of interfaces (255) comparing with the conventional laminated composites in macroscale (256, 257). For example, with an interlayer distance about 0.34 nm (255), multilayered graphene can have an interface density reaching 2.9×10^9 m^2/m^3. More importantly, there exist high contrasts between intralayer and interlayer properties in multilayered 2D materials due to the different chemical nature. For example, in vdW heterostructures, high in-plane stretching modulus arises from the strong covalent bonding within the layers (33, 258, 259) while only low interlayer sliding stress can exist due to the weak and dispersive vdW interactions between layers (260-262). Recent experimental studies have unveiled that the interlayer shear stress is about 40 KPa in bilayer graphene (260) and can reach 5 MPa in GO films (261), which are much lower compared to their in-plan strength. The unique anisotropy between intralayer and interlayer interactions and high interface density make the overall deformation behaviors of multilayered 2D materials fundamentally different from the conventional layered composites in macroscale. For example, due to the interlayer shear and sliding effect, the bending rigidity of multilayered graphene, *h*-BN and MoS_2 do not follow the classical plate theory's prediction for perfectly glued or ultralubricated multilayered plates (79). Similar interlayer sliding has also been observed in the fracture process of the multilayered 2D materials. For instance, asynchronous crack propagation in single-crystalline multilayered graphene is captured in in situ SEM experiments and the

enhancement in the measured fracture toughness is attributed to the interlayer shearing stress and interlayer slippages (263); Intralayer crack propagation and crack nucleation in the neighboring layer are observed in bilayer MoS_2 in TEM images and MD simulations (264). These observations suggest the interlayer sliding can affect the fracture process and failure modes in multilayered 2D materials and raise fundamental questions about fracture process of multilayered 2D materials in the presence of interlayer sliding.

The present chapter is aimed to investigate the effect of interlayer sliding on fracture process in multilayered 2D materials. Through an integrated theoretical and numerical approach, we will demonstrate a novel size dependence of the critical load for crack propagation different from the monolayer case and present a phase diagram for predicting intralayer crack propagation and interlayer crack penetration due to interlayer sliding.

5.2 Results

5.2.1 Model problem

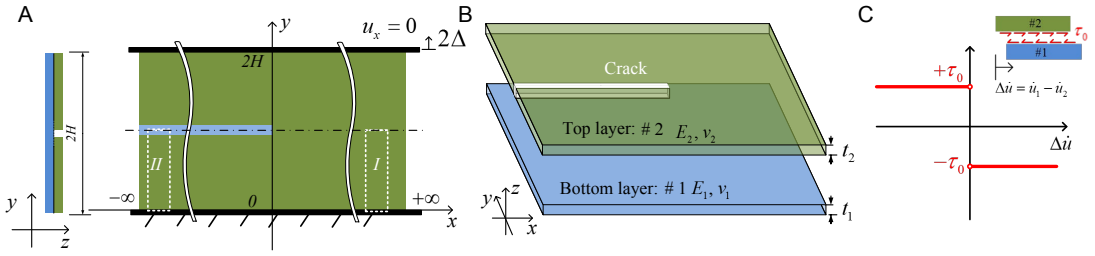

Figure 5. 1 Schematics of the model problem of a bilayer strip. (A) A bilayer infinite long strip with a height of 2*H* is loaded by prescribing the displacement at the lower and upper boundaries to propagate a semi-infinite initial crack in middle of the top layer. (B) The two layers is made of linear elastic material. (C) The interlayer interaction between the two layers shows a constant interlayer shearing stress acting against any nonzero relative sliding displacement.

In different engineering applications, the combination of the constituent layers,

intralayer and interlayer properties, geometry and loading conditions of the multilayered 2D material systems can be very complicated. Without loss of generality, the present study focuses on the shared features of these situations and studies a model problem by considering a steady state of crack propagation (144). As shown in Figure 5. 1A, a semi-infinite edge crack sits in the middle of the top layer (Green one) of an infinite long bilayer strip of a height 2*H*. The bilayer strip is loaded uniaxially by prescribing the displacement at the top and bottom boundaries as,

$$\begin{cases} u_x = 0 \\ u_y = 2\Delta \end{cases} \text{for } y = 2H, \quad \begin{cases} u_x = 0 \\ u_y = 0 \end{cases} \text{for } y = 0. \tag{5.1}$$

The two layers are made of two linear elastic brittle materials with Young's modulus E_i, Poisson's ratio ν_i and fracture energy G_{ci} and have a thickness of t_i, where i = 1 and 2 for the bottom and top layers respectively. The initial crack only cuts through the top layer leaving the bottom layer intact (Figure 5. 1B). The two layers are in contact with each other and we assume there exists a constant interlayer shear stress, τ_0, acting against the interlayer sliding between the two layers (Figure 5. 1C). It should be noted that this simplified interlayer sliding law captures the strength of the interlayer lateral interaction (260) while remaining insensitive to the detailed physical origin, such as registry dependent vdW interactions between crystalline surfaces (265, 266) or repeatedly bond breaking and forming in GO films (267). Similar assumptions have also been adopted and validated in the previous studies like bulge tests of multilayered 2D materials (260). With such a set of minimal assumptions, we aim at estimating the critical loading for the initial crack to propagate steadily in the presence of interlayer sliding.

5.2.2 Steady state analysis of the crack tip driving force

While the displacement field near the crack tip is hard to solve given the nonlinear interlayer sliding law, it remains relatively easy to obtain the deformation of in the regions far ahead of or far behind the crack tip (e.g., Region I and II in Figure 5. 1A). As the lateral distance to the crack tip goes far beyond the characteristic length of the geometry (i.e., the height *H*), the deformation field is expected to be affected little by the crack. Thus, Region I can be approximated as being under uniaxial tension without any interlayer sliding and the vertical displacement satisfies (Figure 5. 2C),

$$\begin{cases} k_1 \dfrac{d^2 u_1}{dy^2} = 0 \\ k_2 \dfrac{d^2 u_2}{dy^2} = 0 \end{cases} \text{for } y \in [0, H], \text{ with boundary conditions } \begin{cases} u_1(0) = u_2(0) = 0 \\ u_1(H) = u_2(H) = \Delta \end{cases} \tag{5.2}$$

where u_i is the vertical displacement, $k_i = \dfrac{E_i t_i}{1-\nu_i^2}$ is the 2D in-plane stiffness with i = 1 and 2 for the bottom and top layers respectively. In Region II, an interlayer sliding zone, $y \in [A, H]$ (Figure 5. 2D) forms from the initial crack surface and grows as the external load increases. The displacement satisfies

$$\begin{cases} k_1 \dfrac{d^2 u_1}{dy^2} - \tau_0 = 0 \\ k_2 \dfrac{d^2 u_2}{dy^2} + \tau_0 = 0 \end{cases} \text{for } y \in [A, H], \begin{cases} k_1 \dfrac{d^2 u_1}{dy^2} = 0 \\ k_2 \dfrac{d^2 u_2}{dy^2} = 0 \end{cases} \text{for } y \in [0, A]$$

$$\text{with boundary conditions } \begin{cases} u_1(0) = u_2(0) = 0 \\ u_1(H) = \Delta \\ k_2 \left.\dfrac{du_2}{dy}\right|_{y=H} = 0 \end{cases}, \tag{5.3}$$

where A and $(H-A)$ is the length of the sticky zone and the sliding zone in the low half. There also exists a critical loading displacement, Δ_{FS}, with which the sliding zone will

occupy the whole height of the sample (i.e., $A = 0$). And for $\Delta > \Delta_{FS}$, the sliding zone no longer expands and the displacement field in Region II satisfies (Figure 5. 2E),

$$\begin{cases} k_1 \dfrac{d^2 u_1}{dy^2} - \tau_0 = 0 \\ k_2 \dfrac{d^2 u_2}{dy^2} + \tau_0 = 0 \end{cases} \text{ for } y \in [0, H], \text{ with boundary conditions } \begin{cases} u_1(0) = u_2(0) = 0 \\ u_1(H) = \Delta \\ k_2 \dfrac{du_2}{dy}\Big|_{y=H} = 0 \end{cases} . \tag{5.4}$$

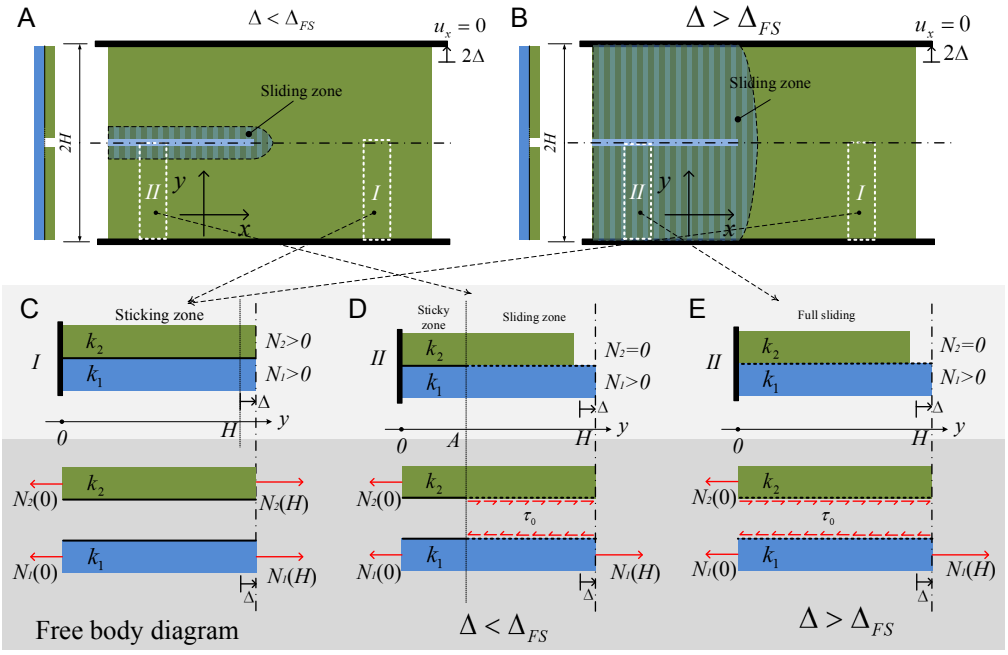

Figure 5. 2 Solving the displacment field in the regions far ahead of and far behind the crack tip. (A) Under a relatively small load, a finite sliding zone forms form the crack surfaces behind the crack tip and occupies part of the strip height. (B) Under a relatively large load, the sliding zone behind the crack tip grows to occupy the whole height of the strip and remains saturated even as the external load keeps incrasing. (C) free body diagram (FBD) of Regin I far ahead of the crack tip. (D) FBD of Regin II far behind the crack tip under partial sliding. (E) FBD of Regin II far behind the crack tip under full sliding.

By solving Equations (5.2), (5.3) and (5.4), we obtain displacement fields for Region I and II as the following. In Region I,

$$u_1^I = u_2^I = \Delta \frac{y}{H} \tag{5.5}$$

In Region II, for $0 < \Delta < \Delta_{FS}$,

$$u_1^{II}(y) = \begin{cases} \dfrac{\tau_0}{k_2}(H-A)\,y, & y \in [0, A] \\ \dfrac{1}{2}\dfrac{\tau_0}{k_1}\left(y^2 + A^2\right) - \dfrac{\tau_0}{k_1} A y + \dfrac{\tau_0}{k_2}(H-A)\,y, & y \in [A, H] \end{cases} \tag{5.6}$$

$$u_2^{II}(y) = \begin{cases} \dfrac{\tau_0}{k_2}(H-A)\,y, & y \in [0, A] \\ -\dfrac{1}{2}\dfrac{\tau_0}{k_2}\left(y^2 + A^2\right) + \dfrac{\tau_0}{k_1} H y, & y \in [A, H] \end{cases} \tag{5.7}$$

where the normalized sliding zone size is

$$1 - \frac{A}{H} = \frac{k_1}{k_2}\left(\sqrt{1 + 2\frac{k_2}{k_1}\frac{k_2}{\tau_0 H}\frac{\Delta}{H}} - 1\right) \in (0,1) \tag{5.8}$$

For the case with a saturated sliding zone, i.e., $\Delta > \Delta_{FS}$, the displacement fields in Region II read

$$u_1^{II}(y) = \Delta \frac{y}{H} - \frac{1}{2}\frac{\tau_0}{k_1}(H-y)\,y, \quad y \in (0, H), \tag{5.9}$$

$$u_2^{II}(y) = \frac{1}{2}\frac{\tau_0}{k_2}(2H-y)\,y, \quad y \in (0, H). \tag{5.10}$$

And the normalized critical load for a fully developed sliding zone is

$$\frac{\Delta_{FS}}{H} = \frac{1}{2}\left(\frac{1}{k_1} + \frac{2}{k_2}\right) H \tau_0. \tag{5.11}$$

For this infinite strip system under a fixed displacement loading, the translational invariance suggests that crack propagation over a length δa is equivalent to moving a domain, $\delta a \times 2H$, of materials from the area far ahead of the crack tip to that far behind the

crack tip (i.e., from Region I to Region II). The released strain energy associated with this process/exchange is dissipated by propagating the crack and creating the sliding zone. Thus, the energetic driving force, *2D*, for crack propagation can be calculated using the following

$$D = \left(w_I - w_{II}\right) - D_{sliding} \tag{5.12}$$

where D is the half driving force at the crack tip, w_I and w_{II} are the strain energy in Region I and II with unit width, and $D_{sliding}$ is the energy dissipation due to the sliding in Region II of unit width,

$$w_I = \int_0^H \frac{1}{2} k_1 \left(\frac{du_1^I}{dy}\right)^2 + \frac{1}{2} k_2 \left(\frac{du_2^I}{dy}\right)^2 dy\,, \tag{5.13}$$

$$w_{II} = \int_0^H \frac{1}{2} k_1 \left(\frac{du_1^{II}}{dy}\right)^2 + \frac{1}{2} k_2 \left(\frac{du_2^{II}}{dy}\right)^2 dy\,, \tag{5.14}$$

$$D_{sliding} = \int_0^H \tau_0 \left(u_1^{II} - u_2^{II}\right) dy\,. \tag{5.15}$$

Thus, combining the displacement solutions for Region I and II with Equation. (5.12), we can estimate the half driving force at the crack tip as the following,

$$D = \begin{cases} D_{PS} = \dfrac{1}{24}\dfrac{H_0^3 \tau_0^2}{k_2} h^3 \left[\alpha^2 (1+\alpha)\left(\sqrt{1+2\dfrac{e}{\alpha h}} - 1\right)^3 \left(3\sqrt{1+2\dfrac{e}{\alpha h}} + 1\right)\right], & for\ PS:\ \dfrac{e}{h} \in \left[0, 1+\dfrac{1}{2\alpha}\right] \\ D_{FS} = \dfrac{1}{24}\dfrac{H_0^3 \tau_0^2}{k_2} h^3 \left[12\left(\dfrac{e}{h}\right)^2 - 12\dfrac{e}{h} + 4 + \dfrac{1}{\alpha}\right], & for\ FS:\ \dfrac{e}{h} \in \left[1+\dfrac{1}{2\alpha}, +\infty\right] \end{cases} \tag{5.16}$$

where D_{PS} and D_{FS} are the half driving forces of partial sliding and full sliding cases respectively, H_0 is a reference half height which can be an arbitrary positive constant at this moment and will be chosen later to simplify the expression, $h = H/H_0$ is the normalized sample half height, $\alpha = k_1/k_2$ is the normalized 2D modulus of the bottom layer, $e = \dfrac{\overline{\varepsilon}}{H_0 \tau_0 / k_2}$

is the normalized averaged loading strain, $\bar{\varepsilon} = \Delta / H$ is the averaged loading strain applied to the strip, PS and FS are short for partial sliding and full sliding respectively. As a special case, at the minimal load that leads to a full sliding, i.e., $\frac{e}{h} = 1 + \frac{1}{2\alpha}$, the half driving force can be simplified as,

$$D = \frac{1}{24} \frac{H_0^3 \tau_0^2}{k_2} h^3 \left[\left(1 + \frac{1}{\alpha} \right) \left(\frac{3}{\alpha} + 4 \right) \right]. \tag{5.17}$$

As a limiting case, when the modulus of the protective bottom layer approaches to zero, i.e., $\alpha \to 0$, the half driving force can be simplified into

$$\lim_{\alpha \to 0} D = \frac{1}{2} k_2 \left(\frac{\Delta}{H} \right)^2 H = D^{\mathrm{Ref}} \tag{5.18}$$

where agrees with the monolayer case, D^{Ref}. At the other limit of a sufficiently stiff bottom layer, i.e., $\alpha \to \infty$, the half driving force also can be written explicitly as

$$\lim_{\alpha \to +\infty} D = \begin{cases} \frac{1}{24} \frac{H_0^3 \tau_0^2}{k_2} h^3 \left[4 \left(\frac{e}{h} \right)^3 \right], & for\ PS: \ \frac{e}{h} \in \left[0, 1 + \frac{1}{2\alpha} \right] \\ \frac{1}{24} \frac{H_0^3 \tau_0^2}{k_2} h^3 \left[12 \left(\frac{e}{h} \right)^2 - 12 \frac{e}{h} + 4 \right], & for\ FS: \ \frac{e}{h} \in \left[1 + \frac{1}{2\alpha}, +\infty \right] \end{cases}. \tag{5.19}$$

5.2.3 Size dependence of the critical load for crack propagation

For the brittle individual layers, according to Griffith criterion (268), the crack starts to propagate once the critical driving force is reached as

$$D = D_c, \tag{5.20}$$

where the critical driving force is $2D_c = G_{c2} t_2$ for the top layer. Theoretically, by combining Equations (5.20) and (5.16), we can obtain the critical load for the crack to propagate within the top layer. However, to clearly identify the effects of strip height and material properties, here we first introduce some characteristic length of material properties.

Consider a special half height of the strip H_0^F, with which the crack starts to propagate when the full sliding in Region II just happens. Using Equations (5.20) and (5.17), we find

$$H_0^F = f(\alpha)\tilde{H}_0^F \tag{5.21}$$

where

$$f(\alpha) = \left[\frac{14\alpha^2}{(\alpha+1)(4\alpha+3)}\right]^{\frac{1}{3}}, \alpha \in (0,+\infty) \tag{5.22}$$

$$\tilde{H}_0^F = \left(D_c \frac{12k_2}{7\tau_0^2}\right)^{1/3}. \tag{5.23}$$

It should be noted that H_0^F and $\tilde{H}_0^F$ are characteristic length determined only by the material properties of the bilayer system. With these intrinsic lengths, we can normalize the half driving force at the crack tip in Equation (5.16) as,

$$\frac{D}{\frac{1}{24}\frac{\left(\tilde{H}_0^F\right)^3\tau_0^2}{k_2}} = \begin{cases} \tilde{h}^3\left[\alpha^2(1+\alpha)\left(\sqrt{1+\frac{2}{\alpha}\frac{\tilde{e}}{\tilde{h}}}-1\right)^3\left(3\sqrt{1+\frac{2}{\alpha}\frac{\tilde{e}}{\tilde{h}}}+1\right)\right], & PS: \tilde{h} > f(\alpha) \\ \tilde{h}^3\left[12\left(\frac{\tilde{e}}{\tilde{h}}\right)^2 - 12\frac{\tilde{e}}{\tilde{h}} + 4 + \frac{1}{\alpha}\right], & FS: 0 < \tilde{h} < f(\alpha) \end{cases} \tag{5.24}$$

where $\tilde{h} = H/\tilde{H}_0^F = h \cdot f(\alpha)$ and $\tilde{e} = \frac{\overline{\varepsilon}}{\tilde{H}_0^F \tau_0/k_2} = e \cdot f(\alpha)$ are the updated normalized strip half height and normalized averaged loading strain. Similarly, using Equation (5.23), the fracture criterion in Equation (5.20) can be rewritten as

$$\frac{D}{\frac{1}{24}\frac{\left(\tilde{H}_0^F\right)^3\tau_0^2}{k_2}} = 14. \tag{5.25}$$

Combining Equations (5.24) and (5.25), we obtain the critical load, Δ_c for crack propagation in terms of the normalized averaged loading strain, $\tilde{e}_c = \frac{\overline{\varepsilon}_c}{\tilde{H}_0^F \tau_0/k_2}$ (where

$\bar{\varepsilon}_c = \frac{\Delta_c}{H}$ is the critical averaged loading strain), as the positive real valued solution to the following algebra equations,

$$\begin{aligned} &\frac{14}{\tilde{h}^3\alpha^2(1+\alpha)} = \left(\sqrt{1+\frac{2}{\alpha}\frac{\tilde{e}_c}{\tilde{h}}}-1\right)^3\left(3\sqrt{1+\frac{2}{\alpha}\frac{\tilde{e}_c}{\tilde{h}}}+1\right), \quad for\ PS: \tilde{h} > f(\alpha) \\ &12\left(\frac{\tilde{e}_c}{\tilde{h}}\right)^2 - 12\left(\frac{\tilde{e}_c}{\tilde{h}}\right) - \left(\frac{14}{\tilde{h}^3} - 4 - \frac{1}{\alpha}\right) = 0, \qquad for\ FS: 0 < \tilde{h} < f(\alpha) \end{aligned} \quad . \tag{5.26}$$

Immediately, it can be noted that explicit solutions exist for some limiting cases. For example, (1) letting the 2D modulus of the bottom layer approach zero, we get

$$\tilde{e}_c \to \tilde{e}_c^{Mono} = \sqrt{\frac{7}{6}}\frac{1}{\sqrt{\tilde{h}}} \quad for\ \alpha \to 0\,, \tag{5.27}$$

which recovers the exact result of the monolayer case, $\tilde{e}_c^{Mono}$, and the critical loading strain is proportional to the inverse square root of the characteristic dimension of the strip (i.e. the height) and approaches to zero in large samples, agreeing with Griffith's prediction. (2) In the other end, if the bottom layer is much stiffer than the crack layers, i.e., $\alpha \to +\infty$, we get

$$\tilde{e}_c \to \begin{cases} \left(\frac{7}{2}\right)^{1/3}, & PS: \tilde{h} > \left[\frac{7}{2}\right]^{1/3} \\ \frac{1}{2}\tilde{h}\left(1+\frac{1}{3}\sqrt{\frac{42}{\tilde{h}^3}-3}\right), & FS: 0 < \tilde{h} < \left[\frac{7}{2}\right]^{1/3} \end{cases} \tag{5.28}$$

It should be noted that the critical strain remains constant instead of decreasing towards zero when the height of the strip is sufficiently large. The difference between these two limiting cases indicates the presence of the bottom layer and interlayer sliding can affect the critical load for crack propagation.

To demonstrate the effect of the interlayer sliding, we first consider a special case in which the bottom layer has the same 2D modulus as the top cracked layer, i.e., $\alpha = 1$. The

critical normalized averaged loading strain for crack propagation in the top layer in Equation (5.26) can be simplified as

$$\tilde{e}_c = \begin{cases} \frac{1}{2}\tilde{h} + \sqrt{\frac{7}{6}\frac{1}{\tilde{h}} - \frac{1}{6}\tilde{h}^2}, & 0 < \tilde{h} < 1 \\ \text{real solution of } 7 = \left(\sqrt{\tilde{h}^2 + 2\tilde{h}\tilde{e}_c} - h\right)^3 \left(3\sqrt{1 + 2\frac{\tilde{e}_c}{\tilde{h}}} + 1\right), & \tilde{h} > 1 \end{cases} . \tag{5.29}$$

As shown in Figure 5. 3A, due the presence of the interlayer sliding, the critical loading strain for crack propagation (blue line) is increased compared with the monolayer case without the bottom layer (orange line). By analyzing the change in the crack tip driving force in Equation (5.12), this enhancement can be attributed to two factors. First, due the presence of the bottom layer and the interlayer sliding, the strain energy in the top layer cannot be fully released after forming the crack, i.e., $w_{II} > 0$; Second, the creation of the sliding zone during fracture process dissipates the stored strain energy, i.e., $D_{sliding} > 0$. Therefore, it's important to consider the deformation and energy dissipation associated with the sliding zone at the critical moment, which obviously depends on the size of the system. Specifically, for a strip with a half-height smaller than $\tilde{H}_0^F$, i.e., $\tilde{h} < 1$, before the crack reaches the critical moment to propagate, a sliding zone covering the full height of the strip has been developed behind the crack tip (Figure 5. 3B and C). Once a full sliding zone in Region II forms, the stored strain energy in Region II is saturated and no long increases with the applied load according to Equations (5.10) and (5.14) while the interlayer sliding can still dissipate more energy as the relative displacement increases (Figure 5. 3C) until the critical driving force is reached. Thus, the critical load is enhanced while still showing a decreasing trend with the height of the strip compared with the monolayer case. As a limiting case, when the trip height approaches towards zero, (i.e.,

$H << \tilde{H}_0^F$), the effect of the bottom layer is diminished and the monolayer result in Equation (5.27) is automatically recovered. For a strip with a half-height larger than $\tilde{H}_0^F$, the effect of the interlayer sliding becomes more significant as the trend of the critical load with increasing strip height deviates from that of the monolayer case as shown in Figure 5. 3A. In such large strips, the crack tends to propagate earlier with a smaller critical load. Thus, the interlayer shearing over the strip height is large enough to sustain most of the deformation even after the crack cuts through the top layer and the formed sliding zone only occupies a portion of the strip height. As the strip height keeps increasing, instead of decaying into zero, the critical loading approaches to a constant level determined by material properties as

$$\lim_{H\to\infty} \overline{\varepsilon}_c = \left(\frac{7}{4}\right)^{\frac{1}{3}} \frac{\tilde{H}_0^F \tau_0}{k_2} \text{ for } \alpha = 1 . \tag{5.30}$$

The positive lower bound of the critical loading strain for crack propagation indicates a strength-like criterion for the failure of the cracked top layer, which is fundamentally different from the inverse square root decaying trend in a Griffith prediction. Combining the results above, it is predicted that in the presence of the bottom layer and interlayer sliding, the critical loading strain for crack propagation in the top layer follows a transition from a Griffith-like criterion to a strength-like criterion as the strip height increases crossing a material-dependent characteristic length.

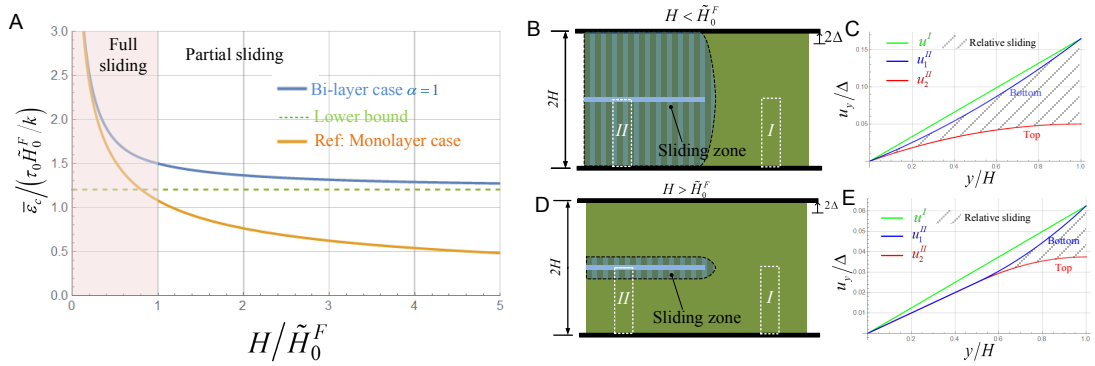

Figure 5. 3 Size dependence of the critical strain for crack propagation in the top layer in the presence of interlayer sliding. (A) Normalized critical averaged loading strain for crack propagation in the top layer with different strip half-height. (B) In a strip with a height smaller than $\tilde{H}_0^F$, crack propagates after a full sliding zone is developed. (C) Example displacement field in Region I and II after full sliding happens. (D) In a strip with a height larger than $\tilde{H}_0^F$, crack propagates when only a partial sliding zone is developed. (E) Example displacement field in Region I and II when only a partial sliding zone is formed.

In order to validate the prediction from our theoretical analysis above, finite element method (FEM) combining cohesive elements (269) and interlayer layer friction have been performed using the commercial software ABAQUS (Dassault Systemes Simulia Corp., Providence, RI) to calculate the critical strain for crack propagation. As shown in Figure 5. 4A, a finite bilayer system is built with an elastic material. An initial edge crack lies in the middle of the top layer while the bottom layer remains intact. Cohesive elements with a triangular force-separation law (Figure 5. 4B) are embedded along the path of the initial crack in the top layer to simulate brittle fracture propagation. The top and bottom layers are in contact with each other and the friction stress follows a nearly perfect plastic law with a constant flow stress (Figure 5. 4C). The strip is loaded by prescribing the displacement at the boundaries as the theoretical model discussed in the previous sections. And the failure of the first cohesive element is monitored and taken as the critical moment

for crack propagation.

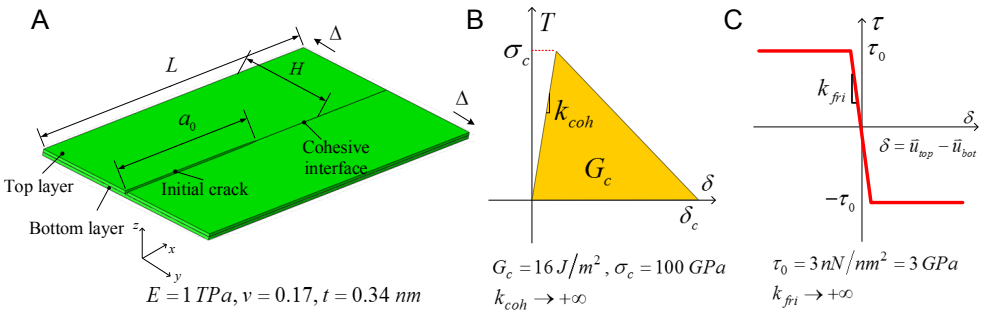

Figure 5. 4 Schematics of the numerical model. (A) The finite element model of a bilayer system with an edge crack in the top layer, cohesive element and interlayer friction included. (B) Force-separation law for the cohesive element. (C) Interlayer friction model.

Representative examples of the interlayer shear stress and in-plane stress distributions of the top and bottom layers at the critical moment are shown in Figure 5. 5A-H. The numerical solutions agree well with the theoretical prediction of the deformation filed and the interlayer sliding (Equations (2.1.5-10)) in the regions far away from the crack tip for the cases of partial sliding (Figure 5. 5A-D) as well as full sliding (Figure 5. 5E-H). And the critical loading strain show good agreement with the theoretical analysis shown in Figure 5. 5I. Since the simulations also capture the crack propagation process, this agreement in Figure 5. 5I indicates our steady state analysis of the crack tip driving force is validated for predicting crack propagation.

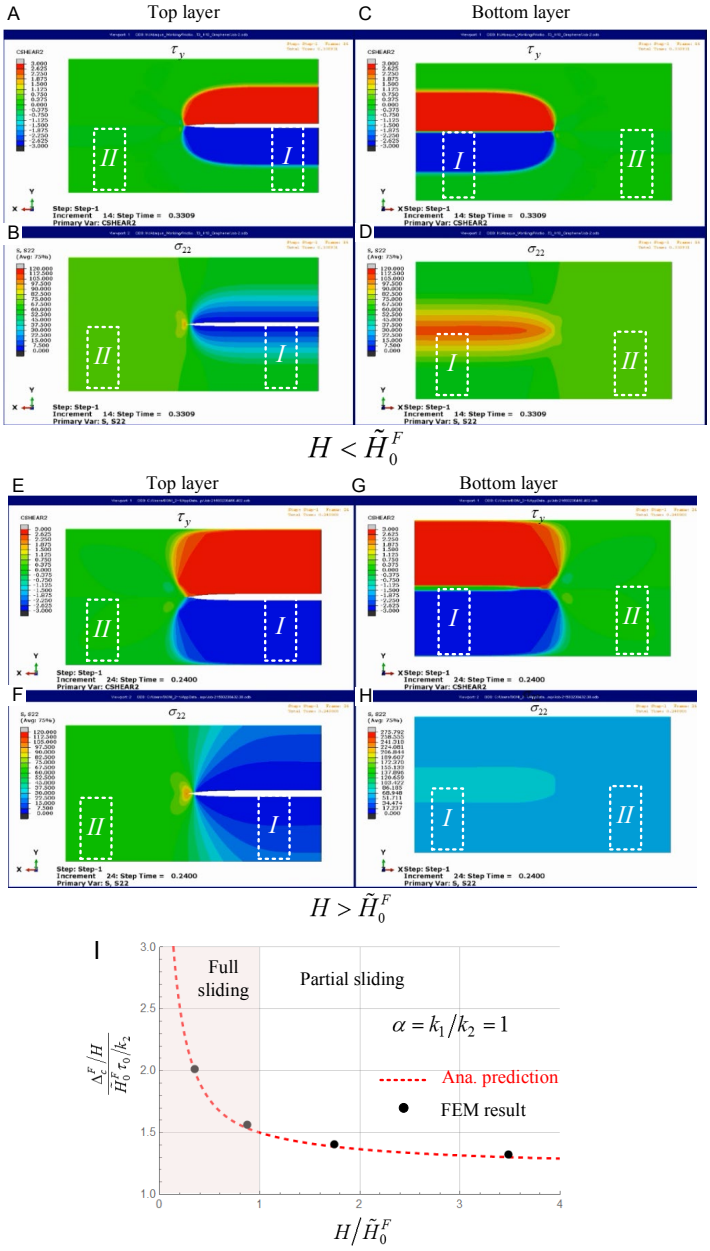

Figure 5. 5 Validating the theoretical model via numerical simulations. (A-D) Numerical solutions of a sample with $H > \tilde{H}_0^F$ at the critical moment, including vertical component of the interlayer shearing force on the top layer (A) and bottom layer (C), in-plane stress σ_{22} in the top layer (B) and the bottom layer (D). (E-H) Numerical solutions of a sample with $H < \tilde{H}_0^F$ at the critical moment, including vertical component of the interlayer shearing force on the top layer (E) and bottom layer (G), in-plane stress σ_{22} in the top layer (F) and the bottom layer (H). (I) Comparing the theoretical prediction of the critical strain for crack propagation in the top layer with the numerical simulations.

5.2.4 Combined effect of the sample height, the modulus of the bottom layer and the interlayer shearing stress

Similar size dependence of the critical loading strain for crack propagation also exists for cases with bottom layers of different 2D moduli. As shown in Figure 5. 6A, the transition from Griffith-like criterion to strength-like criterion is observed for cases with soft ($\alpha < 1$) and stiff ($\alpha > 1$) bottom layers. Correspondingly, the resistance of the top layer to crack propagation is enhanced. Here, we measure this toughening effect using the increase of the critical loading strain for crack propagation compared with that of the monolayer case, i.e., $\bar{\varepsilon}_c - \bar{\varepsilon}_c^{Mono}$, and its normalized form, $\tilde{e}_c - \tilde{e}_c^{Mono}$, for the case of varying strip height and bottom layer modulus is shown in Figure 5. 6B, where

$$\bar{\varepsilon}_c = \tilde{e}_c\left(\frac{\tilde{H}_0^F \tau_0}{k_2}\right), \quad \bar{\varepsilon}_c^{Mono} = \tilde{e}_c^{Mono}\left(\frac{\tilde{H}_0^F \tau_0}{k_2}\right). \tag{5.31}$$

Compared with the monolayer case, the toughening effect due to the interlayer sliding becomes greater as the height of the bilayer strip grows or the stiffness of the bottom layer increases and limits exist along these two increasing directions. For a bilayer strip with a fixed height, the lower and upper bounds of the critical strain are set by the soft and hard limiting cases of the bottom layer as shown in Equation (5.27) and (5.28). For the bilayer strip with an ever-increasing height much larger than $H_0^F(\alpha)$, the lower bound of the critical normalized loading strain is

$$\tilde{e}_c = \left(\frac{7}{2}\frac{\alpha}{\alpha+1}\right)^{1/3} \text{ as } \tilde{h} \to +\infty, \tag{5.32}$$

which also increases with the relative modulus of the bottom layer. Thus, the enhancement

of the normalized critical strain occupies the following interval as shown in Figure 5. 6B,

$$0 < \tilde{e}_c - \tilde{e}_c^{Mono} < \left(\frac{7}{2}\right)^{\frac{1}{3}}, \tag{5.33}$$

and it monotonically increases with the strip height and the 2D modulus of the bottom layer.

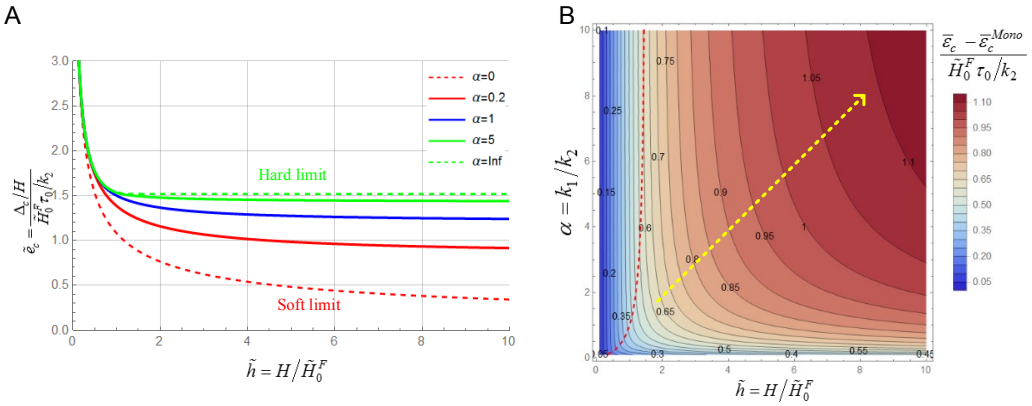

Figure 5. 6 (A) The normalized critical strain for crack propagation in cases with different strip height and 2D modulus of the bottom layer. (B) The normalized increase of the critical strain in cases with different strip height and 2D modulus of the bottom layer.

It should be noted that, in the limiting case of an infinite high strip, the size of the sliding zone in region behind the crack approaches to a finite constant. Plugging the solution of Equation (5.26) into Equation (5.8) and taking the height limit, we obtain the size of the sliding zone as,

$$(H - A) \to \tilde{H}_0^F \left(\frac{7}{2}\frac{\alpha}{\alpha+1}\right)^{1/3} \text{ as } H \to +\infty. \tag{5.34}$$

And displacement solutions under the limit of infinite height indicates there will be no change in displacement outside the sliding zone during fracture. So, all the driving force at the crack tip comes from the energy release within in the finite sliding zone, which makes it a local event no longer depends on the sample size. This localized source of energy driving force leaves the possibility for multiple parallel cracks to propagate in the top layer

independently as long as their half-distance are much large than the size of the sliding zone in Equation (5.34).

The toughening effect of the interlayer sliding also depends on the amplitude of the interlayer shearing interaction, which is represented through the interlayer shearing stress, τ_0, in our model. Combining Equations (5.23) and (5.31), we obtain

$$\bar{\varepsilon}_c - \bar{\varepsilon}_c^{Mono} = \left(\frac{12}{7} D_c \frac{\tau_0}{k_2^{\,2}}\right)^{1/3} \cdot \left(\tilde{e}_c - \tilde{e}_c^{Mono}\right). \tag{5.35}$$

Keeping other material properties and strip height fixed, increasing τ_0 leads to a decrease of $\tilde{H}_0^F$ and an increase in $\tilde{e}_c - \tilde{e}_c^{Mono}$ (i.e., moving right horizontally in Figure 5. 6B). Since the prefactor in Equation (5.35) also increases with τ_0, we conclude the enhancement in the critical loading strain monotonically increases with τ_0. Thus, increasing the interlayer sliding stress can also postpone the crack propagation. It should be noted that the enhancement in the critical strain due to stronger interlayer sliding stress is not bounded, unlike those resulted from increasing strip height or the 2D modulus of the bottom layer. Consider a limiting case in which the interlayer shearing is extremely strong, i.e., $\tau_0 \to \infty$. The crack in the top layer will not release any deformation or stored strain energy in Region II because the interlayer interaction is sufficiently strong to transfer the load across the crack via the bottom layer. With no energy release, the crack propagation becomes impossible, which agrees with the prediction of Equation (5.35) as

$$\bar{\varepsilon}_c - \bar{\varepsilon}_c^{Mono} \to +\infty \; for \; \tau_0 \to +\infty \,. \tag{5.36}$$

In summary, compared with the monolayer case, our model predicts the introduction of the bottom layer and the interlayer sliding can enhance the top layer's resistance to crack propagation by increasing the critical loading strain. For such a bilayer strip with fixed

material properties, the critical strain for crack propagation follows a transition from Griffith-like criterion to a strength-like criterion as the strip height increases. The enhancement in the critical strain compared with the monolayer case grows with the height of the strip; For a bilayer strip with a given height, choosing a stiffer bottom layer or having stronger interlayer shearing stress can postpone the crack propagation.

5.2.5 Competition between intralayer crack propagation and interlayer crack penetration

The previous section predicts that by increasing the interlayer shearing stress to infinite, the crack propagation in the top layer can be postponed indefinitely. However, this ideal prediction can rarely be realized in reality because other failure mode can kick in and lead to the failure of the system. For example, as the initial crack in the top layer is properly contained by interlayer sliding, high stress concentration is built up in the bottom layer beneath the crack. As the material reaches its strength, it is expected that crack can nucleate in the region and lead to a vertical crack penetration into the bottom layer. In this section we consider the competition between fracture-controlled intralayer crack propagation and strength-controlled interlayer crack penetration by comparing the critical load for both failure modes.

To simplify the derivation, here we focus on bilayer systems made of the same 2D material layers, i.e., $\alpha = 1$. As indicated by the numerical solutions (such as Figure 5. 5D and H), the highest stress in the bilayer system occurs in the region of the bottom layer right beneath the initial crack. Using the displacement solution in Region II, we can compare the maximal 2D stress with the strength of the bottom layer, $N_c = \sigma_{c1} t_1$, and obtain

the critical strain for crack penetration, where σ_{c1} is the strength in terms of 3D stress. After some tedious but straightforward deviation, we obtain the critical strain for strength-controlled crack penetration, $\bar{\varepsilon}_c^S$ in its normalized form $\tilde{e}_c^S$ as,

$$\tilde{e}_c^S = \begin{cases} 2 - \dfrac{1}{2}\dfrac{H}{\tilde{H}_0^S}, & FS: H < \tilde{H}_0^S \\ 1 + \dfrac{1}{2}\dfrac{1}{H/\tilde{H}_0^S}, & PS: H > \tilde{H}_0^S \end{cases}, \tag{5.37}$$

where

$$\tilde{e}_c^S = \frac{\bar{\varepsilon}_c^S}{N_c/2k_2}, \tag{5.38}$$

$$\tilde{H}_0^S = \frac{N_c}{2\tau_0}. \tag{5.39}$$

$\tilde{H}_0^S$ is another special half-height of the bilayer strip with which the strength criterion is reached just when a full sliding zone forms in Region II and depends on material properties. As shown in Figure 5. 7, the normalized critical loading strain for crack penetration decreases as the height of the strip increases and the two limiting cases have explicit results. For the strip with vanishing height, i.e., $H/\tilde{H}_0^S \to 0$, the effect of the top layer on the bottom layer disappears and the critical strain of a uniform strip under uniaxial tension is recovered,

$$\lim_{H\to 0} \bar{\varepsilon}_c^S = \frac{N_c}{k_2} = \frac{N_c}{k_1} \quad for \ \ \alpha = 1. \tag{5.40}$$

For a strip with a sufficient large height, i.e., $H/\tilde{H}_0^S \to +\infty$, almost no sliding happens. The maximal 2D stress in the bottom layer is doubled compared with elsewhere since the crack in the top layer reduced the effective thickness by a half, i.e.,

$$\lim_{H\to \infty} \bar{\varepsilon}_c^S = \frac{N_c}{2k_2} = \frac{N_c}{2k_1} \ for\ \alpha = 1. \tag{5.41}$$

Combining these two limits and the monotonical decreasing trend, we find the normalized

critical strain for crack penetration falls into a finite interval,

$$\tilde{e}_c^S \in (1,2). \tag{5.42}$$

Keeping other material properties and the strip height fixed, the critical strain also decreases as the interlayer shearing stress, τ_0, increases. According to Equation (5.39), increasing τ_0 leads to a smaller $\tilde{H}_0^S$, which is equivalent to move left in Figure 5. 7. Correspondingly, the critical strain for crack penetration also decreases. In summary, increasing the strip height or strengthening the interlayer shearing tends to make crack penetration easier with a smaller critical load strain.

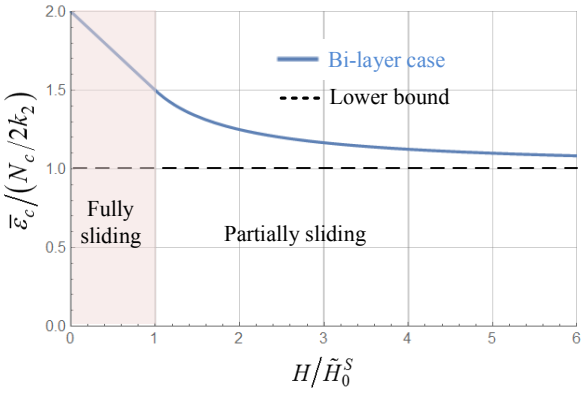

Figure 5. 7 The normalized critical strain for the strength-controlled crack penetration into the bottom layer in cases with different strip height.

Now, we compare the critical strain values for the fracture-controlled crack propagation within the top layer (marked with a superscript, F) and the strength-controlled crack penetration into the bottom layer (marked with a superscript, S) and pick the lower one as the real critical strain for the failure of the bilayer system, $\bar{\varepsilon}_c$,

$$\bar{\varepsilon}_c = \min\left[\bar{\varepsilon}_c^F, \bar{\varepsilon}_c^S\right]. \tag{5.43}$$

As shown in Figure 5. 8A and B, we take the strength failure related properties and characteristic length as the reference and plot the ratio, $\bar{\varepsilon}_c^F/\bar{\varepsilon}_c^S$ (Figure 5. 8A) and the

normalized critical strain, $\bar{\varepsilon}_c$ (Figure 5. 8B), for bilayer system with varying fracture energy and strip height. The vertical axis, $\lambda = \tilde{H}_0^F / \tilde{H}_0^S$, represents the relative fracture resistance with respective to the material strength,

$$\lambda = \frac{\tilde{H}_0^F}{\tilde{H}_0^S} = \left[\frac{(G_{c2}t_2)k_2\tau_0}{(\sigma_{c1}t_1)^3} \frac{48}{7} \right]^{\frac{1}{3}} \propto \frac{(G_{c2}t_2)^{\frac{1}{3}}(k_2\tau_0)^{\frac{1}{3}}}{(\sigma_{c1}t_1)}, \tag{5.44}$$

and the horizontal axis, $H/\tilde{H}_0^S$, represent the normalized strip half-height. For the bilayer strips with a fixed height, an increasing fracture energy or fracture toughness can transfer the failure mode from intralayer crack propagation into interlayer crack penetration. The transition boundary, i.e., $\bar{\varepsilon}_c^F / \bar{\varepsilon}_c^S = 1$ (red line in Figure 5. 8A and dash line in Figure 5. 8B) represent a sufficient toughness, over which the failure mode will always remain strength-controlled crack penetration. This sufficient toughness varies with the strip height and has a maximal. The size-dependency of the failure mode and the critical load varies with the material properties. There exist two special values of the relative fracture toughness,

$$\lambda_l = (4/7)^{1/3}, \lambda_u = \frac{2}{7}\left[4\left(10+\sqrt{2}\right)\right]^{1/3}. \tag{5.45}$$

For $\tilde{H}_0^F / \tilde{H}_0^S < \lambda_l$, as the strip height increases from zero to infinite, the failure mode starts with interlayer crack penetration then quickly transfer into and remain as intralayer crack propagation. For $\tilde{H}_0^F / \tilde{H}_0^S > \lambda_u$, the only failure mode is interlayer crack penetration and the critical strain decreases as the strip height increases. For $\tilde{H}_0^F / \tilde{H}_0^S \in (\lambda_l, \lambda_u)$, more complicated transition can happen. As the strip height varies from zero to infinite, the failure mode starts with interlayer crack penetration, change into intralayer crack propagation and then transfer back to interlayer crack penetration as shown in Figure 5. 8A and B. The effect of interlayer shearing stress, τ_0, on the failure mode can be indirectly

obtained from the discussions on the two failure modes individually. Keeping other conditions unchanged, an increased interlayer shearing stress tends to decrease the critical strain for crack penetration and increase the toughening effect for crack propagation. Thus, a strong interlayer sliding stress tends to promote interlayer crack penetration and the quantitative effect can also be extracted by combining Figure 5. 8B and the normalization parameters.

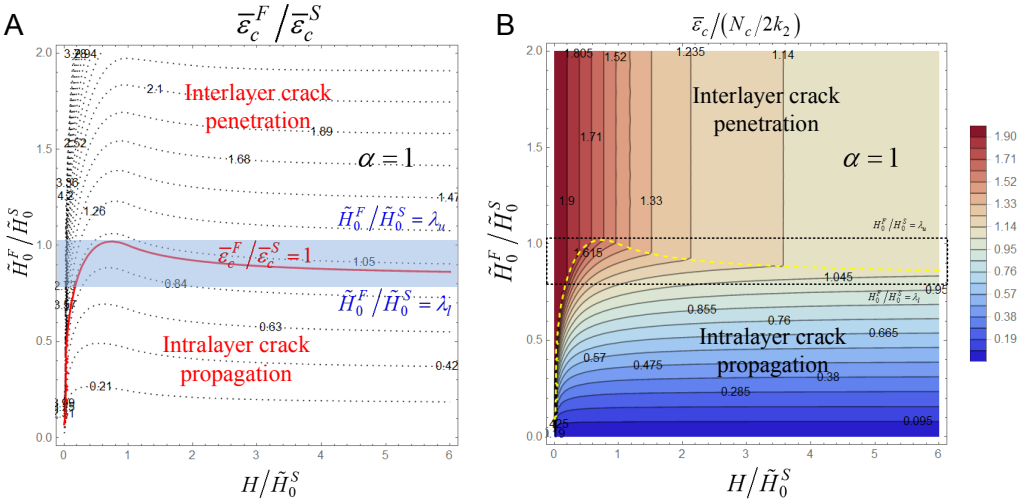

Figure 5. 8 A the phase diagram of the failure mode under different material properties and sample size. (A) The ratio between the critical strain for intralayer crack propagation and interlayer crack penetration. (B) The normalized critical strain for the failure of the bilayer system as the consequence of the competition between the two failure modes.

5.3 Conclusions

Multilayered 2D materials have found broad applications in fields ranging from flexible electronic device design to reinforced composite engineering. With the extremely high density of interfaces and the sharp contrast between intralayer and interlayer properties, the interlayer interaction is expected to a play critical role in determining the collective properties of multilayered 2D materials. Given the low fracture toughness of the

individual 2D material layers, it becomes particularly interesting to ask how interlayer interaction affects the fracture process in multilayered 2D materials and how to take advantage of it to toughen 2D material layers. In this chapter, by adopting a simplified bilayer strip model, we have investigated the toughening effect of the interlayer sliding on crack propagation and demonstrated a competition between intralayer crack propagation and interlayer crack penetration. Specifically, by using theoretical analysis and numerical simulations, we conducted a steady state analysis of the driving force for a propagating crack within the top layer. The results demonstrated that the presence of the neighboring bottom layer and the interlayer interaction can drain the driving force at the crack tip by partially releasing elastic energy after fracture and dissipating the released energy via interlayer sliding. Correspondingly, the critical strain for crack propagation in the top layer is enhanced compared with the monolayer case and show a transition from Griffith-like criterion to strength-like criterion as the strip height increases. The enhancement in the critical strain increases if the strip height grows, or the 2D modulus of the bottom layer rises, or the interlayer shearing stress is strengthened. As the intralayer crack propagation can be postponed due to the interlayer interaction, the system can still fail due to reaching the strength of the material. We have included this possibility by considering the failure of the bottom layer during bridging the initial crack in the top layer and demonstrated a competition between intralayer crack propagation and interlayer crack penetration under different strip height, fracture toughness, material strength and interlayer sliding stress. The dependence of the failure mode on these material properties and sample size are analyzed in detail and the quantitative prediction of the critical strain is also provided. Our study and findings present a clear fracture mechanics model demonstrating how interlayer sliding can

affect intralayer fracture and provide rational guidance for toughening multilayered 2D materials by adopting suitable combination of the sample size, in-plane elasticity and interlayer shearing.

Chapter 6

Conclusions and Perspectives

6.1 Concluding remarks

In this thesis, we aim to advance the fundamental understanding of fracture in 2D materials, especially on how crack interacts with topological defects, out-of-plane curvature, 3D geometry and architecture as well as interlayer sliding, and to take advantage of these novel couplings to propose effective toughening mechanisms and design guidance for tough 2D material engineering in various forms, including monolayer sheets, hybrids with nanotubes, 3D nanolattices and multilayered systems. Below we summarize the scientific findings and their engineering implications for the main chapters.

In Chapter 2, we have demonstrated a mechanism-guided topological design strategy for graphene toughening. Based on the strong coupling between out-of-plane geometry and deformation behaviors in graphene, we have introduced networks of out-of-plane curvatures into graphene by designing the distribution of topological defects and demonstrated various toughening mechanisms, including crack tip blunting, crack trapping, fracture mode transition, ligament bridging, crack deflection, void formation, interfacial failure, daughter crack initiation and coalescence can be transplanted into graphene. The forward relation from topological design to toughening effect is studies and categorized by comparing the vein-patterned graphene with various types of networks of wavy phases. And the possibility of inverse design of wavy phases to reproduce the targeted deformation and fracture behaviors is demonstrated via a nacre-like graphene example. These findings

advance the fundamental understanding about the connections between simple topological patterns and effective toughening mechanisms in atomically thin materials and are expected to provide rational guidance for tough 2D material design and engineering.

In Chapter 3, by joining force with the experimental experts, we have performed quantitative *in situ* mechanical tests and numerical simulations on rebar graphene and determined the toughening mechanisms of the embedded carbon nanotubes (CNTs). By reconstructing full-atom models of rebar graphene and conducting fracture tests with MD simulations, we demonstrated the detailed interactions between crack and CNTs in rebar graphene, including CNT bridging/pulling out, graphene bridging, daughter crack initiation, crack coarsening and crack deflection, and identified their dependence on the geometry and distribution of the CNTs. Collectively, these toughening mechanisms contribute to the experimental measured enhancement in fracture toughness and explain experimental observation of a non-smooth crack path. The unveiled toughening mechanisms in rebar graphene may be applied to design and engineer other tough 2D material systems as hybrids of 2D planar sheets and 1D nanotubes, like rebar hexagonal-boron nitride (h-BN) and even rebar transition metal dichalcogenides (TMDs).

In Chapter 4, we have demonstrated a novel design of using a reversible snap-through instability to engineer energy dissipation in 3D graphene nanolattices. Inspired by the shell structure of flexible straws, we have constructed its graphene counterpart via topological design and demonstrated its associated snap-through instability through MD simulations. 1D straw-like CNT and 3D graphene nanolattices are constructed from a unit cell. These graphene nanolattices possess multiple stable states and are elastically reconfigurable. A theoretical model of 1D bi-stable element chain is adopted to understand the collective

deformation behavior of the nanolattice. Reversible pseudo plastic behavior with a finite hysteresis loop is predicted and further validated via MD. Enhanced by these novel energy dissipation mechanisms, the 3D graphene nanolattice shows good tolerance of crack-like flaw. This study provides a novel mechanism for 3D carbon nanolattice to dissipate energy with no accumulative damage and improve resistance to fracture, broadening the promising application of 3D carbon in energy absorption and programmable materials.

In Chapter 5, we have studied the toughening effect of the interlayer sliding on crack propagation and the competition between intralayer crack propagation and interlayer crack penetration. Using theoretical analysis and numerical simulations, we derived the energetic driving force for a propagating crack in contact with a neighboring intact layer and demonstrated an enhanced critical fracture strain due to interlayer interaction. The enhancement in the critical strain depends on the sample size, in-plane modulus of the neighboring layer as well as the interlayer shearing stress. Based on that, we further included the strength-controlled failure and provided a phase diagram to predict whether the initial crack will propagate within the layer or penetrate the neighboring layer. Our findings present a clear fracture mechanics model demonstrating how interlayer sliding can affect intralayer fracture and provide practical guidance for toughening multilayered 2D materials by choosing suitable size and combination of individual layers.

6.2 Outlook of future research

As a family of materials with extreme dimensionality, high interface density and various assembly forms, 2D materials have demonstrated novel deformation behaviors and physical properties which are rarely observed in conventional bulk materials. These aspects

in turn bring new challenges and opportunities for mechanics and engineering. This thesis aims at responding to this trend by focusing on the mechanics of fracture and toughening in 2D materials of various forms. However, limited by the scope of this thesis, only a few selected topics are included while many newly emerged interactions, such as asymmetric edge states in binary 2D materials (259, 270), effects of piezoelectricity (271, 272) and flexoelectricity (76, 273, 274) and so on, are left for future studies. Within the covered topics, including topological defects, out-of-plane curvature, 3D geometry and architecture and interlayer sliding, the discussions in this thesis provided answers to some questions while stimulating more for further exploration. Some of them are listed below.

In Chapter 2, it has been discovered that the network wavy phases with out-of-plane curvatures and topological defects can act as barrier to a propagating crack. And the enhanced fracture energy is demonstrated through a series of topologically designed graphene samples. From a fundamental science point of view, it will be interesting to know how much enhancement comes from the curvature and how much from the topological defects if we want to apply similar toughening design for general shell structures in different scales. Since the out-of-plane curvature and topological defects go hand by hand in graphene, a continuum model capable of predicting crack propagation on a curved thin shell, such as phase field fracture model (275), may be helpful to isolate the effect of curvature on crack propagation. At the same time, from an engineering point of view, the design with an optimized fracture toughness can be of great practical interests. However, how we can efficiently find the optimized design remains a challenging but important inverse problem and worth further study. Even through phase field crystal modeling and full-atom simulations are good for capturing the detailed mechanisms, they can be very

costly if large numbers of samples have to be constructed and tested. Not to mention the relation between fracture toughness and graphene geometry and topology can be very nonlinear. Given these challenges, machine learning models (276) and genetic algorithm (277) might be potential candidates for addressing this inverse deign challenge.

In Chapter 3, the combination of experimental measurements and numerical simulations has successfully unveiled the toughening mechanisms in rebar graphene. Given the rapid development of experimental capabilities, can we use these findings to design and fabricate rebar graphene with even better properties? For example, can we achieve plastic-like deformation in rebar graphene by controlling the geometry and distribution of the embedded CNTs? If so, how can we optimize these designs for a balanced strength and toughness (278)?

In Chapter 4, a 3D graphene nanolattice consisting of bi-stable unit cells is achieved by designing the geometry and architecture of the graphene surfaces. Collectively, the nanolattice deforms in a pseudo-plastic way while the flow stress and flow strain are determined by the unit cell. To tune the overall mechanical properties, a good understanding about the relation between geometry and snap-through instability in a unit cell is needed. A phase diagram over the parametric space of the geometry to predict the monostability/bistability of the unit cell can be very useful and worth further development. In the architecture level, it will be interesting to introduce some defected unit cells into the 3D lattice and study how these local defects affect their neighboring unit cells during snap-through and influence the overall deformation behavior.

In Chapter 5, the interaction between crack propagation and interlayer sliding is studied within a bilayer system with a one-parameter interlayer sliding model.

Improvements can be made by adopting a more sophisticated interlayer interaction model. For example, for vdW heterogeneous structures, models considering atomic registry (265, 279) can be very helpful in capturing the interaction between intralayer fracture and interlayer dislocations. Also, the potentially universal crack tip field in the presence of interlayer sliding is still missing and worth further study.

Bibliography

1. Novoselov KS, Geim AK, Morozov S, Jiang D, Zhang Y, Dubonos Sa, et al. Electric field effect in atomically thin carbon films. science. 2004;306(5696):666-9.
2. Zhang Y, Tan Y-W, Stormer HL, Kim P. Experimental observation of the quantum Hall effect and Berry's phase in graphene. Nature. 2005;438(7065):201-4.
3. Novoselov K, Geim AK, Morozov S, Jiang D, Katsnelson M, Grigorieva I, et al. Two-dimensional gas of massless Dirac fermions in graphene. nature. 2005;438(7065):197-200.
4. Berger C, Song Z, Li T, Li X, Ogbazghi AY, Feng R, et al. Ultrathin epitaxial graphite: 2D electron gas properties and a route toward graphene-based nanoelectronics. The Journal of Physical Chemistry B. 2004;108(52):19912-6.
5. Barone V, Peralta JE. Magnetic boron nitride nanoribbons with tunable electronic properties. Nano letters. 2008;8(8):2210-4.
6. Nagashima A, Tejima N, Gamou Y, Kawai T, Oshima C. Electronic structure of monolayer hexagonal boron nitride physisorbed on metal surfaces. Physical review letters. 1995;75(21):3918.
7. Mak KF, Lee C, Hone J, Shan J, Heinz TF. Atomically thin MoS 2: a new direct-gap semiconductor. Physical Review Letters. 2010;105(13):136805.
8. Radisavljevic B, Radenovic A, Brivio J, Giacometti V, Kis A. Single-layer MoS2 transistors. Nature nanotechnology. 2011;6(3):147-50.
9. Watanabe K, Taniguchi T, Kanda H. Direct-bandgap properties and evidence for ultraviolet lasing of hexagonal boron nitride single crystal. Nature materials. 2004;3(6):404-9.
10. Bonaccorso F, Sun Z, Hasan T, Ferrari A. Graphene photonics and optoelectronics. Nature photonics. 2010;4(9):611.
11. Wang QH, Kalantar-Zadeh K, Kis A, Coleman JN, Strano MS. Electronics and optoelectronics of two-dimensional transition metal dichalcogenides. Nature nanotechnology. 2012;7(11):699-712.
12. Balandin AA, Ghosh S, Bao W, Calizo I, Teweldebrhan D, Miao F, et al. Superior thermal conductivity of single-layer graphene. Nano letters. 2008;8(3):902-7.
13. Cooper RC, Lee C, Marianetti CA, Wei X, Hone J, Kysar JW. Nonlinear elastic behavior of two-dimensional molybdenum disulfide. Physical Review B. 2013;87(3):035423.

14. Li C, Bando Y, Zhi C, Huang Y, Golberg D. Thickness-dependent bending modulus of hexagonal boron nitride nanosheets. Nanotechnology. 2009;20(38):385707.

15. Lu Q, Arroyo M, Huang R. Elastic bending modulus of monolayer graphene. Journal of Physics D: Applied Physics. 2009;42(10):102002.

16. Wei Y, Wang B, Wu J, Yang R, Dunn ML. Bending rigidity and Gaussian bending stiffness of single-layered graphene. Nano letters. 2012;13(1):26-30.

17. Ganatra R, Zhang Q. Few-layer MoS2: a promising layered semiconductor. ACS nano. 2014;8(5):4074-99.

18. Dean C, Young A, Wang L, Meric I, Lee G-H, Watanabe K, et al. Graphene based heterostructures. Solid State Communications. 2012;152(15):1275-82.

19. Zeng Z, Yin Z, Huang X, Li H, He Q, Lu G, et al. Single-Layer Semiconducting Nanosheets: High-Yield Preparation and Device Fabrication. Angewandte Chemie International Edition. 2011;50(47):11093-7.

20. Kim KS, Zhao Y, Jang H, Lee SY, Kim JM, Kim KS, et al. Large-scale pattern growth of graphene films for stretchable transparent electrodes. nature. 2009;457(7230):706-10.

21. Ghatak S, Pal AN, Ghosh A. Nature of electronic states in atomically thin MoS2 field-effect transistors. Acs Nano. 2011;5(10):7707-12.

22. Wang X, Ouyang Y, Li X, Wang H, Guo J, Dai H. Room-temperature all-semiconducting sub-10-nm graphene nanoribbon field-effect transistors. Physical review letters. 2008;100(20):206803.

23. Lee G-H, Yu Y-J, Cui X, Petrone N, Lee C-H, Choi MS, et al. Flexible and transparent MoS2 field-effect transistors on hexagonal boron nitride-graphene heterostructures. ACS nano. 2013;7(9):7931-6.

24. Bunch JS, Van Der Zande AM, Verbridge SS, Frank IW, Tanenbaum DM, Parpia JM, et al. Electromechanical resonators from graphene sheets. Science. 2007;315(5811):490-3.

25. Lee J, Wang Z, He K, Shan J, Feng PX-L. High frequency MoS2 nanomechanical resonators. ACS nano. 2013;7(7):6086-91.

26. Eichler A, Moser J, Chaste J, Zdrojek M, Wilson-Rae I, Bachtold A. Nonlinear damping in mechanical resonators made from carbon nanotubes and graphene. Nature nanotechnology. 2011;6(6):339-42.

27. Prasai D, Tuberquia JC, Harl RR, Jennings GK, Bolotin KI. Graphene: corrosion-inhibiting coating. ACS nano. 2012;6(2):1102-8.
28. Cohen-Tanugi D, Grossman JC. Water desalination across nanoporous graphene. Nano letters. 2012;12(7):3602-8.
29. Heiranian M, Farimani AB, Aluru NR. Water desalination with a single-layer MoS2 nanopore. Nature communications. 2015;6.
30. Surwade SP, Smirnov SN, Vlassiouk IV, Unocic RR, Veith GM, Dai S, et al. Water desalination using nanoporous single-layer graphene. Nature nanotechnology. 2015;10(5):459-64.
31. Liu Y, Dong X, Chen P. Biological and chemical sensors based on graphene materials. Chemical Society Reviews. 2012;41(6):2283-307.
32. Liu F, Ming P, Li J. Ab initio calculation of ideal strength and phonon instability of graphene under tension. Physical Review B. 2007;76(6):064120.
33. Lee C, Wei X, Kysar JW, Hone J. Measurement of the elastic properties and intrinsic strength of monolayer graphene. science. 2008;321(5887):385-8.
34. Peng Q, Ji W, De S. Mechanical properties of the hexagonal boron nitride monolayer: Ab initio study. Computational Materials Science. 2012;56:11-7.
35. Castellanos-Gomez A, Poot M, Steele GA, van der Zant HS, Agraït N, Rubio-Bollinger G. Elastic properties of freely suspended MoS2 nanosheets. Advanced Materials. 2012;24(6):772-5.
36. Bertolazzi S, Brivio J, Kis A. Stretching and breaking of ultrathin MoS2. ACS nano. 2011;5(12):9703-9.
37. Zhang P, Ma L, Fan F, Zeng Z, Peng C, Loya PE, et al. Fracture toughness of graphene. Nature communications. 2014;5.
38. Eda G, Fanchini G, Chhowalla M. Large-area ultrathin films of reduced graphene oxide as a transparent and flexible electronic material. Nature nanotechnology. 2008;3(5):270-4.
39. Reina A, Jia X, Ho J, Nezich D, Son H, Bulovic V, et al. Large area, few-layer graphene films on arbitrary substrates by chemical vapor deposition. Nano letters. 2008;9(1):30-5.
40. Li X, Cai W, An J, Kim S, Nah J, Yang D, et al. Large-area synthesis of high-quality and uniform graphene films on copper foils. Science. 2009;324(5932):1312-4.
41. Kim KK, Hsu A, Jia X, Kim SM, Shi Y, Hofmann M, et al. Synthesis of monolayer hexagonal boron nitride on Cu foil using chemical vapor deposition. Nano letters.

2011;12(1):161-6.

42. Tay RY, Griep MH, Mallick G, Tsang SH, Singh RS, Tumlin T, et al. Growth of large single-crystalline two-dimensional boron nitride hexagons on electropolished copper. Nano letters. 2014;14(2):839-46.

43. Huang PY, Ruiz-Vargas CS, Van Der Zande AM, Whitney WS, Levendorf MP, Kevek JW, et al. Grains and grain boundaries in single-layer graphene atomic patchwork quilts. Nature. 2011;469(7330):389-92.

44. Kim K, Lee Z, Regan W, Kisielowski C, Crommie M, Zettl A. Grain boundary mapping in polycrystalline graphene. ACS nano. 2011;5(3):2142-6.

45. Hwangbo Y, Lee C-K, Kim S-M, Kim J-H, Kim K-S, Jang B, et al. Fracture characteristics of monolayer CVD-graphene. Scientific reports. 2014;4.

46. Ly TH, Zhao J, Cichocka MO, Li L-J, Lee YH. Dynamical observations on the crack tip zone and stress corrosion of two-dimensional MoS 2. Nature communications. 2017;8(1):1-7.

47. Si C, Liu Z, Duan W, Liu F. First-principles calculations on the effect of doping and biaxial tensile strain on electron-phonon coupling in graphene. Physical review letters. 2013;111(19):196802.

48. Levy N, Burke S, Meaker K, Panlasigui M, Zettl A, Guinea F, et al. Strain-induced pseudo–magnetic fields greater than 300 tesla in graphene nanobubbles. Science. 2010;329(5991):544-7.

49. Zhu S, Stroscio JA, Li T. Programmable extreme pseudomagnetic fields in graphene by a uniaxial stretch. Physical review letters. 2015;115(24):245501.

50. Zhao H, Aluru N. Temperature and strain-rate dependent fracture strength of graphene. Journal of Applied Physics. 2010;108(6):064321.

51. Wei Y, Wu J, Yin H, Shi X, Yang R, Dresselhaus M. The nature of strength enhancement and weakening by pentagon–heptagon defects in graphene. Nature materials. 2012;11(9):759-63.

52. Lee G-H, Cooper RC, An SJ, Lee S, Van Der Zande A, Petrone N, et al. High-strength chemical-vapor–deposited graphene and grain boundaries. science. 2013;340(6136):1073-6.

53. Kotakoski J, Meyer JC. Mechanical properties of polycrystalline graphene based on a realistic atomistic model. Physical Review B. 2012;85(19):195447.

54. Zhang T, Li X, Gao H. Defects controlled wrinkling and topological design in graphene. Journal of the Mechanics and Physics of Solids. 2014;67:2-13.

55. Khare R, Mielke SL, Paci JT, Zhang S, Ballarini R, Schatz GC, et al. Coupled quantum mechanical/molecular mechanical modeling of the fracture of defective carbon nanotubes and graphene sheets. Physical Review B. 2007;75(7):075412.
56. Terdalkar SS, Huang S, Yuan H, Rencis JJ, Zhu T, Zhang S. Nanoscale fracture in graphene. Chemical Physics Letters. 2010;494(4-6):218-22.
57. Cohen-Tanugi D, Grossman JC. Mechanical Strength of Nanoporous Graphene as a Desalination Membrane. Nano letters. 2014;14(11):6171-8.
58. Zhang T, Li X, Kadkhodaei S, Gao H. Flaw insensitive fracture in nanocrystalline graphene. Nano letters. 2012;12(9):4605-10.
59. Kim K, Artyukhov VI, Regan W, Liu Y, Crommie M, Yakobson BI, et al. Ripping graphene: preferred directions. Nano letters. 2011;12(1):293-7.
60. Sen D, Novoselov KS, Reis PM, Buehler MJ. Tearing graphene sheets from adhesive substrates produces tapered nanoribbons. Small. 2010;6(10):1108-16.
61. Moura MJ, Marder M. Tearing of free-standing graphene. Physical Review E. 2013;88(3):032405.
62. Huang X, Yang H, van Duin AC, Hsia KJ, Zhang S. Chemomechanics control of tearing paths in graphene. Physical Review B. 2012;85(19):195453.
63. Li N-N, Sha Z-D, Pei Q-X, Zhang Y-W. Hydrogenated grain boundaries control the strength and ductility of polycrystalline graphene. The Journal of Physical Chemistry C. 2014;118(25):13769-74.
64. Omeltchenko A, Yu J, Kalia RK, Vashishta P. Crack front propagation and fracture in a graphite sheet: a molecular-dynamics study on parallel computers. Physical review letters. 1997;78(11):2148.
65. Zhao S, Xue J. Mechanical properties of hybrid graphene and hexagonal boron nitride sheets as revealed by molecular dynamic simulations. Journal of Physics D: Applied Physics. 2013;46(13):135303.
66. Blees MK, Barnard AW, Rose PA, Roberts SP, McGill KL, Huang PY, et al. Graphene kirigami. Nature. 2015;524(7564):204-7.
67. Wei Y, Wang B, Wu J, Yang R, Dunn ML. Bending rigidity and Gaussian bending stiffness of single-layered graphene. Nano letters. 2013;13(1):26-30.
68. Yazyev OV, Louie SG. Topological defects in graphene: Dislocations and grain boundaries.

Physical Review B. 2010;81(19):195420.
69. Song Z, Artyukhov VI, Wu J, Yakobson BI, Xu Z. Defect-detriment to graphene strength is concealed by local probe: the topological and geometrical effects. ACS nano. 2014;9(1):401-8.
70. Jung G, Qin Z, Buehler MJ. Molecular mechanics of polycrystalline graphene with enhanced fracture toughness. Extreme Mechanics Letters. 2015;2:52-9.
71. Zhang T, Li X, Gao H. Designing graphene structures with controlled distributions of topological defects: A case study of toughness enhancement in graphene ruga. Extreme Mechanics Letters. 2014;1:3-8.
72. Qin H, Sun Y, Liu JZ, Liu Y. Mechanical properties of wrinkled graphene generated by topological defects. Carbon. 2016;108:204-14.
73. Ito Y, Shen Y, Hojo D, Itagaki Y, Fujita T, Chen L, et al. Correlation between chemical dopants and topological defects in catalytically active nanoporous graphene. Advanced Materials. 2016;28(48):10644-51.
74. Cortijo A, Vozmediano MA. Effects of topological defects and local curvature on the electronic properties of planar graphene. Nuclear Physics B. 2007;763(3):293-308.
75. Kvashnin AG, Sorokin PB, Yakobson BI. Flexoelectricity in carbon nanostructures: nanotubes, fullerenes, and nanocones. The journal of physical chemistry letters. 2015;6(14):2740-4.
76. Kalinin SV, Meunier V. Electronic flexoelectricity in low-dimensional systems. Physical Review B. 2008;77(3):033403.
77. Geim AK, Grigorieva IV. Van der Waals heterostructures. Nature. 2013;499(7459):419-25.
78. Dai Z, Lu N, Liechti KM, Huang R. Mechanics at the interfaces of 2D materials: Challenges and opportunities. Current Opinion in Solid State and Materials Science. 2020:100837.
79. Wang G, Dai Z, Xiao J, Feng S, Weng C, Liu L, et al. Bending of multilayer van der Waals materials. Physical Review Letters. 2019;123(11):116101.
80. Pu J, Mo Y, Wan S, Wang L. Fabrication of novel graphene–fullerene hybrid lubricating films based on self-assembly for MEMS applications. Chemical Communications. 2014;50(4):469-71.
81. Liu Z-B, Xu Y-F, Zhang X-Y, Zhang X-L, Chen Y-S, Tian J-G. Porphyrin and fullerene covalently functionalized graphene hybrid materials with large nonlinear optical properties. The

Journal of Physical Chemistry B. 2009;113(29):9681-6.

82. Yu D, Dai L. Self-assembled graphene/carbon nanotube hybrid films for supercapacitors. The Journal of Physical Chemistry Letters. 2010;1(2):467-70.

83. Terse-Thakoor T, Komori K, Ramnani P, Lee I, Mulchandani A. Electrochemically functionalized seamless three-dimensional graphene-carbon nanotube hybrid for direct electron transfer of glucose oxidase and bioelectrocatalysis. Langmuir. 2015;31(47):13054-61.

84. Zhu Y, Li L, Zhang C, Casillas G, Sun Z, Yan Z, et al. A seamless three-dimensional carbon nanotube graphene hybrid material. Nature communications. 2012;3(1):1-7.

85. Kim K, Lee T, Kwon Y, Seo Y, Song J, Park JK, et al. Lanthanum-catalysed synthesis of microporous 3D graphene-like carbons in a zeolite template. Nature. 2016;535(7610):131-5.

86. Bauer J, Schroer A, Schwaiger R, Kraft O. Approaching theoretical strength in glassy carbon nanolattices. Nature materials. 2016;15(4):438-43.

87. Jeong YR, Park H, Jin SW, Hong SY, Lee SS, Ha JS. Highly stretchable and sensitive strain sensors using fragmentized graphene foam. Advanced Functional Materials. 2015;25(27):4228-36.

88. Li J, Zhao S, Zeng X, Huang W, Gong Z, Zhang G, et al. Highly stretchable and sensitive strain sensor based on facilely prepared three-dimensional graphene foam composite. ACS applied materials & interfaces. 2016;8(29):18954-61.

89. Novoselov KS, Geim AK, Morozov SV, Jiang D, Zhang Y, Dubonos SV, et al. Electric field effect in atomically thin carbon films. science. 2004;306(5696):666-9.

90. Xia F, Farmer DB, Lin Y-m, Avouris P. Graphene field-effect transistors with high on/off current ratio and large transport band gap at room temperature. Nano letters. 2010;10(2):715-8.

91. Schneider GF, Kowalczyk SW, Calado VE, Pandraud G, Zandbergen HW, Vandersypen LM, et al. DNA translocation through graphene nanopores. Nano letters. 2010;10(8):3163-7.

92. Heerema SJ, Dekker C. Graphene nanodevices for DNA sequencing. Nature nanotechnology. 2016;11(2):127-36.

93. Tian Z, Mahurin SM, Dai S, Jiang D-e. Ion-gated gas separation through porous graphene. Nano letters. 2017;17(3):1802-7.

94. Jiang D-e, Cooper VR, Dai S. Porous graphene as the ultimate membrane for gas separation. Nano letters. 2009;9(12):4019-24.

95. Homaeigohar S, Elbahri M. Graphene membranes for water desalination. NPG Asia

Materials. 2017;9(8):e427-e.
96. Si C, Sun Z, Liu F. Strain engineering of graphene: a review. Nanoscale. 2016;8(6):3207-17.
97. Sahalianov IY, Radchenko TM, Tatarenko VA, Cuniberti G, Prylutskyy YI. Straintronics in graphene: Extra large electronic band gap induced by tensile and shear strains. Journal of Applied Physics. 2019;126(5):054302.
98. Zhang P, Ma L, Fan F, Zeng Z, Peng C, Loya PE, et al. Fracture toughness of graphene. Nature communications. 2014;5(1):1-7.
99. Wei X, Xiao S, Li F, Tang D-M, Chen Q, Bando Y, et al. Comparative fracture toughness of multilayer graphenes and boronitrenes. Nano letters. 2015;15(1):689-94.
100. Jang B, Mag-isa AE, Kim J-H, Kim B, Lee H-J, Oh C-S, et al. Uniaxial fracture test of freestanding pristine graphene using in situ tensile tester under scanning electron microscope. Extreme Mechanics Letters. 2017;14:10-5.
101. Reina A, Jia X, Ho J, Nezich D, Son H, Bulovic V, et al. Large area, few-layer graphene films on arbitrary substrates by chemical vapor deposition. Nano letters. 2009;9(1):30-5.
102. Obraztsov AN. Making graphene on a large scale. Nature nanotechnology. 2009;4(4):212-3.
103. Deng B, Liu Z, Peng H. Toward mass production of CVD graphene films. Advanced Materials. 2019;31(9):1800996.
104. Garaj S, Liu S, Golovchenko JA, Branton D. Molecule-hugging graphene nanopores. Proceedings of the National Academy of Sciences. 2013;110(30):12192-6.
105. O'Hern SC, Stewart CA, Boutilier MS, Idrobo J-C, Bhaviripudi S, Das SK, et al. Selective molecular transport through intrinsic defects in a single layer of CVD graphene. ACS nano. 2012;6(11):10130-8.
106. Hwangbo Y, Lee C-K, Kim S-M, Kim J-H, Kim K-S, Jang B, et al. Fracture characteristics of monolayer CVD-graphene. Scientific reports. 2014;4:4439.
107. Elapolu MS, Tabarraei A. An Atomistic Study of the Stress Corrosion Cracking in Graphene. The Journal of Physical Chemistry A. 2020;124(35):7060-70.
108. Zhang T, Gao H. Toughening graphene with topological defects: a perspective. Journal of Applied Mechanics. 2015;82(5).
109. Zhang T, Li X, Gao H. Fracture of graphene: a review. International Journal of Fracture.

2015;196(1-2):1-31.

110. Kumar K, Van Swygenhoven H, Suresh S. Mechanical behavior of nanocrystalline metals and alloys. Acta materialia. 2003;51(19):5743-74.

111. Lu K, Lu L, Suresh S. Strengthening materials by engineering coherent internal boundaries at the nanoscale. science. 2009;324(5925):349-52.

112. Lu L, Chen X, Huang X, Lu K. Revealing the maximum strength in nanotwinned copper. Science. 2009;323(5914):607-10.

113. Li X, Wei Y, Lu L, Lu K, Gao H. Dislocation nucleation governed softening and maximum strength in nano-twinned metals. Nature. 2010;464(7290):877-80.

114. Tian Y, Xu B, Yu D, Ma Y, Wang Y, Jiang Y, et al. Ultrahard nanotwinned cubic boron nitride. Nature. 2013;493(7432):385-8.

115. Moon W-J, Ito T, Uchimura S, Saka H. Toughening of ceramics by dislocation sub-boundaries. Materials Science and Engineering: A. 2004;387:837-9.

116. Huang Q, Yu D, Xu B, Hu W, Ma Y, Wang Y, et al. Nanotwinned diamond with unprecedented hardness and stability. Nature. 2014;510(7504):250-3.

117. Kumar K, Van Swygenhoven H, Suresh S. Mechanical behavior of nanocrystalline metals and alloys1. Acta Materialia. 2003;51(19):5743-74.

118. Pan Q, Zhou H, Lu Q, Gao H, Lu L. History-independent cyclic response of nanotwinned metals. Nature. 2017;551(7679):214-7.

119. Saka H. Toughening of a brittle material by means of dislocation subboundaries. Philosophical magazine letters. 2000;80(7):461-6.

120. Meng F, Chen C, Song J. Dislocation shielding of a nanocrack in graphene: atomistic simulations and continuum modeling. The journal of physical chemistry letters. 2015;6(20):4038-42.

121. Verma A, Parashar A. The effect of STW defects on the mechanical properties and fracture toughness of pristine and hydrogenated graphene. Physical Chemistry Chemical Physics. 2017;19(24):16023-37.

122. Rajasekaran G, Parashar A. Molecular dynamics study on the mechanical response and failure behaviour of graphene: performance enhancement via 5–7–7–5 defects. RSC advances. 2016;6(31):26361-73.

123. Rajasekaran G, Parashar A. Enhancement of fracture toughness of graphene via crack

bridging with stone-thrower-wales defects. Diamond and Related Materials. 2017;74:90-9.

124. Wang S, Yang B, Yuan J, Si Y, Chen H. Large-scale molecular simulations on the mechanical response and failure behavior of a defective graphene: cases of 5–8–5 defects. Scientific reports. 2015;5(1):1-9.

125. Song J, Curtin W, Bhandakkar T, Gao H. Dislocation shielding and crack tip decohesion at the atomic scale. Acta materialia. 2010;58(18):5933-40.

126. Song Z, Artyukhov VI, Wu J, Yakobson BI, Xu Z. Defect-detriment to graphene strength is concealed by local probe: the topological and geometrical effects. ACS nano. 2015;9(1):401-8.

127. Ni B, Zhang T, Li J, Li X, Gao H. Topological design of graphene. Handbook of Graphene, Volume 2: Physics, Chemistry, and Biology. 2019:1.

128. Geng D, Wu B, Guo Y, Huang L, Xue Y, Chen J, et al. Uniform hexagonal graphene flakes and films grown on liquid copper surface. Proceedings of the National Academy of Sciences. 2012;109(21):7992-6.

129. Yu Q, Jauregui LA, Wu W, Colby R, Tian J, Su Z, et al. Control and characterization of individual grains and grain boundaries in graphene grown by chemical vapour deposition. Nature materials. 2011;10(6):443-9.

130. Chen Z, Ren W, Gao L, Liu B, Pei S, Cheng H-M. Three-dimensional flexible and conductive interconnected graphene networks grown by chemical vapour deposition. Nature materials. 2011;10(6):424-8.

131. Ito Y, Tanabe Y, Qiu HJ, Sugawara K, Heguri S, Tu NH, et al. High-quality three-dimensional nanoporous graphene. Angewandte Chemie. 2014;126(19):4922-6.

132. Min BH, Kim DW, Kim KH, Choi HO, Jang SW, Jung H-T. Bulk scale growth of CVD graphene on Ni nanowire foams for a highly dense and elastic 3D conducting electrode. Carbon. 2014;80:446-52.

133. Yang Z, Yan C, Liu J, Chabi S, Xia Y, Zhu Y. Designing 3D graphene networks via a 3D-printed Ni template. RSC Advances. 2015;5(37):29397-400.

134. Kawasumi K, Zhang Q, Segawa Y, Scott LT, Itami K. A grossly warped nanographene and the consequences of multiple odd-membered-ring defects. Nature chemistry. 2013;5(9):739-44.

135. Cheung KY, Xu X, Miao Q. Aromatic saddles containing two heptagons. Journal of the American Chemical Society. 2015;137(11):3910-4.

136. Cheung KY, Chan CK, Liu Z, Miao Q. A twisted nanographene consisting of 96 carbon

atoms. Angewandte Chemie International Edition. 2017;56(31):9003-7.
137. Robertson AW, Allen CS, Wu YA, He K, Olivier J, Neethling J, et al. Spatial control of defect creation in graphene at the nanoscale. Nature communications. 2012;3(1):1-7.
138. Warner JH, Fan Y, Robertson AW, He K, Yoon E, Lee GD. Rippling graphene at the nanoscale through dislocation addition. Nano letters. 2013;13(10):4937-44.
139. Dirks J-H, Taylor D. Veins improve fracture toughness of insect wings. PloS one. 2012;7(8):e43411.
140. Smith C, Herbert R, Wootton R, Evans K. The hind wing of the desert locust (Schistocerca gregaria Forskal). II. Mechanical properties and functioning of the membrane. Journal of Experimental Biology. 2000;203(19):2933-43.
141. Elder KR, Provatas N, Berry J, Stefanovic P, Grant M. Phase-field crystal modeling and classical density functional theory of freezing. Physical Review B. 2007;75(6):064107.
142. Li J, Ni B, Zhang T, Gao H. Phase field crystal modeling of grain boundary structures and growth in polycrystalline graphene. Journal of the Mechanics and Physics of Solids. 2018;120:36-48.
143. Evans DJ, Holian BL. The nose–hoover thermostat. The Journal of chemical physics. 1985;83(8):4069-74.
144. Anderson TL. Fracture mechanics: fundamentals and applications: CRC press; 2017.
145. Dasari A, Zhang Q-X, Yu Z-Z, Mai Y-W. Toughening polypropylene and its nanocomposites with submicrometer voids. Macromolecules. 2010;43(13):5734-9.
146. Barthelat F, Espinosa H. An experimental investigation of deformation and fracture of nacre–mother of pearl. Experimental mechanics. 2007;47(3):311-24.
147. Shao Y, Zhao H-P, Feng X-Q, Gao H. Discontinuous crack-bridging model for fracture toughness analysis of nacre. Journal of the Mechanics and Physics of Solids. 2012;60(8):1400-19.
148. Stempflé P, Pantalé O, Rousseau M, Lopez E, Bourrat X. Mechanical properties of the elemental nanocomponents of nacre structure. Materials Science and Engineering: C. 2010;30(5):715-21.
149. Gao H. Application of fracture mechanics concepts to hierarchical biomechanics of bone and bone-like materials. International Journal of Fracture. 2006;138(1-4):101.
150. Dimas LS, Bratzel GH, Eylon I, Buehler MJ. Tough composites inspired by mineralized

natural materials: computation, 3D printing, and testing. Advanced Functional Materials. 2013;23(36):4629-38.

151. Wang Z, Xiang C, Yao X, Le Floch P, Mendez J, Suo Z. Stretchable materials of high toughness and low hysteresis. Proceedings of the National Academy of Sciences. 2019;116(13):5967-72.

152. Wang N, Xia S. Cohesive fracture of elastically heterogeneous materials: an integrative modeling and experimental study. Journal of the Mechanics and Physics of Solids. 2017;98:87-105.

153. Mitchell N. Fracture in sheets draped on curved surfaces. Geometric Control of Fracture and Topological Metamaterials: Springer; 2020. p. 17-30.

154. Yang Y, Li X, Wen M, Hacopian E, Chen W, Gong Y, et al. Brittle fracture of 2D MoSe2. Advanced Materials. 2017;29(2):1604201.

155. Yan Z, Peng Z, Casillas G, Lin J, Xiang C, Zhou H, et al. Rebar graphene. ACS nano. 2014;8(5):5061-8.

156. Geim AK, Novoselov KS. The rise of graphene. Nanoscience and technology: a collection of reviews from nature journals: World Scientific; 2010. p. 11-9.

157. Zhao H, Min K, Aluru N. Size and chirality dependent elastic properties of graphene nanoribbons under uniaxial tension. Nano letters. 2009;9(8):3012-5.

158. Bolotin KI, Sikes KJ, Jiang Z, Klima M, Fudenberg G, Hone J, et al. Ultrahigh electron mobility in suspended graphene. Solid state communications. 2008;146(9-10):351-5.

159. Dean CR, Young AF, Meric I, Lee C, Wang L, Sorgenfrei S, et al. Boron nitride substrates for high-quality graphene electronics. Nature nanotechnology. 2010;5(10):722-6.

160. Gómez-Navarro C, Burghard M, Kern K. Elastic properties of chemically derived single graphene sheets. Nano letters. 2008;8(7):2045-9.

161. Balandin AA. Thermal properties of graphene and nanostructured carbon materials. Nature materials. 2011;10(8):569-81.

162. Lee C, Wei X, Li Q, Carpick R, Kysar JW, Hone J. Elastic and frictional properties of graphene. physica status solidi (b). 2009;246(11-12):2562-7.

163. Shekhawat A, Ritchie RO. Toughness and strength of nanocrystalline graphene. Nature communications. 2016;7(1):1-8.

164. Faccio R, Denis PA, Pardo H, Goyenola C, Mombrú AW. Mechanical properties of

graphene nanoribbons. Journal of Physics: Condensed Matter. 2009;21(28):285304.

165. Claussen N. Fracture toughness of Al2O3 with an unstabilized ZrO2Dispersed phase. Journal of the American Ceramic Society. 1976;59(1-2):49-51.

166. George R, Kashyap K, Rahul R, Yamdagni S. Strengthening in carbon nanotube/aluminium (CNT/Al) composites. Scripta Materialia. 2005;53(10):1159-63.

167. Cha SI, Kim KT, Arshad SN, Mo CB, Hong SH. Extraordinary strengthening effect of carbon nanotubes in metal-matrix nanocomposites processed by molecular-level mixing. Advanced Materials. 2005;17(11):1377-81.

168. Yang Y, Rigdon W, Huang X, Li X. Enhancing graphene reinforcing potential in composites by hydrogen passivation induced dispersion. Scientific reports. 2013;3:2086.

169. Stankovich S, Dikin DA, Dommett GH, Kohlhaas KM, Zimney EJ, Stach EA, et al. Graphene-based composite materials. nature. 2006;442(7100):282-6.

170. Ramanathan T, Abdala A, Stankovich S, Dikin D, Herrera-Alonso M, Piner R, et al. Functionalized graphene sheets for polymer nanocomposites. Nature nanotechnology. 2008;3(6):327-31.

171. Potts JR, Dreyer DR, Bielawski CW, Ruoff RS. Graphene-based polymer nanocomposites. Polymer. 2011;52(1):5-25.

172. Xiong D-B, Cao M, Guo Q, Tan Z, Fan G, Li Z, et al. Graphene-and-copper artificial nacre fabricated by a preform impregnation process: bioinspired strategy for strengthening-toughening of metal matrix composite. Acs Nano. 2015;9(7):6934-43.

173. Wang D, Choi D, Li J, Yang Z, Nie Z, Kou R, et al. Self-assembled TiO2–graphene hybrid nanostructures for enhanced Li-ion insertion. ACS nano. 2009;3(4):907-14.

174. Levendorf MP, Kim C-J, Brown L, Huang PY, Havener RW, Muller DA, et al. Graphene and boron nitride lateral heterostructures for atomically thin circuitry. Nature. 2012;488(7413):627-32.

175. Li Y, Peng Z, Larios E, Wang G, Lin J, Yan Z, et al. Rebar graphene from functionalized boron nitride nanotubes. ACS nano. 2015;9(1):532-8.

176. Gojny F, Wichmann M, Köpke U, Fiedler B, Schulte K. Carbon nanotube-reinforced epoxy-composites: enhanced stiffness and fracture toughness at low nanotube content. Composites science and technology. 2004;64(15):2363-71.

177. Yang Y, Kim ND, Varshney V, Sihn S, Li Y, Roy AK, et al. In situ mechanical investigation of carbon nanotube–graphene junction in three-dimensional carbon nanostructures. Nanoscale. 2017;9(8):2916-24.
178. Ganesan Y, Lu Y, Peng C, Lu H, Ballarini R, Lou J. Development and application of a novel microfabricated device for the in situ tensile testing of 1-D nanomaterials. Journal of microelectromechanical systems. 2010;19(3):675-82.
179. Yang Y, Chen W, Hacopian E, Dong P, Sun A, Ci L, et al. Unveil the size-dependent mechanical behaviors of individual CNT/SiC composite nanofibers by in situ tensile tests in SEM. Small. 2016;12(33):4486-91.
180. Sha J, Salvatierra RV, Dong P, Li Y, Lee S-K, Wang T, et al. Three-dimensional rebar graphene. ACS applied materials & interfaces. 2017;9(8):7376-84.
181. Bauer J, Meza LR, Schaedler TA, Schwaiger R, Zheng X, Valdevit L. Nanolattices: an emerging class of mechanical metamaterials. Advanced Materials. 2017;29(40):1701850.
182. Zhang X, Vyatskikh A, Gao H, Greer JR, Li X. Lightweight, flaw-tolerant, and ultrastrong nanoarchitected carbon. Proceedings of the National Academy of Sciences. 2019;116(14):6665-72.
183. Qin Z, Jung GS, Kang MJ, Buehler MJ. The mechanics and design of a lightweight three-dimensional graphene assembly. Science advances. 2017;3(1):e1601536.
184. Jung GS, Buehler MJ. Multiscale mechanics of triply periodic minimal surfaces of three-dimensional graphene foams. Nano letters. 2018;18(8):4845-53.
185. Zhang X, Zhong L, Mateos A, Kudo A, Vyatskikh A, Gao H, et al. Theoretical strength and rubber-like behaviour in micro-sized pyrolytic carbon. Nature nanotechnology. 2019;14(8):762-9.
186. Kashani H, Ito Y, Han J, Liu P, Chen M. Extraordinary tensile strength and ductility of scalable nanoporous graphene. Science advances. 2019;5(2):eaat6951.
187. Hu M, He J, Zhao Z, Strobel TA, Hu W, Yu D, et al. Compressed glassy carbon: An ultrastrong and elastic interpenetrating graphene network. Science advances. 2017;3(6):e1603213.
188. Gao H, Ji B, Jäger IL, Arzt E, Fratzl P. Materials become insensitive to flaws at nanoscale: lessons from nature. Proceedings of the national Academy of Sciences. 2003;100(10):5597-600.
189. Gao H, Chen S. Flaw tolerance in a thin strip under tension. Journal of Applied Mechanics. 2005;72(5):732-7.

190. Gu XW, Jafary-Zadeh M, Chen DZ, Wu Z, Zhang Y-W, Srolovitz DJ, et al. Mechanisms of failure in nanoscale metallic glass. Nano letters. 2014;14(10):5858-64.

191. Allen MJ, Tung VC, Kaner RB. Honeycomb carbon: a review of graphene. Chemical reviews. 2009;110(1):132-45.

192. Zhang P, Ma L, Fan F, Zeng Z, Peng C, Loya PE, et al. Fracture toughness of graphene. Nature communications. 2014;5:3782.

193. Anderson TL, Anderson TL. Fracture mechanics: fundamentals and applications: CRC press; 2005.

194. Schaedler TA, Jacobsen AJ, Torrents A, Sorensen AE, Lian J, Greer JR, et al. Ultralight metallic microlattices. Science. 2011;334(6058):962-5.

195. Meza LR, Das S, Greer JR. Strong, lightweight, and recoverable three-dimensional ceramic nanolattices. Science. 2014;345(6202):1322-6.

196. Meza LR, Zelhofer AJ, Clarke N, Mateos AJ, Kochmann DM, Greer JR. Resilient 3D hierarchical architected metamaterials. Proceedings of the National Academy of Sciences. 2015;112(37):11502-7.

197. Salari-Sharif L, Schaedler TA, Valdevit L. Energy dissipation mechanisms in hollow metallic microlattices. Journal of Materials Research. 2014;29(16):1755-70.

198. Holmes DP. Elasticity and Stability of Shape Changing Structures. Current opinion in colloid & interface science. 2019.

199. Bertoldi K, Vitelli V, Christensen J, van Hecke M. Flexible mechanical metamaterials. Nature Reviews Materials. 2017;2(11):17066.

200. Fargette A, Neukirch S, Antkowiak A. Elastocapillary snapping: Capillarity induces snap-through instabilities in small elastic beams. Physical review letters. 2014;112(13):137802.

201. Cedolin L. Stability of structures: elastic, inelastic, fracture and damage theories: World Scientific; 2010.

202. Pandey A, Moulton DE, Vella D, Holmes DP. Dynamics of snapping beams and jumping poppers. EPL (Europhysics Letters). 2014;105(2):24001.

203. Haghpanah B, Salari-Sharif L, Pourrajab P, Hopkins J, Valdevit L. Multistable shape-reconfigurable architected materials. Advanced Materials. 2016;28(36):7915-20.

204. Shan S, Kang SH, Raney JR, Wang P, Fang L, Candido F, et al. Multistable architected materials for trapping elastic strain energy. Advanced Materials. 2015;27(29):4296-301.

205. Restrepo D, Mankame ND, Zavattieri PD. Phase transforming cellular materials. Extreme Mechanics Letters. 2015;4:52-60.
206. Rafsanjani A, Akbarzadeh A, Pasini D. Snapping mechanical metamaterials under tension. Advanced Materials. 2015;27(39):5931-5.
207. Li T, Zhang Z. Snap-through instability of graphene on substrates. Nanoscale research letters. 2010;5(1):169.
208. Puglisi G, Truskinovsky L. Mechanics of a discrete chain with bi-stable elements. Journal of the Mechanics and Physics of Solids. 2000;48(1):1-27.
209. Puglisi G, Truskinovsky L. A mechanism of transformational plasticity. Continuum Mechanics and Thermodynamics. 2002;14(5):437-57.
210. Puglisi G, Truskinovsky L. Rate independent hysteresis in a bi-stable chain. Journal of the Mechanics and Physics of Solids. 2002;50(2):165-87.
211. Puglisi G, Truskinovsky L. Thermodynamics of rate-independent plasticity. Journal of the Mechanics and Physics of Solids. 2005;53(3):655-79.
212. Williams PM, Fowler SB, Best RB, Toca-Herrera JL, Scott KA, Steward A, et al. Hidden complexity in the mechanical properties of titin. Nature. 2003;422(6930):446.
213. Oberhauser AF, Hansma PK, Carrion-Vazquez M, Fernandez JM. Stepwise unfolding of titin under force-clamp atomic force microscopy. Proceedings of the National Academy of Sciences. 2001;98(2):468-72.
214. Bhattacharya K. Microstructure of martensite: why it forms and how it gives rise to the shape-memory effect: Oxford University Press; 2003.
215. Gandhi MV, Thompson B. Smart materials and structures: Springer Science & Business Media; 1992.
216. Calladine CR. Theory of shell structures: Cambridge University Press; 1989.
217. Holmes DP, Crosby AJ. Snapping surfaces. Advanced Materials. 2007;19(21):3589-93.
218. Tavakol B, Bozlar M, Punckt C, Froehlicher G, Stone HA, Aksay IA, et al. Buckling of dielectric elastomeric plates for soft, electrically active microfluidic pumps. Soft matter. 2014;10(27):4789-94.
219. Taffetani M, Jiang X, Holmes DP, Vella D. Static bistability of spherical caps. Proceedings of the Royal Society A: Mathematical, Physical and Engineering Sciences. 2018;474(2213):20170910.

220. Panter JR, Chen J, Zhang T, Kusumaatmaja H. Harnessing energy landscape exploration to control the buckling of cylindrical shells. Communications physics. 2019.
221. Friedman JB. Flexible drinking straw. Google Patents; 1951.
222. Harp HJ, Leible WT, Mccort WM. Flexible drinking tube. Google Patents; 1968.
223. Bende NP, Yu T, Corbin NA, Dias MA, Santangelo CD, Hanna JA, et al. Overcurvature induced multistability of linked conical frusta: how a 'bendy straw'holds its shape. Soft matter. 2018;14(42):8636-42.
224. Ni B, Zhang T, Li J, Li X, Gao H. Topological design of graphene. Handbook of Graphene: Physics, Chemistry, and Biology. 2019:1.
225. Seymour M, Provatas N. Structural phase field crystal approach for modeling graphene and other two-dimensional structures. Physical Review B. 2016;93(3):035447.
226. Hoover WG. Canonical dynamics: Equilibrium phase-space distributions. Physical review A. 1985;31(3):1695.
227. Filleter T, McChesney JL, Bostwick A, Rotenberg E, Emtsev KV, Seyller T, et al. Friction and dissipation in epitaxial graphene films. Physical review letters. 2009;102(8):086102.
228. Rogers RC, Truskinovsky L. Discretization and hysteresis. Physica B: Condensed Matter. 1997;233(4):370-5.
229. Benichou I, Givli S. The hidden ingenuity in titin structure. Applied Physics Letters. 2011;98(9):091904.
230. Rief M, Gautel M, Oesterhelt F, Fernandez JM, Gaub HE. Reversible unfolding of individual titin immunoglobulin domains by AFM. science. 1997;276(5315):1109-12.
231. Fraternali F, Blesgen T, Amendola A, Daraio C. Multiscale mass-spring models of carbon nanotube foams. Journal of the Mechanics and Physics of Solids. 2011;59(1):89-102.
232. Benichou I, Givli S. Structures undergoing discrete phase transformation. Journal of the Mechanics and Physics of Solids. 2013;61(1):94-113.
233. Florijn B, Coulais C, van Hecke M. Programmable mechanical metamaterials. Physical review letters. 2014;113(17):175503.
234. Yoon J, Park W, Bae GY, Kim Y, Jang HS, Hyun Y, et al. Highly flexible and transparent multilayer MoS2 transistors with graphene electrodes. Small. 2013;9(19):3295-300.
235. Hong YK, Liu N, Yin D, Hong S, Kim DH, Kim S, et al. Recent progress in high-mobility thin-film transistors based on multilayer 2D materials. Journal of Physics D: Applied Physics.

2017;50(16):164001.
236. Liu Y, Weiss NO, Duan X, Cheng H-C, Huang Y, Duan X. Van der Waals heterostructures and devices. Nature Reviews Materials. 2016;1(9):1-17.
237. Castilho CJ, Li D, Liu M, Liu Y, Gao H, Hurt RH. Mosquito bite prevention through graphene barrier layers. Proceedings of the National Academy of Sciences. 2019;116(37):18304-9.
238. Hu Z, Tong G, Lin D, Chen C, Guo H, Xu J, et al. Graphene-reinforced metal matrix nanocomposites–a review. Materials Science and Technology. 2016;32(9):930-53.
239. Nieto A, Bisht A, Lahiri D, Zhang C, Agarwal A. Graphene reinforced metal and ceramic matrix composites: a review. International Materials Reviews. 2017;62(5):241-302.
240. Sreenivasulu B, Ramji B, Nagaral M. A review on graphene reinforced polymer matrix composites. Materials Today: Proceedings. 2018;5(1):2419-28.
241. Novoselov K, Mishchenko oA, Carvalho oA, Neto AC. 2D materials and van der Waals heterostructures. Science. 2016;353(6298).
242. Cao Y, Fatemi V, Demir A, Fang S, Tomarken SL, Luo JY, et al. Correlated insulator behaviour at half-filling in magic-angle graphene superlattices. Nature. 2018;556(7699):80-4.
243. Cao Y, Fatemi V, Fang S, Watanabe K, Taniguchi T, Kaxiras E, et al. Unconventional superconductivity in magic-angle graphene superlattices. Nature. 2018;556(7699):43-50.
244. Liu Y, Sheng J, Wu H, He Q, Cheng HC, Shakir MI, et al. High‐Current‐Density Vertical‐Tunneling Transistors from Graphene/Highly Doped Silicon Heterostructures. Advanced Materials. 2016;28(21):4120-5.
245. Withers F, Del Pozo-Zamudio O, Schwarz S, Dufferwiel S, Walker P, Godde T, et al. WSe2 light-emitting tunneling transistors with enhanced brightness at room temperature. Nano letters. 2015;15(12):8223-8.
246. Yang H, Heo J, Park S, Song HJ, Seo DH, Byun K-E, et al. Graphene barristor, a triode device with a gate-controlled Schottky barrier. Science. 2012;336(6085):1140-3.
247. Wang F, Wang Z, Xu K, Wang F, Wang Q, Huang Y, et al. Tunable GaTe-MoS2 van der Waals p–n junctions with novel optoelectronic performance. Nano letters. 2015;15(11):7558-66.
248. Cheng R, Jiang S, Chen Y, Liu Y, Weiss N, Cheng H-C, et al. Few-layer molybdenum disulfide transistors and circuits for high-speed flexible electronics. Nature communications. 2014;5(1):1-9.

249. Georgiou T, Jalil R, Belle BD, Britnell L, Gorbachev RV, Morozov SV, et al. Vertical field-effect transistor based on graphene–WS 2 heterostructures for flexible and transparent electronics. Nature nanotechnology. 2013;8(2):100.

250. Li J, Xiong Y, Wang X, Yan S, Yang C, He W, et al. Microstructure and tensile properties of bulk nanostructured aluminum/graphene composites prepared via cryomilling. Materials Science and Engineering: A. 2015;626:400-5.

251. Kuang D, Xu L, Liu L, Hu W, Wu Y. Graphene–nickel composites. Applied Surface Science. 2013;273:484-90.

252. He T, Li J, Wang L, Zhu J, Jiang W. Preparation and consolidation of alumina/graphene composite powders. Materials transactions. 2009;50(4):749-51.

253. Walker LS, Marotto VR, Rafiee MA, Koratkar N, Corral EL. Toughening in graphene ceramic composites. ACS nano. 2011;5(4):3182-90.

254. Zhang L, Liu W, Yue C, Zhang T, Li P, Xing Z, et al. A tough graphene nanosheet/hydroxyapatite composite with improved in vitro biocompatibility. Carbon. 2013;61:105-15.

255. Hod O. Graphite and hexagonal boron-nitride have the same interlayer distance. Why? Journal of chemical theory and computation. 2012;8(4):1360-9.

256. Minatto FD, Milak P, De Noni A, Hotza D, Montedo ORK. Multilayered ceramic composites–a review. Advances in Applied Ceramics. 2015;114(3):127-38.

257. Kant T, Swaminathan K. Estimation of transverse/interlaminar stresses in laminated composites–a selective review and survey of current developments. Composite structures. 2000;49(1):65-75.

258. Cao K, Feng S, Han Y, Gao L, Ly TH, Xu Z, et al. Elastic straining of free-standing monolayer graphene. Nature communications. 2020;11(1):1-7.

259. Han Y, Feng S, Cao K, Wang Y, Gao L, Xu Z, et al. Large Elastic Deformation and Defect Tolerance of Hexagonal Boron Nitride Monolayers. Cell Reports Physical Science. 2020;1(8):100172.

260. Wang G, Dai Z, Wang Y, Tan P, Liu L, Xu Z, et al. Measuring interlayer shear stress in bilayer graphene. Physical review letters. 2017;119(3):036101.

261. Daly M, Cao C, Sun H, Sun Y, Filleter T, Singh CV. Interfacial shear strength of multilayer graphene oxide films. ACS nano. 2016;10(2):1939-47.

262. Oviedo JP, KC S, Lu N, Wang J, Cho K, Wallace RM, et al. In situ TEM characterization of shear-stress-induced interlayer sliding in the cross section view of molybdenum disulfide. ACS nano. 2015;9(2):1543-51.
263. Jang B, Kim B, Kim J-H, Lee H-J, Sumigawa T, Kitamura T. Asynchronous cracking with dissimilar paths in multilayer graphene. Nanoscale. 2017;9(44):17325-33.
264. Jung GS, Wang S, Qin Z, Martin-Martinez FJ, Warner JH, Buehler MJ. Interlocking friction governs the mechanical fracture of bilayer MoS2. ACS nano. 2018;12(4):3600-8.
265. Kumar H, Dong L, Shenoy VB. Limits of coherency and strain transfer in flexible 2D van der waals heterostructures: formation of strain solitons and interlayer debonding. Scientific reports. 2016;6(1):1-8.
266. Yang L, Xu H, Liu K, Gao D, Huang Y, Zhou Q, et al. Molecular dynamics simulation on the formation and development of interlayer dislocations in bilayer graphene. Nanotechnology. 2020;31(12):125704.
267. Liu Y, Xu Z. Multimodal and self-healable interfaces enable strong and tough graphene-derived materials. Journal of the Mechanics and Physics of Solids. 2014;70:30-41.
268. Griffith AA. VI. The phenomena of rupture and flow in solids. Philosophical transactions of the royal society of london Series A, containing papers of a mathematical or physical character. 1921;221(582-593):163-98.
269. Bower AF. Applied mechanics of solids: CRC press; 2009.
270. Liu Y, Bhowmick S, Yakobson BI. BN white graphene with “colorful” edges: The energies and morphology. Nano letters. 2011;11(8):3113-6.
271. Huang L, Li Y, Wei Z, Li J. Strain induced piezoelectric effect in black phosphorus and MoS 2 van der Waals heterostructure. Scientific reports. 2015;5(1):1-7.
272. Javvaji B, He B, Zhuang X. The generation of piezoelectricity and flexoelectricity in graphene by breaking the materials symmetries. Nanotechnology. 2018;29(22):225702.
273. Kothari M, Cha M-H, Lefevre V, Kim K-S. Critical curvature localization in graphene. II. Non-local flexoelectricity–dielectricity coupling. Proceedings of the Royal Society A. 2019;475(2221):20180671.
274. Kothari M, Cha M-H, Kim K-S. Critical curvature localization in graphene. I. Quantum-flexoelectricity effect. Proceedings of the Royal Society A: Mathematical, Physical and Engineering Sciences. 2018;474(2214):20180054.

275. Amiri F, Millán D, Shen Y, Rabczuk T, Arroyo M. Phase-field modeling of fracture in linear thin shells. Theoretical and Applied Fracture Mechanics. 2014;69:102-9.
276. Gu GX, Chen C-T, Richmond DJ, Buehler MJ. Bioinspired hierarchical composite design using machine learning: simulation, additive manufacturing, and experiment. Materials Horizons. 2018;5(5):939-45.
277. Goldberg DE, Samtani MP, editors. Engineering optimization via genetic algorithm. Electronic computation; 1986: ASCE.
278. Ritchie RO. The conflicts between strength and toughness. Nature materials. 2011;10(11):817-22.
279. Leven I, Maaravi T, Azuri I, Kronik L, Hod O. Interlayer potential for graphene/h-BN heterostructures. Journal of chemical theory and computation. 2016;12(6):2896-905.